Universidad Autónoma de San Luis Potosí
Facultad de Ingeniería
Centro de Investigación y Estudios de Posgrado

Maximum oscillations and hydrodynamic response of flexible circular cylinders undergoing vortex-induced vibrations

T E S I S

Que para obtener el grado de:

Doctora en Ingeniería Mecánica con opción terminal en termofluidos

Presenta:
M.I. Cintia Monreal Jiménez

Asesor:

Dr. Francisco Oviedo Tolentino

Co-asesora:

Dra. Geydy Luz Gutiérrez Urueta

San Luis Potosí, S. L. P. Agosto de 2020

UASLP
Universidad Autónoma de San Luis Potosí

FACULTAD DE
INGENIERÍA

5 de diciembre de 2019

M.I. CINTIA MONREAL JIMÉNEZ
P R E S E N T E

En atención a su solicitud de Temario, presentada por los **Dres. Francisco Oviedo Tolentino y Geydy Luz Gutiérrez Urueta** Asesor y Co-asesor de la Tesis que desarrollará Usted, con el objeto de obtener el Grado de **Doctora en Ingeniería Mecánica con Orientación Terminal en Termofluidos**, me es grato comunicarle que en la Sesión del H. Consejo Técnico Consultivo celebrada el día 5 de diciembre del presente año, fue aprobado el Temario propuesto:

TEMARIO:

"Oscilaciones máximas y respuesta hidrodinámica de cilindros circulares flexibles sometidos a vibraciones inducidas por vórtices"

Introducción.
1. Historia y fundamentos de las vibraciones.
2. Teoría de las vibraciones inducidas por vórtices.
3. Análisis dinámico e hidrodinámico de un cilindro circular sometido a vibraciones inducidas por vórtices.
4. Resultados y discusión de la respuesta en amplitud en la gráfica de Griffin y su comparación con parámetros de clasificación.
5. Resultados y discusión de los modos de desprendimiento de vórtices en el mapa de Williamson-Roshko.

Conclusiones
Referencias

"MODOS ET CUNCTARUM RERUM MENSURAS AUDEBO"

A T E N T A M E N T E

UNIVERSIDAD AUTONOMA DE SAN LUIS POTOSI
FACULTAD DE INGENIERIA
DIRECCION

M. I. JORGE ALBERTO PÉREZ GONZÁLEZ
DIRECTOR

UNIVERSIDAD AUTÓNOMA DE SAN LUIS POTOSÍ
FACULTAD DE INGENIERÍA
RECIBIDO
02 JUN 2020

Copia. Archivo
*etn.

www.uaslp.mx

Av. Manuel Nava 8
Zona Universitaria • CP 78290
San Luis Potosí, S.L.P.
tel. (444) 826 2330 al39
fax (444) 826 2336

Universidad Autónoma de San Luis Potosí

Facultad de Ingeniería

Centro de Investigación y Estudios de Posgrado

Thesis for the degree of PhD in Mechanical Engineering

Maximum oscillations and hydrodynamic response of flexible circular cylinders undergoing vortex-induced vibrations

Cintia Monreal Jiménez

August 2020

Committee

Dr. Francisco Oviedo Tolentino

Dra. Geydy Luz Gutiérrez Urueta

Dr. Emilio Jorge González Galván

Dr. Ricardo Romero Méndez

Dr. Gilberto Mejía Rodríguez

Dr. Francisco Gerardo Pérez Gutiérrez

Dr. Daniel Juárez Robles

Abstract

Despite the attention given to vortex induced-vibrations (VIV) in the last years, especially due to energy harvesting, many related subjects are still no well-known. This work aims to reveal how the behavior of the maximum amplitude is affected by different parameters, from geometric characteristics to parameters proposed in the literature as the mass-damping coefficient. To achieve this, meticulous experimental research, with a broad variety of *cantilevered uniform flexible circular cylinder* in a steady current along the entire lock-in region, is proposed. The length, diameter, and density (materials) were varied in the experimental campaign. A total of 36 cylinders were proposed, from which only 31 could be studied due to operating ranges restrictions of the water tunnel.

For the dynamic response, the tip of the cylinder was recorded using a high-speed video camera. This allows to determine the path followed by the cylinder using circle recognition functions in a Matlab ® code. For the hydrodynamic response downstream the cylinder, the PIV technique with hydrogen bubbles as tracers was used.

Results obtained in this work reveal atypical behavior (compared with reported in the literature) in maxima amplitudes. Cylinders are classified into four groups, each one separated in different branches. Results also offer a comparison among different parameters to classify the cylinders.

For the hydrodynamic response, experimental results are presented and compared with the Williamson-Roshko map, revealing discordance. Trajectories and vortex shedding modes are illustrated for one cylinder of each group along with the entire synchronization regime. The jumps in these modes are aligned with most of the different branches in each group.

Acknowledgments

I would like to express my gratitude to the National Council for Science and Technology (CONACYT) for the scholarship given to obtain my PhD degree. Also, I would like to thank the Center for Research and Graduate Studies of the Faculty of Engineering (CIEP-FI) of the Autonomous University of San Luis Potosi (UASLP) for their support for the development of this project. Particularly to Dr. Francisco Oviedo Tolentino, Dra. Geydy Luz Gutiérrez Urueta, Dr. Emilio González Galván, Dr. Ricardo Romero Méndez and all my dissertation committee for their invaluable contributions to this thesis.

Contents

List of Figures

List of Tables

Nomenclature

a	acceleration
A^*	normalized maximum amplitude, A/D
A	cross-sectional area of the cylinder
c	structural damping, viscous damping coefficient, damping constant
C_D	drag coefficient
C_M	inertia coefficient
C_L	lift coefficient
C_m	hydrodynamic mass coefficient
C_{mc}	hydrodynamic mass coefficient in current
C_p	pressure coefficient
δ	logarithmic decrement
D	diameter of the cylinder
f	body oscillation frequency, frequency of vibrations
f_n	natural frequency
f_v	vortex shedding frequency
F	fluid force in the transverse direction
F_D	drag, total in-line force
F_f	resultant force due to friction per unit length
F_L	lift, total cross-flow force
$F_{potential}$	potential force

F_p	resultant force due to pressure per unit length
F_{total}	total fluid force
F_{vortex}	vortex force
k	spring constant
KC	Keulegan-Carpenter number
m'	hydrodynamic mass
m	total mass of the system
m'_c	hydrodynamic mass in current
$m^*\zeta$	mass-damping parameter
μ	dynamic viscosity
p	pressure
p_0	hydrostatic pressure
ϕ	phase angle, represents the offset between the fluid force and the body displacement
ϕ	angular coordinate, velocity potential
ϕ_{total}	total phase angle
ϕ_{vortex}	vortex phase angle
φ	phase delay
r, θ	polar coordinates
r_0	cylindre radius
Re	Reynolds number
ρ	fluid density
ζ	total damping
ζ_f	fluid damping
ζ_s	structural damping

St	Strouhal number
T	period of the vibration
t	time
τ_0	wall shear stress
U_b	body velocity in the in-line direction
U_m	maximum value of oscillatory-flow velocity
U	main flow velocity
ν	kinematic viscosity
V_r	reduced velocity
v	speed
ω	angular oscillation frequency
ω_d	damped natural angular frequency
ω_{dv}	angular frequency of damped free vibrations
ω_n	undamped natural angular frequency
ω_v	angular frequency of undamped free vibrations
x, y	x- and y-displacements of structure

Introduction

Mechanical vibrations are one of the most important topics in mechanical engineering. Depending on the situation, vibrations can be desired or not. For example, in a vehicle suspension vibrations are necessary in order to allow wheels to remain always in contact to the ground and to not lose stability, as well as to dissipate energy and bring a comfortable trip. In energy harvesting, the piezoelectric effect (the ability of certain materials to generate an electric charge as a response to mechanical vibrations) is being used to produce environmentally friendly energy. On the other hand, undesired vibrations must be avoided and considered in the design of mechanical devices. For example, vibrations in machines, such as an unbalanced helicopter motor, may lead to failure and therefore to catastrophic events. Vibrations caused by earthquakes may also cause catastrophic events, but due to structural failure (creeping or stress peak).

A specific type of mechanical vibrations is the one caused by fluid-structural coupling. The most famous example of this kind of vibrations is the Tacoma Narrows Bridge. The bridge collapsed (Nov. 8, 1940) at 64 km/h, a much lower wind speed for which this structure was designed. The cause of failure is related to vortex-induced vibrations. Without speaking strictly, vortex-induced vibrations (VIV) occur when the structure becomes coupled in an unstable oscillation driven by a fluid (air in the case of the Tacoma Bridge). The oscillations increase their amplitude in each cycle because the structure is unable to dissipate energy at the same rate at which the fluid inserts energy into it. Finally, the oscillations are so large that cause failure due to excessive deflection and stress.

Motivation and justification

The Tacoma bridge event marked the necessity to consider VIV effects in civil and structural engineering. Since then, several fundamental studies were carried out by different researches, many of them discussed in the reviews of Sarpkaya (1979), Griffin & Ramberg (1982), Bearman (1984), Parkinson (1989) and Williamson & Govardhan (2004). These among other studies help to develop new bridge designs capable of suppressing VIV. An example is the second Jindo Bridge built in 2005 with a main span of 344 m, see Fig. 1a. In this bridge, vortex-induced vibration was observed in the windward bridge deck. To mitigate the amplitude of vibration 4 sets of 3.5 ton TMDs

(Tuned Mass Damper), see Fig. 1b, which is a vibration control device installed inside the structures to reduce wind-induced vibrations, designed by TESolution (an engineering company specializing in wind engineering and vibration control) were installed inside the bridge deck to reduce the vertical amplitude of 30cm to 3cm.

a)  b) 

Figure 1: 2nd Jindo Bridge: a) Actual photography and b) Vertical TMD (Tuned Mass Dampers) for the 2nd Jindo Bridge. Obtained from http://www.tesolution.com/2nd-jindo-bridge-tuned-mass-dampers.html.

Despite the mentioned and several works on VIV, many fundamental questions still exist. Some of these interrogations are directly related to the behavior of the structure in the lock-in region. This thesis is an effort to explore how the variation on the structural parameters (material, diameter and length) affects the behavior of the amplitude response in the synchronization regime.

Objectives

The general objective is:

Determine the maximum oscillation and hydrodynamic response of flexible circular cylinders subject to vortex induced-vibrations.

Specific objectives are:

1. Deepen the state of the art on VIV for flexible circular cylinders.
2. Design an experimental campaign considering relevant parameters on maximum oscillation.
3. Build the experimental apparatus.
4. Develop a mathematical code to determine the dynamic response of the cylinder using the PTV technique.

Organization of this work

The following 5 chapters will be a broader development of this brief introduction. In Chapter 1, the history and the fundamentals of vibrations are explained. Here the importance and the elements of vibrations are presented. In Chapter 2, the theory of vortex induced vibrations is settled down. Basic concepts and simple explanations based on the state of art are developed here. Chapter 3, treats the dynamic and hydrodynamic analysis setup. This is a broad explanation in how to obtain the parameters and the techniques to acquire both dynamic and hydrodynamic responses. In Chapter 4 the experimental results are presented. Some of the main results are the dynamic response of the tip of the cylinder. Different behaviors are distinguished and classified in four different groups. Finally, in chapter 5 the vortex shedding pattern is analyzed and compared with the Williamson Roshko map along the lock-in region for each group.

At the end of this thesis, the main conclusions along with contributions and future work are given.

1 History and fundamentals of vibrations

This chapter briefly explains the general notions of mechanical vibrations. First, a short historical review of the study of vibration from its origins to the twentieth century is given. Then, the importance of vibration analysis is discussed. Afterward, the three main elements of vibrating systems are given. Finally, the chapter is focused on Vortex Induced Vibrations (VIV) from its basic concepts to the different types of apparatus used to study this phenomenon. The main equations to analyze VIV and the different dynamic and hydrodynamic responses reported in the literature are established.

1.1 A brief historical review on vibrations

It is very probable that people became interested in vibration with the creation of the first musical instruments. These people, long ago as 4000 B.C., started to define some rules based on experience and the notions of what they considered sounded better. Nevertheless, their knowledge never reached the level of a science.

It was until Greek civilization reached its high point that mathematicians as Pythagoras (582-507 B.C.) started to research sounds on a scientific basis. He used an apparatus called "monochord" to investigate the sound of a string (see Fig. 1.1). This device consisted of a piece of wood with three bridges, two fixed at the ends and one mobile in the middle. A cord was placed on top of the bridges, one side was fixed to the main piece of wood and the other end was held at constant tension due to weight. Pythagoras noticed that two strings with different lengths, one half of the other, but the same tension emits the same note, but the shorter one emits it an octave above. This is a raw definition of *pitch* (the degree of highness or lowness of a tone).

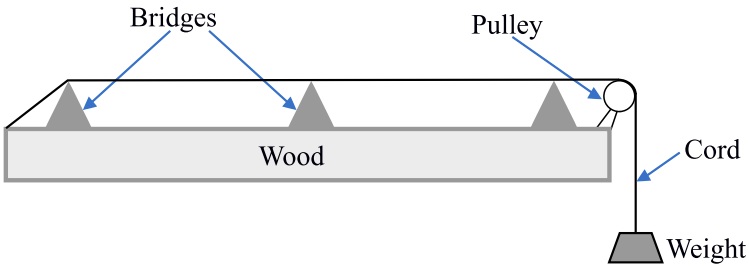

Figure 1.1: Monochord scheme.

Besides of Pythagoras, there are only a few other greek works on the subject of music. In 320 B.C., Aristoxenus wrote a work entitled "Elements of Harmony" and in 300 B.C., Euclid wrote about music without any reference to the physical nature of sound. Moreover, it seems that no further advances in the theories of sound and vibration were made for nearly 16 centuries in Western civilization.

On the eastern side of the world, in a.d. 132, Zhang Heng invented the first seismograph (see Fig. 1.2). It consisted of a bronze jar with a special mechanism. It had eight dragon faces with a ball in its mouth, each pointing to a specific direction. When an earthquake started the pendulum would tilt in that direction, causing one dragon to drop the ball. The ball produced a tinkling sound, alerting direction and time of the earthquake.

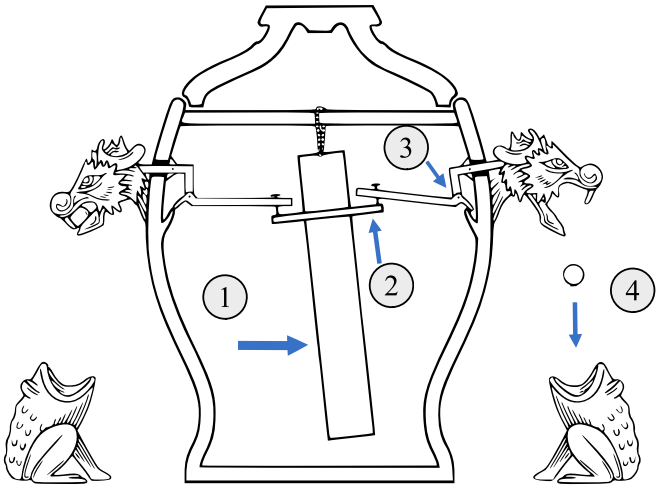

Figure 1.2: First seismograph.

Back to Europe, in the seventeenth century, Galileo Galilei study the behavior of a simple pendulum, this idea first became from observing the movement of a lamp in

a church in Pisa. From his experiments, he found that the *time period* (the time the pendulum takes from one side to the other and back) was independent of the amplitude of swings. Also he described the relation among the time period and the length of the pendulum and with *resonance* (increase in amplitude of oscillation due to synchronous vibration).

Almost at the same time that Galileo, in France the mathematician Marin Mersenne measured the frequency of vibration of a long string and with that information predicted the frequency of a shorter one with same tension and density. Later, in London, Robert Hooke conducted experiments to find the relation between pitch and frequency of a string. Also, Joseph Sauveur in France and John Wallis in England observed, in a separate way, that a vibrating string has no motion at particular points (*nodes*) while all the other points form specific shapes (*loops*). They also found that the higher frequencies were integral multiples of the frequency with just one loop in the same string. This "one loop shape" corresponds with the *fundamental frequency*, and higher frequencies are called *harmonics*. Example of these terms are shown in Fig. 1.3.

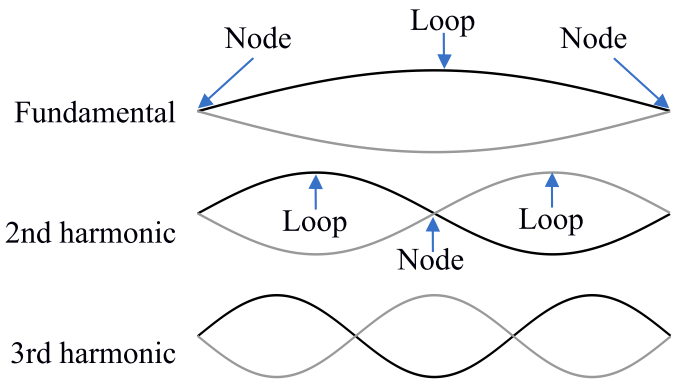

Figure 1.3: Illustrative scheme of loops, nodes, fundamental and harmonic frequencies.

Shortly after, Isaac Newton published its second law of motion, which is now used to derive the equations of motion of a vibrating body. Moreover, Brook Taylor found the theoretical solution of the problem of the vibrating string. The natural frequency obtained by Taylor agreed with the experimental values of Galileo and Mersenne. The procedure followed by Taylor would be perfected later by Daniel Bernoulli, Jean D'Alembert and Leonard Euler with the introduction of partial derivatives in the equations of motion.

From the work of these scientists, the principle of superposition was developed. This is the most valuable development of theory of vibrations. All started with the problem presented by the possibility of a string vibrating with several harmonics at the same

time. This would lead to the fact that the displacement of any particle of the string at any instant would be equal to the algebraic sum of displacement for each harmonic. Namely, absolutely any function (shape of the string) can be represented as an infinite sum of series of sines and cosines, see Fig. 1.4. It was Fourier in 1822 who finally proved the validity of this principle.

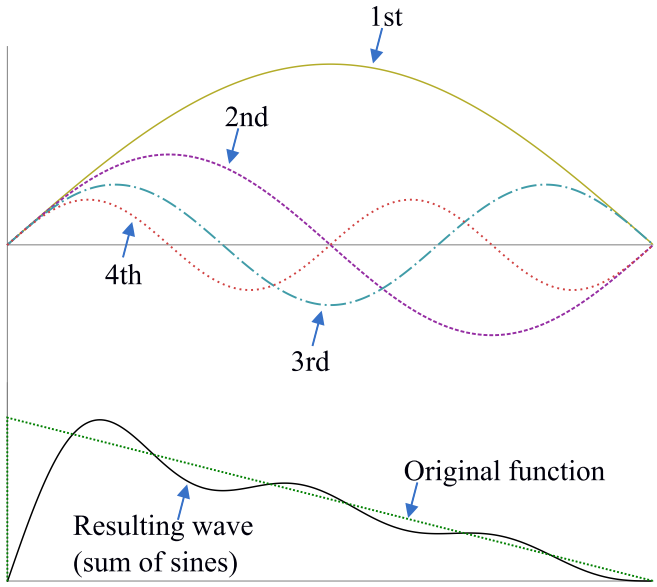

Figure 1.4: Superposition principle example.

The analytical solution of the vibrating string was presented by Joseph Lagrante in 1759. He assumed that the string was made up of small equally spaced mass particles, and that for each particle would have a independent frequency. If the number of masses increases til infinite, the resulting frequencies would be the harmonic frequencies of the original string.

Around that time, the studies on different bodies other than strings became important. Euler and Bernoulli focused their work on the vibration of thin beams supported and clamped. Their approaches are now known as the Euler-Bernoulli beam theory. Coulomb conducted experiments and also did theoretical work on torsional oscillations of a metal cylinder suspended by a wire. He found that the period of oscillation is independent of the angle of twist. The vibrations of plates was studied by Sophie Germain and later her work were corrected by G. R. Kirchhoff. Meanwhile Poisson solved the problem of vibration of a rectangular flexible membrane. To finish the nineteenth century, Baron Rayleigh published a book on theory of sound. He published a method to find the fundamental frequency on a conservative system by using the

principle of conservation of energy. Nowadays, an extension of this method is used to find multiple natural frequencies, the Rayleigh-Ritz method.

In the twentieth century, Aurel Stodola contributed to the study of plates, membranes, and beams, this last is also applicable to turbines; P. De Laval proposed a solution for unbalanced rotating disk; and Stephen Timoshenko improved the theory of beams by considering the effects of rotary inertia and shear deformations. Besides these breakthroughs, the recent studies are mainly focused on using numerical evaluation (finite element method, among others) to treat complex systems.

1.2 Importance of vibration analysis

Vibrations are part of our daily life. As we walk we produce a periodic motion. We can hear because of vibration. The light we see can be described by waves that undergo vibration. We need vibrations in our vocal chords to communicate.

As seen earlier, back in history, our ancients wanted to understand the phenomena in natural events. However, in recent times, the studies are driven by engineering applications (design of machines or structures). For some cases vibration can lead to negative effects such as noise, wear of bearings or other machine parts, poor quality in the surface finishing, failure due to fatigue, and so on. In the specific case of structural vibration, it can cause discomfort and even fear in their occupants. Key concepts to take care when designing a civil structure is the natural frequency and the resonance. For example, the American Association of State Highway and Transportation Officials (AASHTO) in the United States of America specifies the minimum frequency for a pedestrian bridge to be 3 Hz, and for office buildings the natural frequency of floor structures need to be kept within 4 Hz.

There are three general ways to reduce vibration. The first is to suppress the source of excitation. This method is called isolation. However, in some applications like earthquakes there is nothing that the designer can do about the source. The second way consists in redesign the system until the vibration levels become acceptable. For example, adding mass to the system so the natural frequency is changed and no resonance occurs. This method is called design modification. The third way is to control the vibration of the system. This is the control method and it needs to absorb or dissipate vibrations through sensing and controlling. An example of this method is a magnetic damper, it changes its damping depending on the electric current received. This current is send by a controller that measures the displacement and takes action according to it.

In other cases, vibrations are really useful. In musical instruments, shakers, and pacemakers. Other examples in engineering applications are compactors, vibratory conveyors, and motors. Vibrations can even help to produce energy through the piezoelectric

effect. To both avoid and produce controlled vibrations we must understand how they are produced and how can we modify them.

1.3 Elements of vibration

Vibration is a term normally used to describe oscillations in a mechanical system. Each vibration has its own magnitude, frequency and phase angle. Magnitude refers to the maximum variation of the displacement, namely is the distance between the equilibrium point and the farthest point in the oscillation. The equilibrium point is a certain point in the space where if the system is released, with zero velocity and no forces are applied, the system would remain at rest. Frequency means the number of cycles per time unit. The phase angle is helpful because it can be used to know the offset between two waves or oscillations.

It is important to note that strictly speaking, vibration and oscillation are not the same. Both last in time converting energy from one type to another. For example, a pendulum converts kinetic energy into potential energy, it oscillates but it does not vibrate. To declare that vibrations are occurring, a special type of energy, namely deformation or elastic potential energy, must appear. However, several authors have proposed different definitions and not always the elastic potential energy is involved. For purposes of this research, the classical definition given at the beginning is sufficient.

There are three main elements for a vibratory system to exist. An element to storage and release potential energy, usually an *spring* or some other item with elasticity. An element to storage and release kinetic energy, could be any *mass* or inertia element. A way to dissipate or loses energy, it can be a physical *damper* or due to the viscosity of the surrounding fluid.

1.3.1 Springs

It can be defined as a mechanical link. This element is normally considered to have no mass or damping. Although the most famous type of spring is a coil spring, there are many different types. In fact, any elastic body can be considered as a spring. For example a curved aluminum foil is deformed and, because of its elasticity, it will tend to recover its original position.

The spring element is frequently represented as shown in Fig. 1.5. The *spring constant* or spring stiffness is represented by k. In the part a) the spring is at its equilibrium position, which means that the force acting on the spring is zero. In this case l represents the free length of the spring. In part b) a force F is applied to the free end

and this causes an elongation of the spring (denoted by x). This F force represents the force required to elongate the spring a x length and can be calculated using

$$F = kx \tag{1.1}$$

by integrating force along the displacement, the work (or potential energy) can be obtained through

$$U = \frac{1}{2}kx^2 \tag{1.2}$$

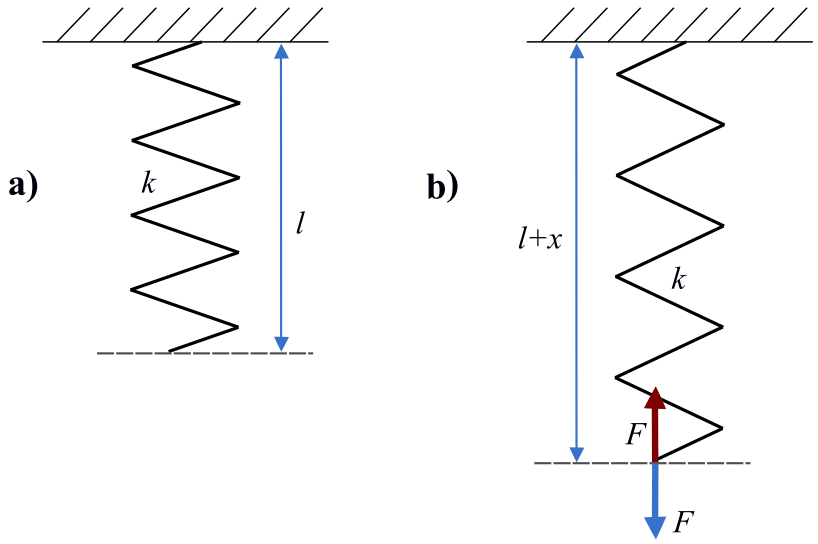

Figure 1.5: Spring element.

An important attribute of a spring is the type of deflection obtained by a constant force applied at the free end. For example, some springs have nonlinearities. This could be achieved by arrangements of simple coil springs, by having a special spring or due to the nature of the object considered as spring. In any case, the important feature here is how the spring force and the displacement are related. Depending if the spring is hard, soft or linear, the force will approach the behavior plotted in Fig. 1.6.

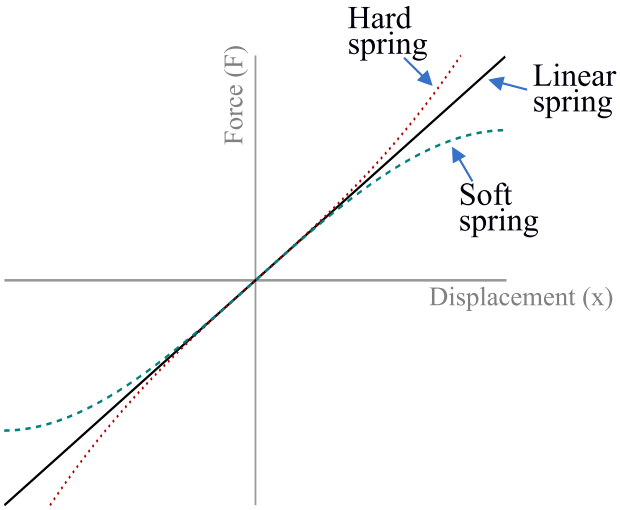

Figure 1.6: Linear and nonlinear springs.

It is important to mention that depending on the material from which the spring is made of, it will have a force displacement curve. If the force applied reach the yield force, the spring would enter at its plastic deformation zone and it will no longer be entirely recovered when the force is eliminated. The spring would, ideally, work only in the elastic deformation zone.

1.3.2 Mass or inertia elements

It normally is a rigid body and it can storage or lose kinetic energy with changes in velocity. Following Newton's second law and its simplification for systems with constant mass:

$$F = \frac{\mathrm{d}(mv)}{\mathrm{d}t} = m\ddot{x} \tag{1.3}$$

where m is the mass of the system, v is the velocity and $\ddot{x}$ means the second derivative with respect to time of the displacement.

Depending on the vibratory system, different parts can be modeled with various masses, see Fig. 1.7. However, in other cases different parts can be replaced by a single equivalent mass. This can be achieved through several mathematical methods. The location of the equivalent mass is assumed and from it, using geometrical lengths, different masses can be clustered in one. The same applies to the inertia elements.

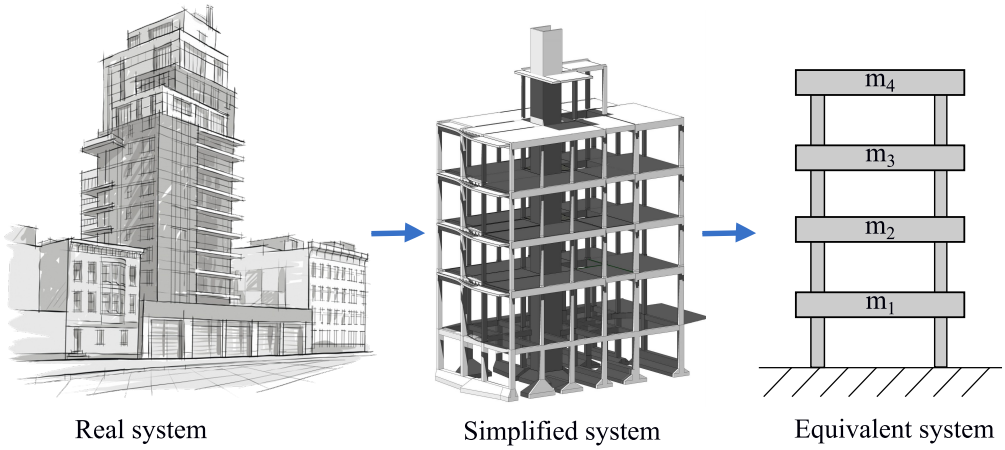

Figure 1.7: Building equivalent system.

1.3.3 Dampers

A vibrating structure has the ability to dissipate energy into heat or other type of energy. This ability is known as damping and its role is to limit the vibrations. There are three types of damping: the structural damping, the matter (or material) damping and the fluid damping. Structural damping is generated by friction. Matter damping is generated by the dissipation of internal energy inside the material. Fluid damping is generated by the dissipation of energy due to the fluid that moves along with the vibrating structure. Usually the most important types of energy dissipation are the structural and the fluid damping.

The viscous or resisting force can be expressed as:

$$F = cv = c\dot{x} \tag{1.4}$$

where c is the damping constant and $\dot{x}$ is the derivative with respect to time of the displacement. The viscous damping is always related to the shear or resisting force and depending on the situation it can be described differently, see Fig. 1.8. In parallel plates separated by viscous fluid it can be expressed as $\tau = \mu {}^{dv}/_{dy}$, the damping constant would be calculated from $F = \tau A = \mu A {}^{dv}/_{dy} = cv$, where A is the area of the plate. In the case of a rotary shaft with lubricated clearance in a bearing, $\tau = \mu {}^{dv}/_{dr}$ and instead of force the torque is used. This means the equation is $T = (\tau A)\, R$, where $A = 2\pi RL$ is the surface area of the shaft exposed to lubricant and R is the radio of the shaft and the damping constant is $c = {}^{T}/_{\omega}$.

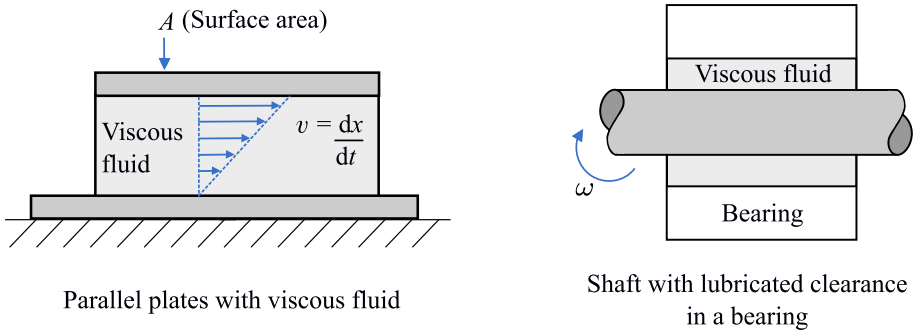

Figure 1.8: Different viscous damping situations.

In some systems exist multiple dampers, and they can be replaced by a single equivalent damper. For constant translational dampers, the equivalent constant can be calculated by $c_{eq} = c_1 + c_2$ if they are parallel placed and by $1/c_{eq} = 1/c_1 + 1/c_2$ if they are placed in series.

1.4 Classification of vibrating systems

Depending on the point of view, there are several ways to classify vibratory systems. These different classifications are explained briefly in the next subsections. First, two distinctive classifications for *systems* are detailed. Then several classification for *vibrations* are given.

1.4.1 Number of degrees of freedom

In the vibrating systems, the number of degrees of freedom (DOF) stands for the minimum independent coordinates required to determine completely the positions of all parts of the system at any time. In the first image, in Fig. 1.9, the Cartesian coordinate x is the only one needed to describe the position of mass at any instant of time. In the second image, the angular coordinate θ can be used to describe motion, one for each inertia element. In the last image, the angular coordinates specifies the positions of the masses.

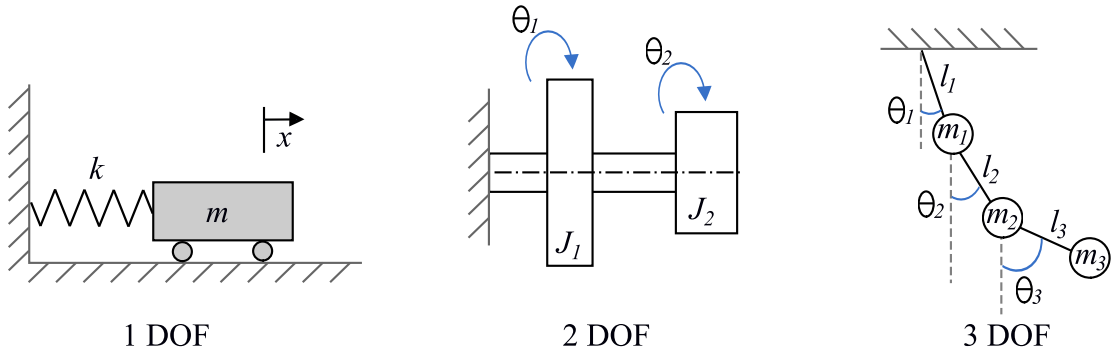

Figure 1.9: Different degrees of freedom in vibratory systems.

In general, the necessary coordinates to describe a system form a set of generalized coordinates. They can be Cartesian or non-Cartesian or both and are usually denoted by $q_1, q_2, q_3, \ldots$

1.4.2 Discrete and continuous systems

Discrete systems are those that have finite numbers of DOF. All systems in Fig. 1.9 are examples of discrete systems and they are also called *lumped parameter* systems.

In some cases the number of DOF can be really high. For example in numerical evaluation such as finite element method. When the number of DOF become infinite, the system pass from discrete to continuous. This last case is also known as *distributed* system.

The same system, depending on the situation, can be analyzed as a continuous or as a discrete model. For example the beam described in Fig. 1.10 might be taken as a continuous system with an analytical solution. Also, the same beam can be simplified and taken as a discrete system with numerical solution.

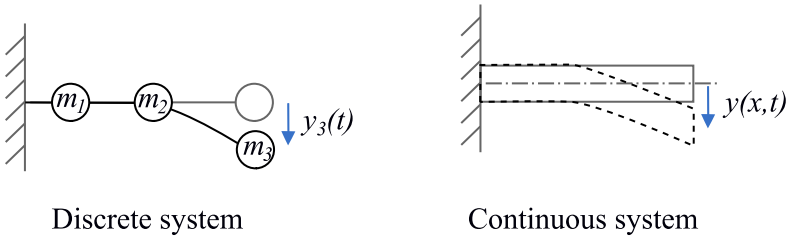

Figure 1.10: Discrete and continuous system.

The following classification categories are based not in the system itself but in the type of vibration that undergoes the system.

1.4.3 Free and forced vibration

In general terms, there are two kinds of mechanical vibrations: free vibrations and forced vibrations. Free vibrations occurs when the body is kept in movement by restoring gravitational or elastic forces. Forced vibrations, on the other hand, are provided by an external periodic or intermittent force. In Fig. 1.11 an example of each type of vibration is shown. Free vibrations can be appreciated in a bow cord. On the other hand, forced vibrations are represented by a swing in which in every oscillation the person add energy by swinging his legs up and down.

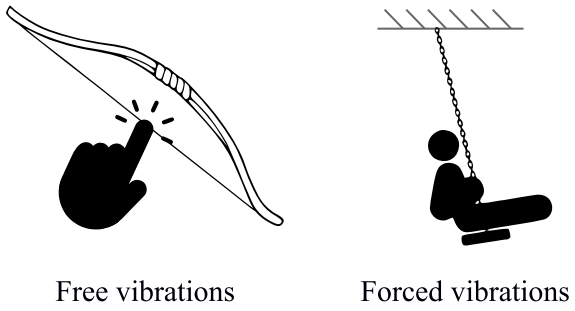

Figure 1.11: Free and forced vibration examples.

1.4.4 Damped and undamped vibration

Both types of vibrations can be damped or undamped. The damped vibrations decrease with time until the system reaches the equilibrium position again. Opposite to that, the undamped vibrations may continue infinitely if the frictional effects are neglected. This is only possible mathematically, being that friction is always present and it acts as a damping force. The response of displacement vs time for both types of vibrations are depicted in Fig. 1.12 for a one degree of freedom system.

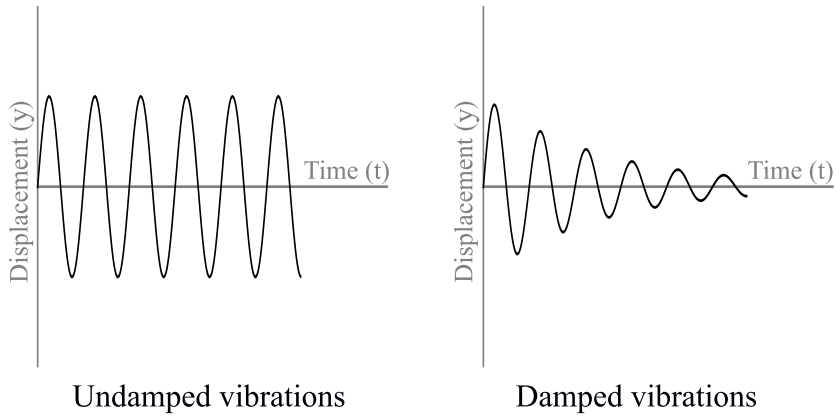

Figure 1.12: Undamped and damped vibrations.

1.4.5 Linear and nonlinear vibration

For a linear vibration system to exist, all the basic components (mass, spring and damper) need to behave linearly. If any of the three elements have a nonlinear behavior, the resulting vibration will be nonlinear. If the vibration is linear, the superposition principle holds. For the nonlinear vibration, the superposition principle is not valid and the problem needs a different approach. Usually, most of the vibratory systems behave (or can be approximated) linearly for small vibrations. However, in many real systems the nonlinearity cannot be avoid. Graphical examples of both linear and nonlinear vibrations are shown in Fig. 1.13.

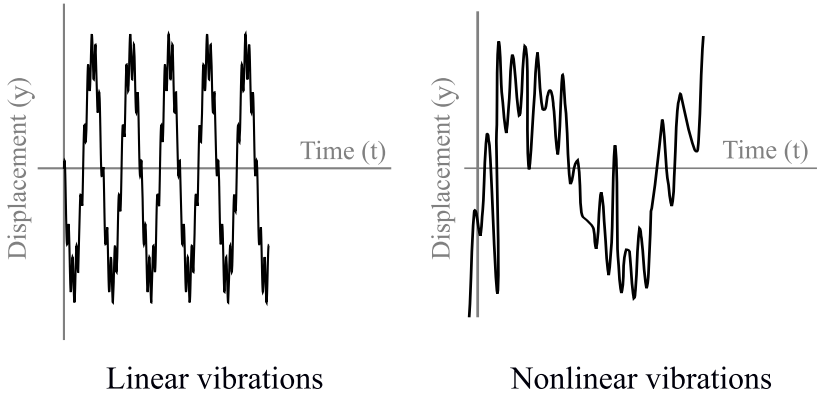

Figure 1.13: Linear and nonlinear vibrations.

1.4.6 Deterministic and random vibration

If the excitation magnitude, force or motion, applied to a vibratory system is known at any instant in time the excitation is called *deterministic* and, therefore, the vibration will be also deterministic. On the other hand if the excitation cannot be predicted it is called *random* or non-deterministic. One of the most common examples of a random vibration is an earthquake, see Fig. 1.14. When a random vibration occurs, a simple approach could be to estimate an average magnitude.

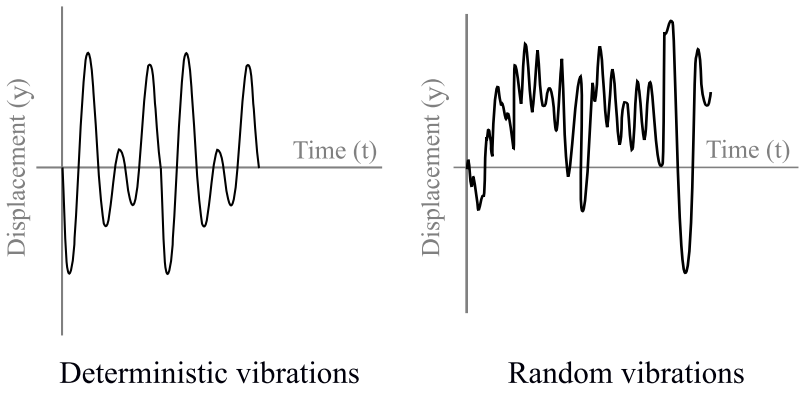

Figure 1.14: Deterministic and random vibrations.

1.5 Vortex-Induced Vibration

From the different types of vibrations studied, one of particular interest is the so-called vortex-induced vibration (VIV). These are self-excited vibrations due to vortex shedding normally in long slender bodies. This type of vibrations occur in a specific region known as 'lock-in'. The classical definition of lock-in is: the regime where the body oscillation frequency (f) and the vortex shedding frequency (f_v) are close to the natural frequency of the structure (f_n), that is $f \approx f_v \approx f_n$ (see Blevins 1990 and Sumer & Fredse 1997). However, on more recent studies a lock-in regime was found at several times the natural frequency (see Moe & Wu 1990, and Khalak & Williamson 1997). One of the most accepted definitions, and the one used as a reference in this thesis, is the one proposed by Sarpkaya (1995). Synchronization, or lock-in, might be defined as the regime where the fluid force frequency must match the shedding frequency. Or as proposed by Khalak & Williamson (1999), synchronization is the matching of the frequency of the periodic wake vortex mode with the body oscillation frequency.

In order to study the lock-in region, and therefore the VIV phenomenon, there are different configurations of experimental apparatus used in the literature. These differ-

ent configurations have unique features that allow different responses and behaviors. Despite the configuration, some data are almost identical and can be used in a broader way. However, that does not always happen and the chosen configuration will affect the equations and assumptions made, and therefore the results.

1.5.1 Types of experimental apparatus

1.5.1.1 Rigid and flexible cylinders

There are two different types of cylinders: the rigid cylinder and the flexible cylinder (see Fig. 1.15). A rigid cylinder has the characteristic of not being deformed by the effect of external forces. In other words, if an axis is plotted along the cylinder, the relative position of any particle to this axis will not change despite the external forces applied to the cylinder. Although a real body is never totally rigid, this kind of cylinders are useful to describe movement (usually considering a continuous mass distribution). Moreover, in a flexible cylinder, the external forces cause deformation. This deformation appears as an opposition to the external force and therefore, when the force is removed the cylinder returns to its original state. What a flexible body experiences is what actually happens, hence, is a more accurate model but also a more complex one. Due to its proximity to the reality, the chosen cylinder for this research was a flexible one.

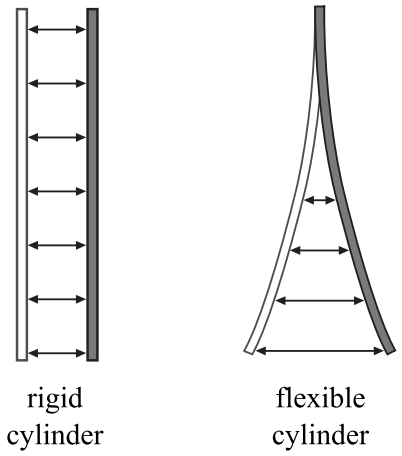

Figure 1.15: Rigid and flexible cylinders.

1.5.1.2 Elastic, pivoted and cantilevered cylinders

In the literature, there are different systems or apparatus to study VIV. Three of those systems are: elastic base system, pivoted rod or pendulum system and cantilevered

bar system (see Fig. 1.16). Each has a different mathematical treatment.

The elastic base system consists of a rigid cylinder mounted on an elastic base. Normally this base allows the cylinder to move only in one degree-of-freedom. And because of the configuration, it is always a two-dimensional phenomenon. Important research concerning this system are those of Jauvtis & Williamson (2004), Stappenbelt & Lalji (2008) and Blevins & Coughran (2009).

The pivoted pendulum system consists of a rigid cylinder mounted in a pivoted pendulum base. It can have one or two degrees-of-freedom, namely, oscillations in the cross-flow and in the in-line directions. This configuration allows the base to have the same natural frequency in both directions. Also the base allows the model to rotate around the Cardan-joint axis at the top of the rigid bar. Some interesting research using this system were carried out by Freire & Meneghini (2010) and Gonçalves et al. (2011).

The cantilevered bar system consists of a flexible cylinder attached to a rigid base. This configuration can have two degrees-of-freedom. Normally, this system has a very low structural damping coefficient and its stiffness depends directly on the length of the cylinder. Usually for this kind of system, the amplitude of the in-line oscillations are less than 10% of the amplitude of the cross-flow oscillations. Some researchers that used this system are: Pesce & Fujarra (2000) and Fujarra et al. (1998). This kind of system is the one used in the present work due to its resemblance to reality.

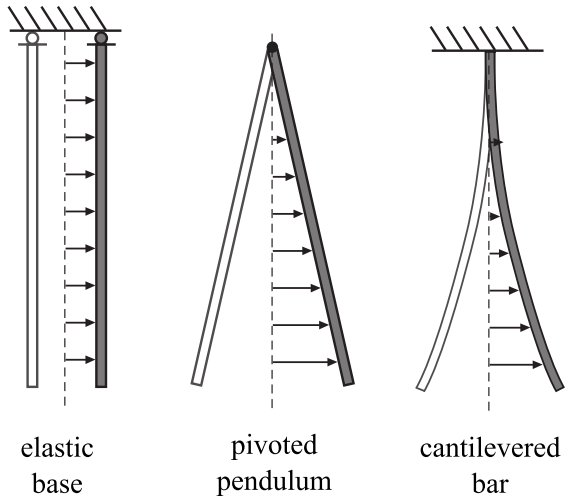

Figure 1.16: Different systems to study VIV.

1.5.1.3 Tapered and uniform

In the literature, different types of cylinders are used (see Fig. 1.17). Tapered cylinders are used to study three-dimensional vortex patterns and/or the span-wise variation of the amplitude of the oscillations. According to Techet et al. (1998) tapered cylinders may produce different hydrodynamic responses along the cylinder. On the other hand, uniform cylinders are most commonly used. They are easier to construct and to model mathematically. Because of this, a uniform cylinder is used in this work.

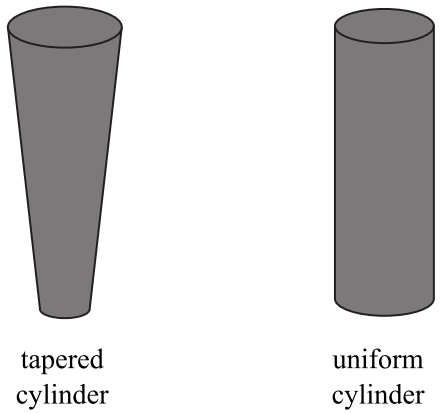

Figure 1.17: Tapered and uniform cylinders.

Once the entire configuration of the experimental apparatus is stated, in this case *a cantilevered uniform flexible circular cylinder*, the mathematical model of the system can be established. Next section indicates some important points about passing from actual problem to differential equations capable of describing the main variables.

1.5.2 Mathematical model

In engineering problems is not always possible to obtain mathematical solutions. Only in a few simple cases an analytic solution is found. When the problem exceeds the complexity of the equations or the methods to solve these equations, simplifications must be made. In spite of the simplifications, results must be capable of achieving certain goals.

The key to pass from a real problem to a mathematical solution is to obtain a mathematical model and, if it is possible, a discretized model. A discretized model includes a symbolic representation of the idealized system and all the simplifications and assumptions made.

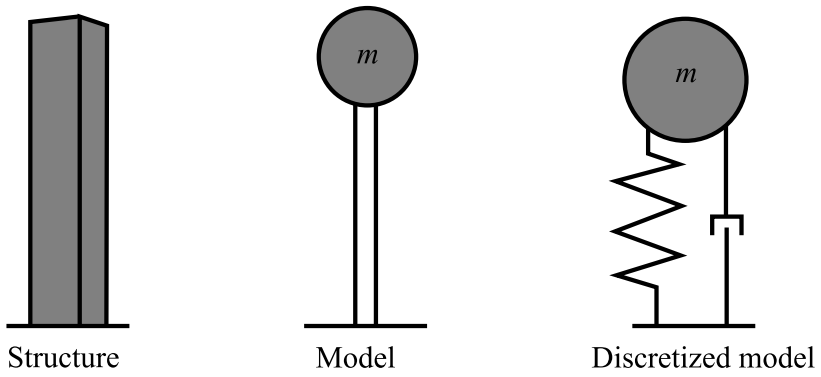

Figure 1.18: Converting a real problem to a mathematical model.

When the structure approaches to a model in which real mass (the one that a weight scale would measure) is replaced by an equivalent mass, the new system is called discretized model. An equivalent mass is a punctual mass connected by springs and dampers with no mass. If the real mass is represented in a distributed form (distributed in physical space), it is said that the system is now a model with distributed parameters.

In this work, the experimental apparatus is a cantilevered uniform flexible circular cylinder under VIV. The mathematical model is a discretized model, and the equation of motion generally used to represent the displacement in the cross-flow direction under this configuration is (Govardhan & Williamson, 2000 and Javitus & Williamson, 2004):

$$m\ddot{y}\left(t\right) + c\dot{y}\left(t\right) + ky\left(t\right) = F\left(t\right) \tag{1.5}$$

where m is the total mass of the system, c is the structural damping, k is the spring constant, and F is the fluid force in the transverse direction. When the body oscillation frequency is synchronized with the periodic wake mode, $F(t)$ can be approximated to:

$$F(t) = F\sin\left(\omega t + \phi\right) \tag{1.6}$$

where

$$y(t) = A\sin\left(\omega t\right) \tag{1.7}$$

in which $\omega = 2\pi f$, and f is the oscillation frequency. The phase angle ϕ represents the offset between the fluid force and the body displacement. Sarpkaya (1979) and

Bearman (1984) pointed out that this phase angle is related to the energy transfer from the fluid to the body, and therefore it influences the amplitude of oscillation.

1.5.2.1 Parameters

As it can be seen from the last section, there are three main parameters in the equation of motion: mass, spring constant, and structural damping coefficient. Each parameter has different features. Here the three elements are ideal, which implies the following facts:

Ideal mass:

- The ideal mass is totally rigid.
- The motion of an ideal mass is not affected by any damping force or friction.

Ideal spring:

- The ideal spring has no mass or internal damping.
- A positive value of y produces a negative restoring force, the spring force represents an opposition to original movement.

Ideal damper (mechanical resistance):

- The ideal damper has no mass and it does not causes a restoring force.
- Force due to viscosity is typically approximated as being proportional to velocity.

1.5.2.2 Forces

As an important part of the mathematical model, forces must be stated and decomposed to deeply understand some concepts, like the vortex formation. Lighthill (1986) shows that the total fluid force, F_{total}, expressed in Eq. 1.8 can be decomposed into a 'potential force', $F_{potential}$, and a 'vortex force', F_{vortex}. He also stated that the vortex force is caused by the dynamics of the 'additional vorticity', where additional vorticity is the entire vorticity in the flow field minus "part of the distribution of vorticity attached to the boundary in the form of a vortex sheet allowing exactly the tangential velocity associated with the potential flow" (Lighthill, 1986). The vortex force is directly related to vortex dynamics, and any change in the vortex force would lead to a change in the vortex formation mode.

$$F_{total} = F_{vortex} - F_{potential} \tag{1.8}$$

where the potential force is due to the added-mass (see sec. 2.4.3.1 for detailed information about added also known as hydrodynamic mass):

$$F_{potential}(t) = m'\ddot{y}\,(t) \tag{1.9}$$

The equation of motion using the vortex force is given by

$$(m + m')\ddot{y}\,(t) + c\dot{y}\,(t) + ky\,(t) = F_v \sin\left(\omega t + \phi_{vortex}\right) \tag{1.10}$$

and the equation of motion using the total force is given by

$$m\ddot{y}\,(t) + c\dot{y}\,(t) + ky\,(t) = F_t \sin\left(\omega t + \phi_{total}\right) \tag{1.11}$$

Once the configuration and equations used to study VIV were stated, in the next sections the different dynamic and hydrodynamic responses found in literature will be briefly explained.

1.5.3 Types of dynamic response in vortex-induced vibrations

According to Khalak & Williamson (1999), two different types of responses exist for an elastically mounted system depending on the mass-damping parameter ($m^*\zeta$), see Fig. 1.19. Where $m^* = 4m/\left(\rho\pi D^2\right)$is the mass ratio and ζ is the damping ratio. In the mass ratio m is the mass per unit length. For a high $m^*\zeta$, experiments like the ones conducted by Feng (1968) and Brika & Laneville (1993) show two different branches of amplitude response with hysteresis in the transition between them. Khalak & Williamson described them as the 'initial' branch, which corresponds to the highest amplitudes reached, and the 'lower' branch. For a low $m^*\zeta$, experiments conducted by Khalak & Williamson (1996, 1997, 1999) show the existence of an additional branch. They find the so-called 'upper' branch and an hysteretic transition from initial to upper branch. On the other hand, transition from upper to lower branch turn out to be an intermittent switching of modes.

Despite the fact that this classification was intended for elastically mounted cylinders, the classification seems to fit with the flexible mounted cylinders as well. For such reason, this classification is used in this thesis. According to the classification and in order to get more information on the lock-in regime, in this research, it was decided to study the low $m^*\zeta$ case.

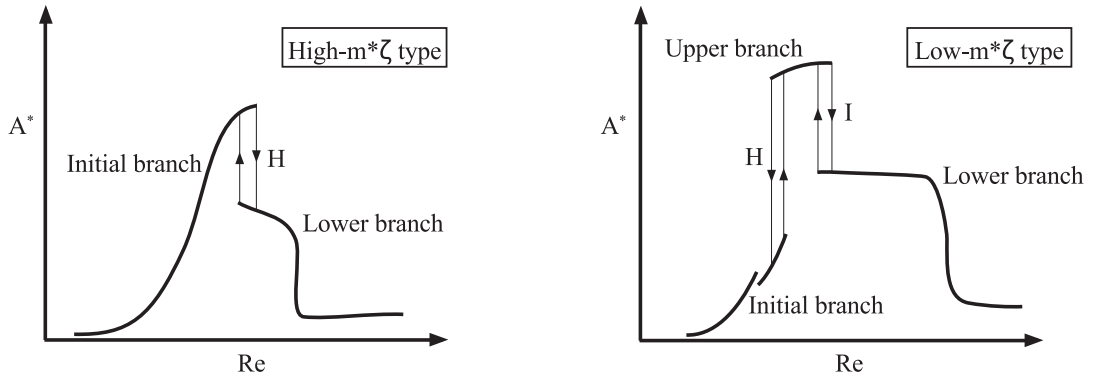

Figure 1.19: Sketches of the two different types of dynamic response. **H** means an hysteretic transition and **I** means an intermittent switching of modes. Based on Govardhan & Williamson (2000).

1.5.4 Types of hydrodynamic response in vortex-induced vibrations

A number of researches have reported different patterns of vortex formation as Re and A^* vary along the lock-in regime (see Fig. 1.20). Griffin & Ramberg (1974) were the first showing, in forced-vibrations experiments, that an asymmetric mode occurs where three vortices per cycle are formed. Also, in forced-vibration studies, Williamson & Roshko (1988), showed different vortex formation modes. These modes were defined as '2S', '2P' and 'P+S'. '2S' indicates two single vortices formed per cycle, '2P' indicates two pair of vortices formed per cycle and 'P+S' indicates a pair of vortices and a single vortex per cycle.

It is important to note that the existence of the '2P' mode in forced transverse vibrations was confirmed by Sheridan et al. (1998) using experimental measurements. Even a hybrid mode where the '2P' and '2S' modes occur at the same time at different spanwise locations along a tapered cylinder was found by Hover & Triantafyllou (1998), also in forced-vibration. However, some two-dimensional numerical simulations, carried out by Meneghini & Bearman (1995) and Blackburn & Henderson (1995), and experiments, by Jeon, Shan & Gharib (1995) and Atsavapranee et al. (1998), do not find the '2P' mode.

Despite the fact that there are works where the '2P' mode does not exist, Williamson & Roshko (1988) suggested that a phase jump, ϕ, corresponds to a change of mode from '2S' to '2P' in forced-vibration experiments. Even more, Brika & Laneville (1993) and Khalak & Williamson (1999) showed independently, in free-vibration experiments, that the jump from the initial branch to the lower branch is directly related to the mode change from '2S' to '2P'. In a similar way, Govardhan & Williamson (2000)

confirmed that a large jump in the 'vortex phase', ϕ_{vortex}, in the initial-upper branch transition is associated with a jump between the '2S' to '2P' vortex wake modes. They also conclude that there is no jump in ϕ_{vortex} at the upper-lower branch transition since both branches are associated with the '2P' mode. However, interestingly, Evangelinos & Karniadakis (1999) concluded that the 'P+S' pattern may be associated with the upper branch.

Besides the vortex formation modes mentioned above, others have been found. The 'P' mode indicates a pair of vortices formed per cycle. Although it may be mistaken as a '2S' mode, the 'P' mode have the vortices of a pair closer and on the same horizontal axis. Other vortex formation mode, the 'C' mode, is defined as a vortex coalescence and is rarely seen.

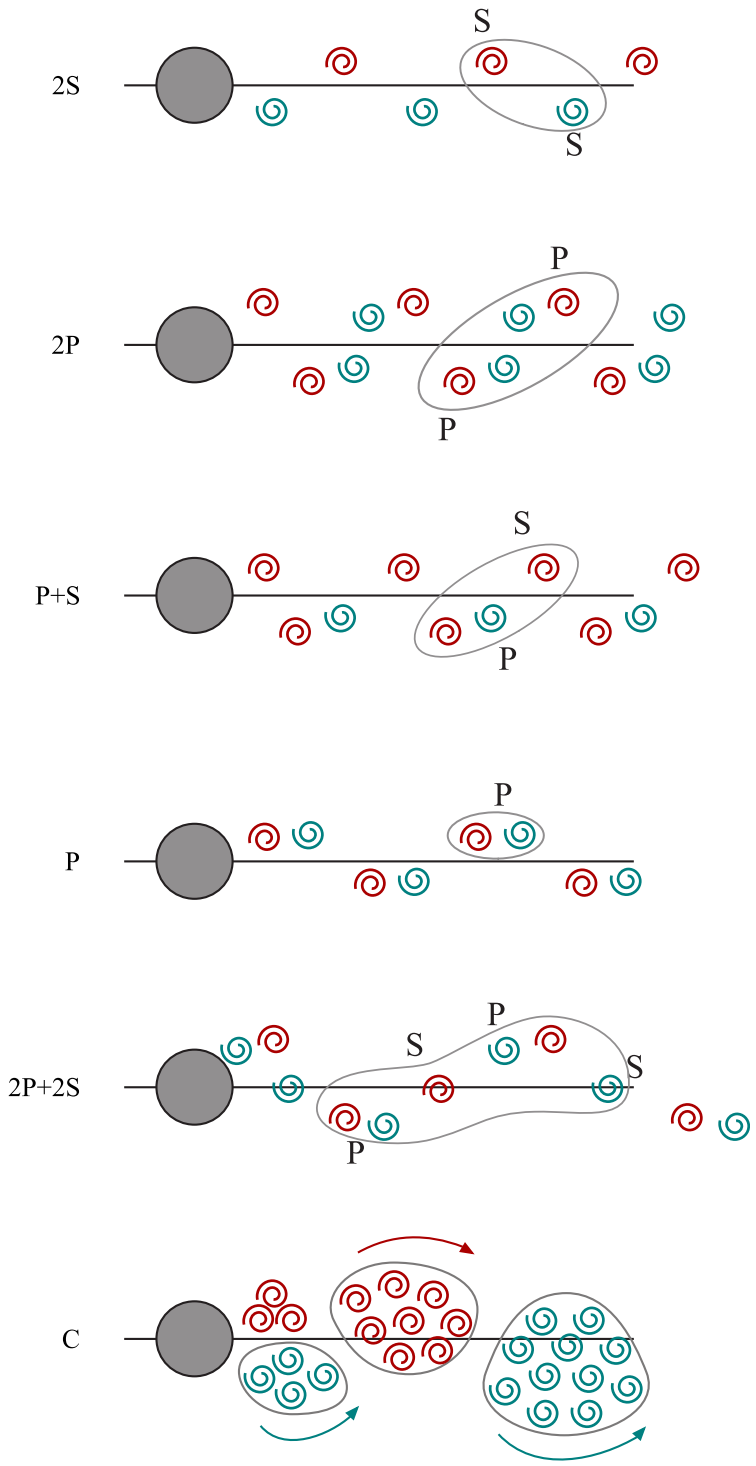

Figure 1.20: Sketches of the vortex shedding patterns found in Vortex-Induced Vibrations. **S** means a single vortex and **P** means a vortex pair, each pattern is defined by the number of pairs and single vortices formed per cycle. Gray lines encircles the vortices shed in one complete cycle. Based on Williamson & Roshko (1988).

2 Theory of vortex induced vibrations

In this chapter four main topics are developed. First, some theory about vibrating systems and solutions of motion equations are offered. Secondly, a wide explanation about vibration modes and different mathematical models to obtain the natural frequency is offered. Later, flow around cylinders is reviewed. Finally, forces in cylinders are studied starting with a cylinder in steady current and ends with a more complicated case like a cylinder in oscillatory current. Even though the topics explained in this chapter are not exclusive of VIV, they are necessary to understand the phenomena present in it. In the fifth section important topics in VIV are presented, with the concepts developed earlier, which are part of the particular objectives of this thesis.

2.1 Solutions to vibration equation

A vibrating structure, sketched in Fig. 2.1, has three forces acting on it: a spring force, a damping force and a force on the structure. The spring force, namely $-ky$, is based on k the spring constant and y the displacement of the structure from the equilibrium position. The damping force, $c\dot{y}$, is due to c the viscous damping coefficient and the velocity of the system. Finally the force on the structure, $F(t)$, depends on external factors acting on the system.

The differential equation that governs the motion of the structure is:

$$F(t) = m\ddot{y}(t) + c\dot{y}(t) + ky(t) \tag{2.1}$$

where m is the total mass of the system (see sec. 1.5.2.1 for more detailed information).

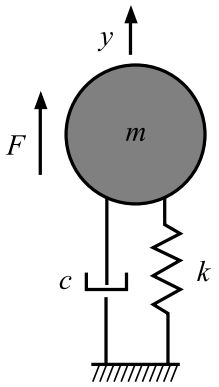

Figure 2.1: Sketch of a flexibly-mounted system vibrating in y direction.

2.1.1 Free vibrations without viscous damping

In this case, no external forces are acting on the structure. $F(t) = 0$ (free vibrations) and the damping is null, $c = 0$. The equation is now

$$m\ddot{y} + ky = 0 \tag{2.2}$$

The solution to this equation is

$$y = A\cos(\omega_v t) + B\sin(\omega_v t) \tag{2.3}$$

where ω_v is the angular frequency of the motion, namely

$$\omega_v = \sqrt{\frac{k}{m}} \tag{2.4}$$

2.1.2 Free vibrations with viscous damping

The damping must be considered, but the external forces are still zero. The equation can be written as

$$m\ddot{y}(t) + c\dot{y}(t) + ky(t) = 0 \tag{2.5}$$

Here the solution is of the form

$$y = C_1 \exp(r_1 t) + C_2 \exp(r_2 t) \tag{2.6}$$

where $r_1 = \frac{1}{2m}\left(-c + \sqrt{c^2 - 4mk}\right)$and $r_2 = \frac{1}{2m}\left(-c - \sqrt{c^2 - 4mk}\right)$. Depending on the value of m, c and k, three different cases may occur. Only two are of interest for the present work (both responses are shown in Fig. 2.2):

Over-damped case ($c^2 > 4mk$) In which r_1 and r_2 have real values. Considering $y(0) = A_y$ and $\dot{y} = 0$, the solution will be:

$$y = \frac{A_y}{r_1 - r_2}\left(r_1 \exp(r_2 t) - r_2 \exp(r_1 t)\right) \tag{2.7}$$

This type of motion is referred to as 'aperiodic' motion.

Under-damped case ($c^2 < 4mk$) In which r_1 and r_2 are complex. The real part of the solution, considering the same initial conditions as in the over-damped case, may be written as:

$$y = A_y \exp\left(-\frac{c}{2m}t\right)\cos(\omega_{dv} t) \tag{2.8}$$

where A is the amplitude of vibrations at time $t = 0$, and the angular frequency is given by

$$\omega_{dv} = \sqrt{\frac{k}{m} - \left(\frac{c}{2m}\right)^2} \tag{2.9}$$

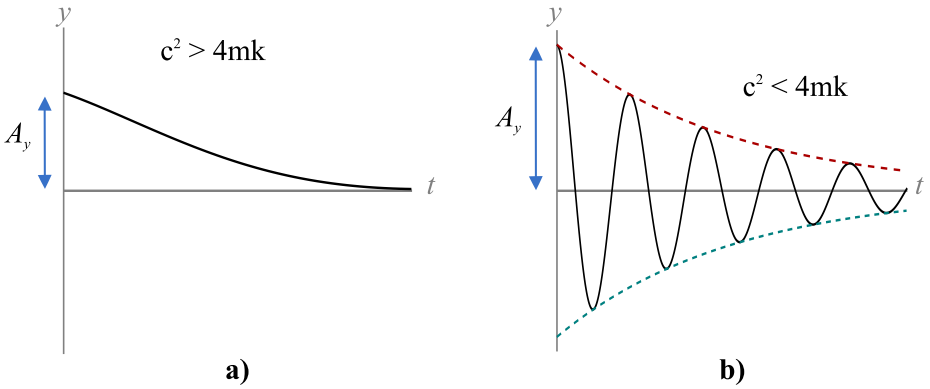

Figure 2.2: Free vibrations with viscous damping. a) over-damped case with no vibration, and b) underdamped case the oscillations decrease with time.

2.1.3 Forced vibrations with viscous damping

In this case, there is an external force acting on the system, $F(t)$. Now the equation is in its full form, Eq. 2.82. If the external force takes the form $F = F_0 \cos(\omega t)$, where ω is the angular frequency associated with the force, the general solution would be:

$$y = A_y \exp\left(-\frac{c}{2m}t\right) \cos(\omega_{dv} t) + C_1 \cos(\omega t) + C_2 \sin(\omega t) \tag{2.10}$$

The first term in this equation represents the case when $F = 0$, and with the time its contribution to the movement of the system will be zero. Therefore, the other two terms will govern the movement and the system will have the same angular frequency as the force, ω.

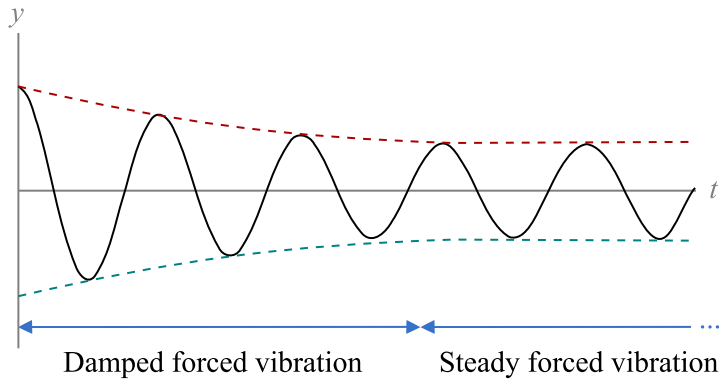

Figure 2.3: Forced vibrations with viscous damping.

The case when only the two last terms of the Eq. 2.10 affect the structure is known as steady forced vibrations. The solution may then be written as

$$y = A\cos\left(\omega t - \phi\right) \tag{2.11}$$

where

$$A = \sqrt{C_1^2 + C_2^2} = \frac{F_0}{k}\left[\frac{1}{\sqrt{\left(1 - \frac{\omega^2}{\omega_v^2}\right)^2 + \left(\frac{c}{m\omega_v}\right)^2\left(\frac{\omega}{\omega_v}\right)^2}}\right] \tag{2.12}$$

and

$$\phi = \tan^{-1}\left(\frac{C_1}{C_2}\right) = \tan^{-1}\left[\frac{\left(\frac{c}{m\omega_v}\right)\left(\frac{\omega}{\omega_v}\right)}{1 - \left(\frac{\omega}{\omega_v}\right)^2}\right] \tag{2.13}$$

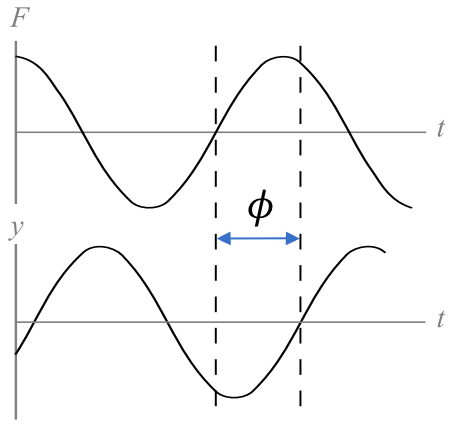

Figure 2.4: Phase delay (ϕ) illustration.

2.1.4 Damping

2.1.4.1 Structural damping

If a rigid cylinder is suspended with springs in still water and displaced from its equilibrium position and then released, the cylinder would start to oscillate. These oscillations will eventually disappear due to damping (structural plus fluid damping). To separate the structural damping, the structure should be placed in vacuum. Only in this case the damping will be caused merely by the structural damping.

For the simplest case, consider a structure in vacuum with free vibrations and with no damping. The equation will be

$$m\ddot{y} + ky = 0 \tag{2.14}$$

and the solution will be written as

$$y = A_y \cos(\omega_v t) \tag{2.15}$$

where $\omega_v = \sqrt{k/m}$, will be the angular frequency of an undamped free vibrations system in vacuum.

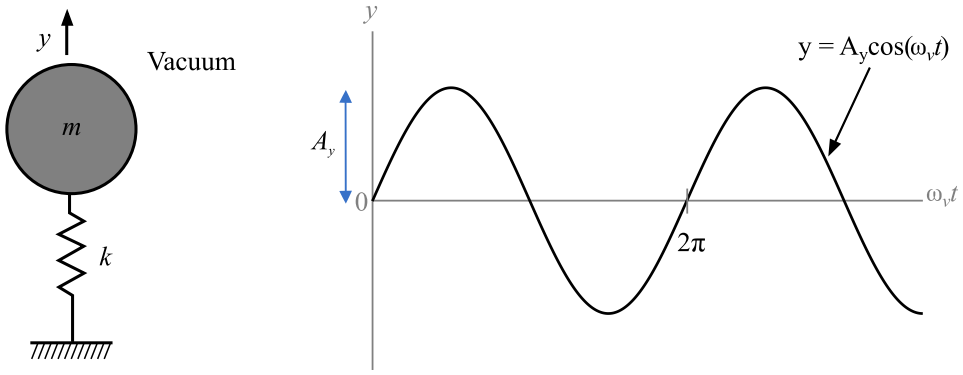

Figure 2.5: Free vibrations in vacuum without damping.

Now consider the last system with damping. Since the structure is placed in vacuum, the damping force will only correspond to the structural damping. The equation to

solve will be

$$m\ddot{y} + c\dot{y} + ky = 0 \tag{2.16}$$

and its solution

$$y = A_y \exp\left(-\frac{c}{2m}t\right)\cos\left(\omega_{dv}t\right) \tag{2.17}$$

where ω_{dv} corresponds to Eq. 2.9. For convenience, the damping coefficient may be written as

$$\zeta_s = \frac{c}{2m\omega_{dv}} \tag{2.18}$$

Eq. 2.18 is the definition of the structural damping factor. Re-writing the solution:

$$y = A_y \exp\left(-\zeta_s\omega_{dv}t\right)\cos\left(\omega_{dv}t\right) \tag{2.19}$$

in which

$$\omega_{dv} = \omega_v\sqrt{\frac{1}{1+\zeta_s^2}} \tag{2.20}$$

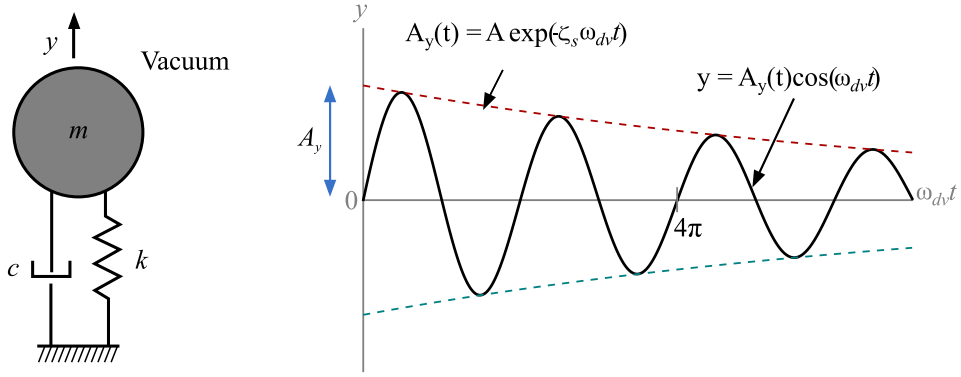

Figure 2.6: Free vibrations in vacuum with damping.

2.1.4.2 Fluid damping in still fluid

Finally, consider a damped and free vibrations system in otherwise still fluid. The difference with the last system is that the vibrations will decay faster in a fluid than in vacuum. This is due to the fact that the fluid damping is added to the structural damping.

When the cylinder is oscillating, the Morison force acts and the mass is no longer m but rather $m + m'$. An additional hydrodynamic resistance force is present, which can be observed as an increment in the total damping.

The equation for this case will be

$$(m + m')\ddot{y} + c\dot{y} + \frac{1}{2}\rho C_D D \left|\dot{y}\right| \dot{y} + ky = 0 \tag{2.21}$$

and its solution will be written as

$$y = A_y \exp\left(-\zeta\omega_d t\right) \cos\left(\omega_d t\right) \tag{2.22}$$

where the angular frequency, ω_d, is given by

$$\omega_d = \omega_n \sqrt{1 - \zeta^2} \tag{2.23}$$

reminding that

$$\omega_n = \sqrt{\frac{k}{m + m'}} \tag{2.24}$$

and ζ is the total damping (considering both structural and fluid damping)

$$\zeta = \zeta_s + \zeta_f \tag{2.25}$$

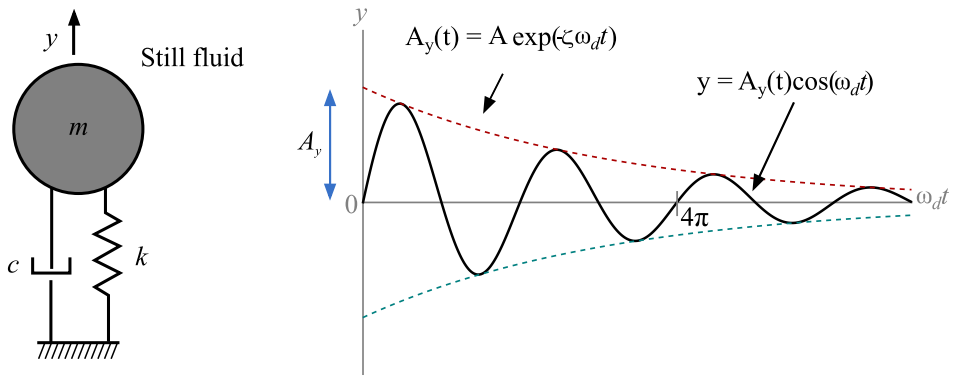

Figure 2.7: Free vibrations in still fluid with damping.

2.1.4.3 Measurement of damping

Testing is the 'easiest' way to determine the damping of a system. This is usually done in air and/or in water. One of the main techniques used for measuring of damping is the free decay. It consists on applying a known excitation to the structure (move the system from its equilibrium point), record the response of the structure and find the damping by matching the theoretically predicted response with the recorded results.

If y_n and y_{n+1} were two consecutive amplitudes recorded in the experiment (see Fig. 2.8), the ratio of both will be

$$\frac{y_n}{y_{n+1}} = \frac{A_y \exp\left(-\zeta\omega_n t\right)}{A_y \exp\left(-\zeta\omega_n \left(t+T\right)\right)} = \exp\left(\zeta\omega_n T\right) \tag{2.26}$$

in which T is the period of the vibration

$$T = \frac{2\pi}{\omega_d} \tag{2.27}$$

From the Eq. 2.26 and 2.23, ζ is obtained as:

$$\zeta = \frac{\delta}{\sqrt{\delta^2 + (2\pi)^2}} \tag{2.28}$$

where the quantity $\delta = \ln\left(y_n/y_{n+1}\right)$is known as logarithmic decrement.

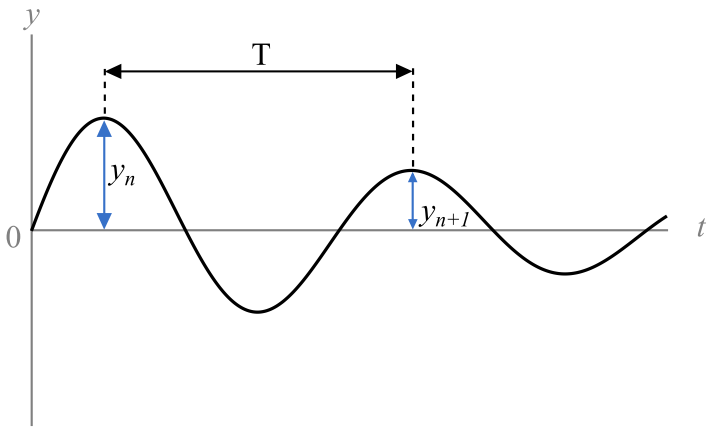

Figure 2.8: Recorded response of the structure in a free decay experiment.

2.2 Natural frequencies and vibration modes

There are different methods to determine the natural frequencies and the mode shapes of a body. For example, the Dunkerley's formula, the Rayleigh's method, the Holzer's method, the Jacobi's method, the matrix iteration method and the standard eigenvalue method. The majority of these methods are beyond the scope of this thesis. To be more specific, only the mathematical analysis of a single degree of freedom and a continuous system considering the Euler-Bernoulli equation cantilevered beam is presented here.

2.2.1 Frequencies of lumped systems

A lumped system is also a single degree of freedom system. Consider a uniform slender beam in cantilever with length l, mass m and properties k, E, I with a concentrated mass M at the free end. In order to lump the beam mass and the concentrated mass, an equivalent mass at the free end must be found by using the equivalence kinetic energy.

First consider the free-body diagram of the beam shown in Fig. 2.9. The static deflection is:

$$y(x) = \frac{Px^2}{6EI}(3l - x) = \frac{Mgx^2}{6EI}(3l - x) = \frac{y_{max}}{2l^3}(3lx^2 - x^3) \tag{2.29}$$

where P is a force acting in the free end of the cantilever beam and g is the gravity.

The maximum kinetic energy of the beam is given by:

$$KE_{max} = \frac{1}{2}\int \frac{m}{l}\left[\dot{y}(x)\right]^2 dx \tag{2.30}$$

where the integral is from 0 to l. By substituting $y(x)$, the Eq. 2.30 becomes

$$KE_{max} = \frac{m}{2l}\left(\frac{\dot{y}_{max}}{2l^3}\right)^2 \int (3lx^2 - x^3)^2 dx = \left(\frac{m}{2l}\right)\left(\frac{\dot{y}^2_{max}}{4l^6}\right)\left(\frac{33}{35}l^7\right) = \frac{1}{2}\left(\frac{33}{140}m\right)\dot{y}^2_{max} \tag{2.31}$$

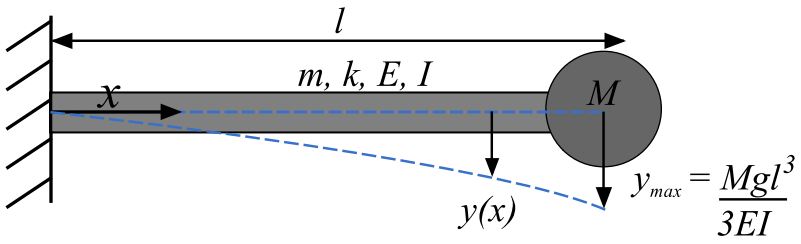

Figure 2.9: Beam undergoing transverse vibrations. Where $y(x)$ is the transverse deflection measured from its static equilibrium point.

Since the maximum kinetic energy is half the mass multiplied by the square of the velocity, this means:

$$KE_{max} = \frac{1}{2}m_{eq}\dot{y}^2_{max} \tag{2.32}$$

From Eq. 2.32 it can be deduced that:

$$m_{eq} = \frac{33}{140}m \tag{2.33}$$

The natural frequency of transverse vibration of the beam with a concentrated mass

is given by:

$$\omega_n = \sqrt{\frac{k}{M_{eff}}} = \sqrt{\frac{k}{M + \frac{33}{140}m}} \tag{2.34}$$

where M_{eff} is the effective mass acting at the end of the cantilever beam. If the concentrated mass is removed, then a simple lumped cantilever beam system will remain, see Fig. 2.10. It can be deduced that the natural frequency is:

$$\omega_n = \sqrt{\frac{k}{\frac{33}{140}m}} \tag{2.35}$$

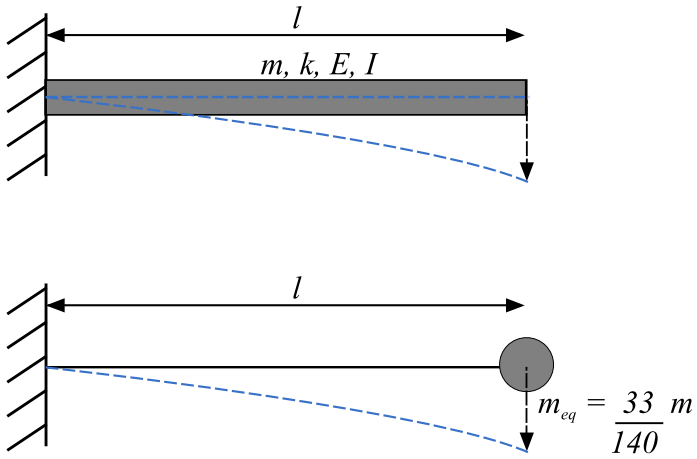

Figure 2.10: Lumped beam undergoing transverse vibrations.

2.2.2 Frequencies of continuous systems

First consider a uniform beam of mass density ρ and elastic modulus E with a length L and a cross-sectional area A, which leads to a moment of inertia I (see Fig. 2.11). The x axis is placed in the neutral axis of the beam and along it an external load per unit length, $f(x,t)$, exists. Finally, the transverse deflection is measured from the x axis and is denoted by $w(x,t)$.

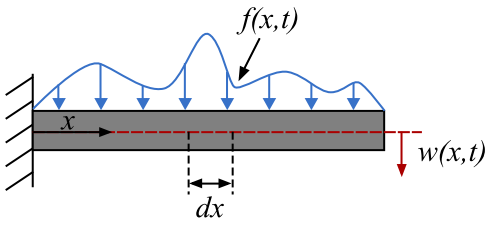

Figure 2.11: Beam undergoing transverse vibrations. Where $w(x,t)$ is the transverse deflection measured from its static equilibrium point.

If a differential element of the beam is taken, the external force acting on it will be the one shown in Fig. 2.12. This is known as external loading $f(x,t)$, and it causes internal bending moment M, and the internal shear force V. There are other forces involved but they are small in comparison, so their effects are ignored.

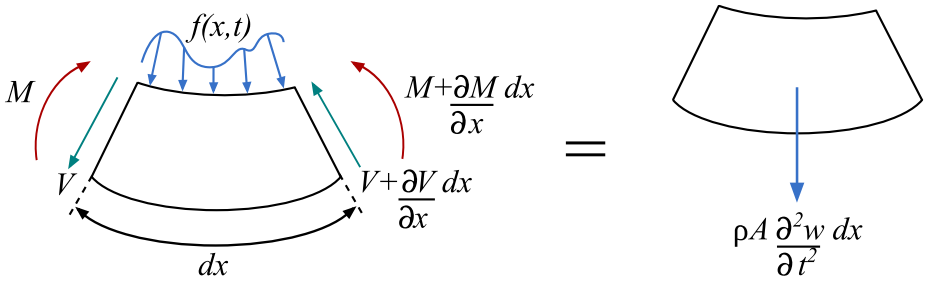

Figure 2.12: Free-body diagram of differential beam element. The left part represents the external forces and the right side, the effective forces following Newton's law.

The sum of forces in vertical direction is:

$$V - \left(V + \frac{\partial V}{\partial x}dx\right) + \int f(\varsigma,t)d\varsigma = \rho A \frac{\partial^2 w}{dt^2}dx \tag{2.36}$$

where the integral is from x to $x+dx$, and the variable ς is the curvature created due to bending. The mean value theorem implies that there is an $\overline{x}$ where

$$\int f(\varsigma,t)d\varsigma = f(\overline{x},t)dx$$

and since dx is infinitesimal, $\overline{x} \approx x$, so Eq. 2.36 becomes:

$$f(x,t) - \frac{\partial V}{\partial x} = \rho A \frac{\partial^2 w}{dt^2} \tag{2.37}$$

Now, the sum of moments about the left side of the beam in Fig. Fig. 2.12 is:

$$M - \left(M + \frac{\partial M}{\partial x}dx\right) - \left(V + \frac{\partial V}{\partial x}dx\right)dx + \int (\varsigma - x)\, f(\varsigma, t)\, d\varsigma = \rho A \frac{\partial^2 w}{dt^2} dx \left(\frac{dx}{2}\right) \tag{2.38}$$

in Eq. 2.38 there are terms of order $(dx)^2$, which are negligible compared to terms of order dx. Also, mean value theorem is used on the integral and since $\varsigma - x$ is smaller than dx, it can be deduced that the integral is also of order $(dx)^2$. The only terms left are:

$$V = -\frac{\partial M}{\partial x} \tag{2.39}$$

The internal bending moment in the cantilever beam, from mechanics of materials, is:

$$M = -EI\frac{\partial^2 w}{dx^2} \tag{2.40}$$

where the second derivative of its deflected shape with respect to x is interpreted as its curvature, E is the Young's modulus and I is the area moment of inertia of the cross-section. Substituting these results in 2.37:

$$f(x,t) - EI\frac{\partial^4 w}{dx^4} = \rho A \frac{\partial^2 w}{dt^2} \tag{2.41}$$

This equation can be nondimensionalized by:

$$x^* = \frac{x}{L},\, t^* = t\sqrt{\frac{EI}{\rho A L^4}},\; w^* = \frac{w}{L},\; f^* = \frac{f}{f_m}$$

where f_m is the maximum value of $f(x,t)$. These substitutions leads to:

$$\frac{f_m L^3}{EI} f^* - \frac{\partial^4 w^*}{dx^{*4}} = \frac{\partial^2 w^*}{dt^{*2}} \tag{2.42}$$

Finally, the *s have been dropped from nondimensional variables and the equation is now:

$$\frac{f_m L^3}{EI} f - \frac{\partial^4 w}{dx^4} = \frac{\partial^2 w}{dt^2} \tag{2.43}$$

Since the nondimensionalized equation is of fourth order, four boundary conditions, two at $x = 0$ and two at $x = 1$ must be specified. The boundary conditions depend on the supports of the beam. These conditions must have a physical meaning, in the nondimensional form: the deflection is w, the slope of deflection is $\partial w/\partial x$, the internal bending moment is $\partial^2 w/\partial x^2$, and the internal shear force is $\partial^3 w/\partial x^3$.

2.2.2.1 Free vibration in vacuum

Vibrations here are free, this means that $f(x,t) = 0$. The equation of motion is given by:

$$\frac{\partial^4 w}{dx^4} + \frac{\partial^2 w}{dt^2} = 0 \tag{2.44}$$

The boundary conditions for the fixed end in $x = 0$ are:

$$w = 0, \text{and } \frac{\partial w}{\partial x} = 0$$

and the boundary conditions for the free end in $x = 1$ are:

$$\frac{\partial^2 w}{\partial x^2} = 0, \text{and } \frac{\partial^3 w}{\partial x^3} = 0$$

In order to solve the equation, the method of separation of variables is used. The product solution is $w(x,t) = X(x)T(t)$. This leads to:

$$\frac{1}{T}\frac{d^2 T}{dt^2} = -\frac{1}{X}\frac{d^4 X}{dx^4}$$

and equaling both sides to a constant:

$$\frac{d^2T}{dt^2} + \lambda T = 0, \text{and } \frac{d^4X}{dx^4} - \lambda X = 0$$

The solutions to these equations are:

$$T(t) = A\cos\left(\lambda^{1/2}t\right) + B\sin\left(\lambda^{1/2}t\right) \tag{2.45}$$

$$X(x) = C_1\cos\left(\lambda^{1/4}x\right) + C_2\sin\left(\lambda^{1/4}x\right) + C_3\cosh\left(\lambda^{1/4}x\right) + C_4\sinh\left(\lambda^{1/4}x\right) \tag{2.46}$$

Applying the boundary conditions, the five lowest nondimensionalized natural frequencies for this specific case correspond to $\omega_k = \sqrt{\lambda_k}$: $\omega_1 = 3.51$, $\omega_2 = 22.03$, $\omega_3 = 61.70$, $\omega_4 = 120.9$, and $\omega_5 = 199.9$. The corresponding dimensional natural frequency is

$$\bar{\omega}_k = \omega_k\sqrt{\frac{EI}{\rho AL^4}} \tag{2.47}$$

The mode shape is

$$X_k(x) = C_k\left[\cosh\left(\lambda^{1/4}x\right) - \cos\left(\lambda^{1/4}x\right) - \alpha_k\left(\sinh\left(\lambda^{1/4}x\right) - \sin\left(\lambda^{1/4}x\right)\right)\right] \tag{2.48}$$

, where $\alpha_k = \frac{\cos\left(\lambda_k^{1/4}\right)+\cosh\left(\lambda_k^{1/4}\right)}{\sin\left(\lambda_k^{1/4}\right)+\sinh\left(\lambda_k^{1/4}\right)}$. C_k can be calculated with the kinetic energy scalar product

$$\int X_j(x)X_k(x)dx \tag{2.49}$$

the integral is from 0 to 1. This yields to:

$$C_i = \frac{1}{\sqrt{\int\left[\cosh\left(\lambda_i x\right) - \cos\left(\lambda_i x\right) - \alpha_i\left(\sinh\left(\lambda_i x\right) - \sin\left(\lambda_i x\right)\right)\right]^2 dx}} \tag{2.50}$$

Fig. 2.13 represents the five normalized lowest mode shapes.

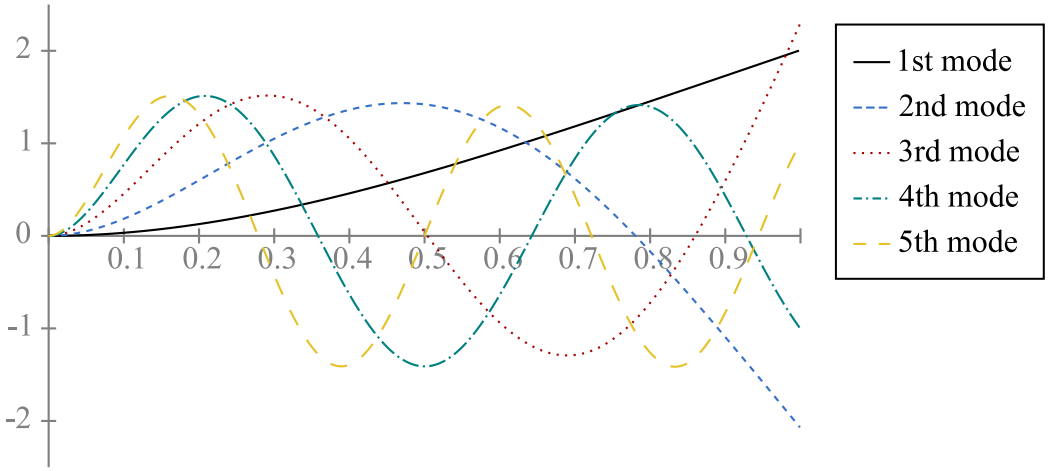

Figure 2.13: Five lowest mode shapes.

The natural frequency depends on the eigenvalues, λ_k, and on cylinder properties such as Young's modulus, moment of inertia, density, cross-sectional area and length. Neither of them depends on the orientation of the cylinder.

2.2.2.2 Free vibration in water

In order to simulate a cantilever beam in free vibration in water, the effect of water is represented by its damping. Eq. 2.44 applies to this problem. Instead of a free end, in $x = 1$, the beam has a viscous damper (see Fig. 2.14). The new boundary conditions are:

$$\frac{\partial^2 w}{\partial x^2} = 0, \text{and } EI\frac{\partial^3 w}{\partial x^3} = c\frac{\partial w}{\partial t}$$

where the solutions are of the form:

$$w(x,t) = W(x)e^{\lambda t} \tag{2.51}$$

$W(x)$ is a complex function in general, and λ is the eigenvalue of the system which is also complex in general. The detailed solution for the free vibration response is carried out in (Gürgöze, 2006). When the beam vibrates at λ frequency, the absolute values of $W(x)$ represent the amplitude distribution over it.

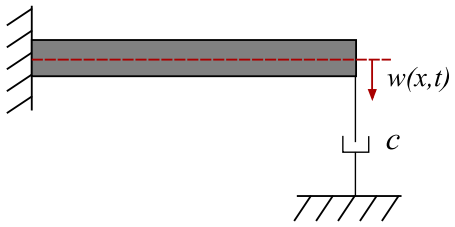

Figure 2.14: Beam undergoing free vibrations with a viscous damper simulating water. Where $w(x,t)$ is the transverse deflection measured from its static equilibrium point.

In this work, the amplitude is considered only at the tip of the cylinder. In order to solve the natural frequency at the tip of a cantilever cylinder, Eq. 2.44 was used with its corresponding boundary conditions (Gürgöze, 2006) and the eigenvalues are obtained by setting to zero the determinant of the dynamic stiffness matrix ($\det\mathbf{K}(\overline{\beta},\mu)=0$). The dynamic stiffness matrix is:

$$K = \frac{EI}{1+e^{2i\overline{\beta}}-4e^{(1+i)\overline{\beta}}+e^{2\overline{\beta}}+e^{(2+2i)\overline{\beta}}}\begin{bmatrix}\alpha_F & \alpha\\ \alpha & \alpha_M\end{bmatrix} \tag{2.52}$$

where

$$\beta^4 = -\frac{\rho A}{EI}\lambda^2 \quad \overline{\beta}=\beta L \quad \mu = \frac{c\lambda}{EI\beta^3}$$

$$\alpha_F = \beta^3\left\{(1-i)+e^{2\overline{\beta}}\left[(-1-i)+\mu\right]+e^{(2+2i)\overline{\beta}}\left[(-1+i)+\mu\right]+\mu-4e^{(1+i)\overline{\beta}}\mu+e^{2i\overline{\beta}}\left[(1+i)+\mu\right]\right\}$$

$$\alpha = i\beta^2\left(-1+e^{2i\overline{\beta}}\right)\left(-1+e^{2\overline{\beta}}\right)$$

$$\alpha_M = \beta\,(1+i)\left(-1+ie^{2i\overline{\beta}}-ie^{2\overline{\beta}}+e^{(2+2i)\overline{\beta}}\right)$$

where c is a lumped viscous damping parameter that represents the effect of water

as the working fluid. Finally the different frequencies, each one associated with one eigenvalue, are given by 2.53:

$$\omega_i^2 = (\beta_i L)^4 \frac{EI}{\rho A L^4} \tag{2.53}$$

2.3 Flow around a cylinder in steady current

2.3.1 Regimes of flow around a smooth circular cylinder

The Reynolds number (Re), is a non-dimensional quantity used to describe similar flow patterns in fluid flows under different circumstances. It is defined as the ratio between the inertial and the viscous forces, which highlights the importance of each force for a given flow condition. In the case of flow around a smooth circular cylinder, it is defined as:

$$\mathrm{Re} = \frac{inertial\ forces}{viscous\ forces} = \frac{\rho D U}{\mu} = \frac{DU}{\nu} \tag{2.54}$$

where D is the diameter of the cylinder, U is the main flow velocity, and ν is the kinematic viscosity.

The flow is subjected to enormous changes as the Re increase from zero. Fig. 2.15 shows the different regimes of flow classified according to the Reynolds number. As it can be seen (Fig. 2.15a), for very small Re there are no separation, it only occurs when $\mathrm{Re} > 5$. For $5 < \mathrm{Re} < 40$, a fixed pair of vortices appear in the wake of the cylinder (Fig. 2.15b), which length, according to Batchelor (1967), increases with the Re.

When Re exceeds a value of 40, the flow is no longer stable and a phenomenon called vortex shedding shows up. This event consists in the shedding of vortices alternately to either side of the cylinder, normally with a very specific frequency. This is normally known as a "vortex street" (Fig. 2.15d-f). In the range $40 < \mathrm{Re} < 200$, the vortex street is fully laminar and it does not vary along the cylinder (is a 2-D phenomenon).

When Re increases, the flow starts a transition from laminar to turbulent. As stated by Bloor (1964), in the range $200 < \mathrm{Re} < 300$ this transition moves towards the cylinder, and once $\mathrm{Re} = 400$ the vortices formed are turbulent. According to the work of Gerrard (1978) and Williamson (1988) in the range $200 < \mathrm{Re} < 300$ the vortices are shed in different cells along the cylinder, so the phenomena is now 3-D. It is important

to notice that although the wake can be partially turbulent, the boundary layer over the cylinder remains still laminar.

Even for the subcritical range, $300 < \mathrm{Re} < 3 \times 10^5$, the boundary layer stays laminar despite the fact that the wake is now completely turbulent (Fig. 2.15e). Beyond this point, $3 \times 10^5 < \mathrm{Re} < 3.5 \times 10^5$, the range is known as the critical flow regime. Here the boundary layer starts to become turbulent at the separation point but only in one side of the cylinder (Fig. 2.15f). This turbulence in the boundary layer causes a non-zero mean lift on the cylinder. According to Schewe (1983), the side of the cylinder at which the turbulent separation occurs may switch and consequently the lift changes its direction.

In $3 \times 10^5 < \mathrm{Re} < 3.5 \times 10^5$ the regime is known as the supercritical flow regime. Here the boundary layer separation is turbulent on both sides of the cylinder, but the transition to turbulent flow in the boundary layer is not complete. The transition from laminar to turbulent is somewhere between the stagnation point and the separation point (Fig. 2.15g). Beyond $\mathrm{Re} = 1.5 \times 10^6$, the boundary layer is totally turbulent on one side of the cylinder. The other side is partially laminar and partially turbulent. This type of response corresponds to the so-called upper transition flow regime, $1.5 \times 10^6 < \mathrm{Re} < 4 \times 10^6$. Further this last value, $\mathrm{Re} = 4 \times 10^6$, the boundary layer is turbulent everywhere and is referred to as the transcritical flow regime (Fig. 2.15i).

a)	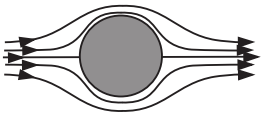	No separation / Creeping flow	$Re < 5$
b)	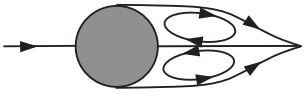	A fixed pair of symmetric vortices	$5 < Re < 40$
c)	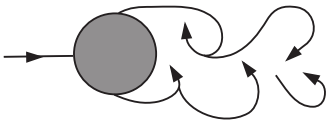	Laminar vortex street	$40 < Re < 200$
d)	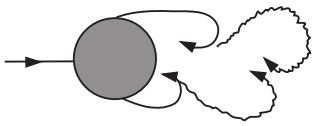	Transition to turbulence in the wake	$200 < Re < 300$
e)	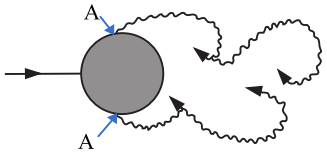	Wake completely turbulent	$300 < Re < 3 \times 10^5$ Subcritical
f)	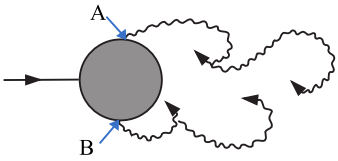	One side with a laminar and the other with turbulent boundary layer separation (still both sides with a laminar boundary layer)	$3 \times 10^5 < Re < 3.5 \times 10^5$ Critical (Lower transition)
g)	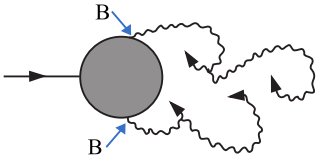	Both sides with turbulent boundary layer separation (both sides with partly laminar partly turbulent boundary layer)	$3.5 \times 10^5 < Re < 1.5 \times 10^6$ Supercritical
h)	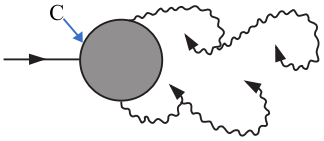	Boundary layer completely turbulent at one side	$1.5 \times 10^6 < Re < 4 \times 10^6$ Upper transition
i)	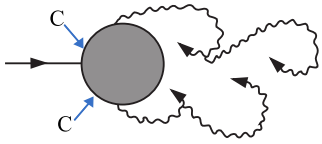	Boundary layer completely turbulent at both sides	$4 \times 10^6 < Re$ Transcritical

Figure 2.15: Regimes of flow around a smooth circular cylinder in steady current. **A**: laminar boundary layer separation; **B**: turbulent boundary layer separation; and **C**: turbulent boundary layer separation with boundary layer completely turbulent.

The preceding regimes are based mainly in the work of Roshko (1961) and Schewe (1983). However, there is no general classification well accepted by the entire scientific community.

2.3.2 Vortex shedding

As mentioned in the last section, for Re $>$ 40 the vortex shedding phenomenon appears. For those cases, the boundary layer separates from the cylinder surface due to the adverse pressure gradient, which is imposed by the divergent geometry of the flow environment at the rear side of the cylinder. This event forms a shear layer (Fig. 2.16).

The boundary layer formed contains a certain vorticity that feeds the shear layer, formed downstream the separation point, and yields the shear layer to roll up into a vortex . This vortex has the same sign of the incoming vorticity (see vortex A in Fig. 2.16). Likewise, on the other side of the cylinder occurs the same phenomenon but with a lag time, forming other vortex (see vortex B in Fig. 2.16).

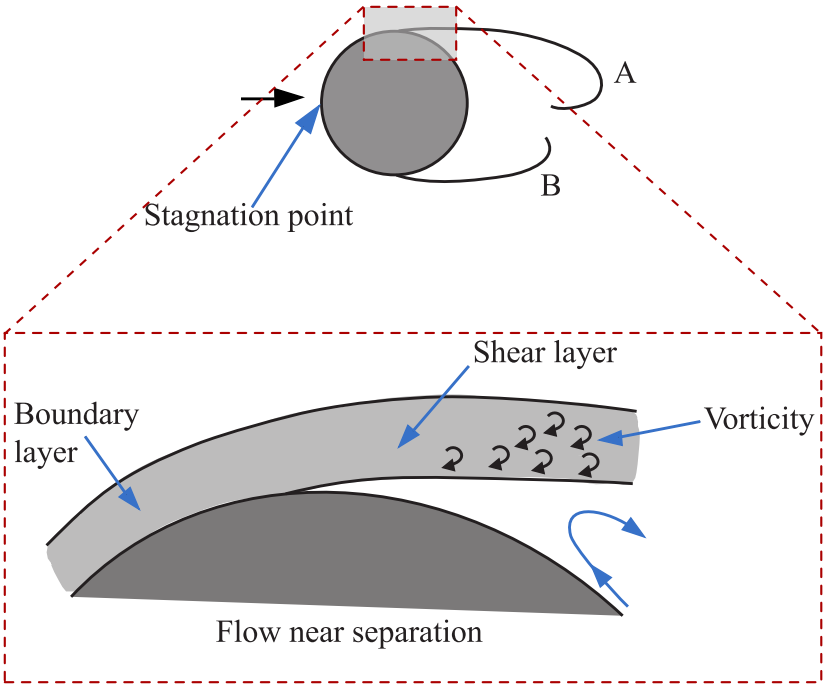

Figure 2.16: The shear layer. The shear layer roll up to form a vortex, one for each side of the cylinder. Based on Sumer & Fredsøe (1997).

The pair of vortices formed due to the shear layer is unstable when is exposed to small disturbances. This leads one vortex to grow larger than the other. The larger vortex

throws the other vortex toward the wake due to the asymmetric flow (see Fig. 2.17). One vortex spins in the clockwise direction while the other spins in the anticlockwise direction. This difference will cut off the supply of vorticity from the boundary layer to one vortex and will cause the shedding of it. As a free vortex, it will be drawn downstream by the main flow.

The vortex shedding only happens when the two shear layers (one at each side of the cylinder) interact with each other. If this interaction between the layers is affected somehow, no vortex shedding will occur. Some ways to prevent the interaction consist of placing a horizontal plate at the rear side of the cylinder, or to place the cylinder close enough to a wall, among others.

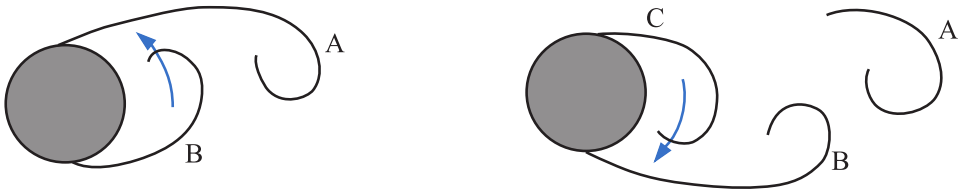

Figure 2.17: Vortex shedding mechanism. In the first scheme, the vortex **A** is larger and throws the vortex **B** across the wake. In the second scheme, the vortex **B** has grown enough to throw the vortex **C** across the wake. This mechanism is repeated in an alternate manner at each side of the cylinder to form the "vortex street". Based on Sumer & Fredsøe (1997).

2.3.2.1 Vortex-shedding frequency

As the Reynolds number is used to describe flows, there is a dimensionless number that helps to describe an oscillatory flow. This number depends on the normalization of the vortex shedding frequency:

$$\mathrm{St} = \mathrm{St}\,(\mathrm{Re}) = \frac{f_v D}{U} \tag{2.55}$$

where f_v is the vortex shedding frequency, D is the diameter of the cylinder and U is the main flow velocity. This normalized vortex shedding frequency is known as the Strouhal number (St).

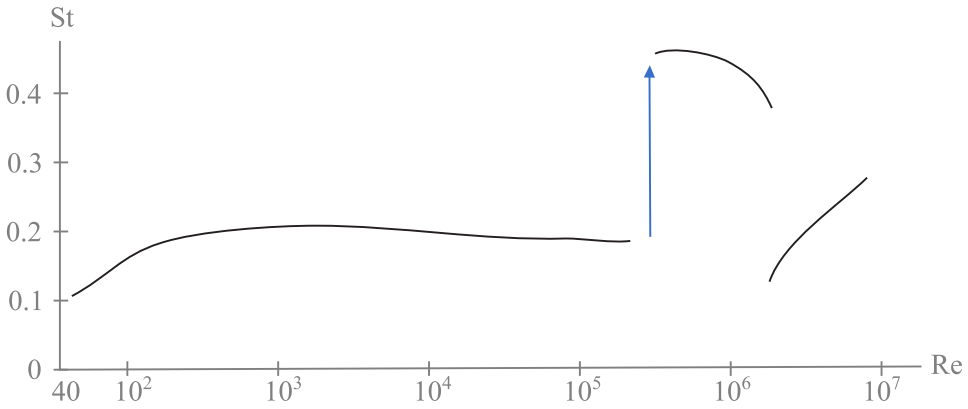

Figure 2.18: Sketch of the Strouhal number for a smooth circular cylinder. Based on experimental data from: Williamson (1989), Roshko (1961), and Schewe (1983).

When the vortex shedding first appears, the St number takes a value of approximately 0.1 (see Fig. 2.18). It increases until Re $\backsimeq$ 300, from this value onwards the St number stays practically at a constant value of 0.2. The St number change its value again when Re $= 3 \times 10^5$, suddenly it jumps from 0.2 to 0.45. At this point, Re $= 3 \times 10^5$, the boundary layer is turbulent at the separation point on both sides of the cylinder. The outcome is a delay in the boundary layer separation where the separation point moves downstream (see Fig. 2.19). Now that the vortices are closer to each other, the interaction is faster than before and the shedding vortex increases drastically, the same as the St number.

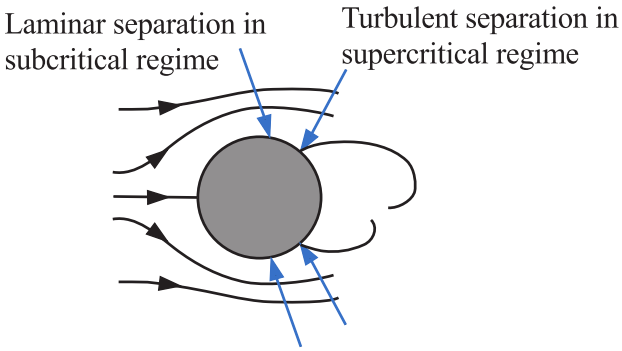

Figure 2.19: Sketch of the separation points. Based on Sumer & Fredsøe (1997).

At Re $= 1.5 \times 10^6$, the St number jumps again, but this time its value decreases. At this point, the boundary layer at one side of the cylinder is turbulent and laminar on the other side. This asymmetry inhibits the vortex interaction partially and the vortex shedding becomes irregular. This behavior changes when Re overpass the value of 4.5×10^6; there, the St number takes a value of 0.25-0.30.

2.4 Forces on cylinders

2.4.1 Forces in steady current

Because of the flow around a circular cylinder, two forces will appear. One caused by the pressure and one due to the friction. The total mean resultant force due to pressure per unit length is:

$$\overline{F}_p = \int \overline{p} \cdot r_0 d\phi \tag{2.56}$$

While the total resultant force due to friction is:

$$\overline{F}_f = \int \overline{\tau}_0 \cdot r_0 d\phi \tag{2.57}$$

in which $\overline{p}$ is the time-averaged pressure and $\overline{\tau}_0$ is the time-averaged wall shear stress on the cylinder surface. The geometry used in these integrals is shown in Fig. 2.20. In this section, all the integrals are defined for $d\phi$ from 0 to 2π.

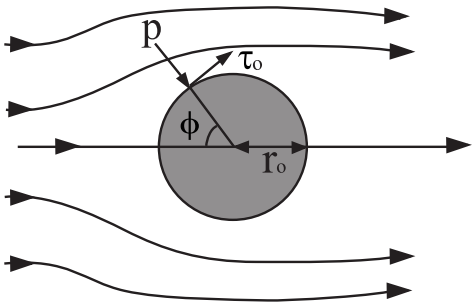

Figure 2.20: Definition sketch.

Besides the above method, there are other way to classify these forces depending on the direction in which they are applied. The total in-line force, known as the mean drag, is the sum of the corresponding component of the Eq. 2.56 and 2.57:

$$\overline{F}_D = \int \overline{p} \cdot \cos(\phi) \cdot r_0 d\phi + \int \overline{\tau}_0 \cdot \sin(\phi) \cdot r_0 d\phi \tag{2.58}$$

While the total cross-flow force, known as the mean lift, is:

$$\overline{F}_L = \int \overline{p} \cdot \sin(\phi) \cdot r_0 d\phi + \int \overline{\tau}_0 \cdot \cos(\phi) \cdot r_0 d\phi \tag{2.59}$$

In this case this last force, $\bar{F}_L$, will be null due to symmetry in the flow. Nevertheless, the instantaneous cross-flow component is non-zero and its value can be large.

2.4.2 Drag and lift

The forces, as well as the flow itself, vary as the Re number is changed, but also when the surface roughness, the cross-sectional shape and the incoming turbulence change. Independently of these changes, the vortex shedding phenomenon is always present.

Due to vortex shedding, the pressure distribution is different as the vortex shedding process goes on. These changes are periodic and they will result in the variation of the force components around the cylinder.

As Fig. 2.21 shows, the drag force acting on the cylinder will oscillate around the mean value and will always be positive or in the same direction. The lift force, on the other hand, changes its direction and it may have a zero value in a specific time. However, both forces vary periodically along the vortex shedding process.

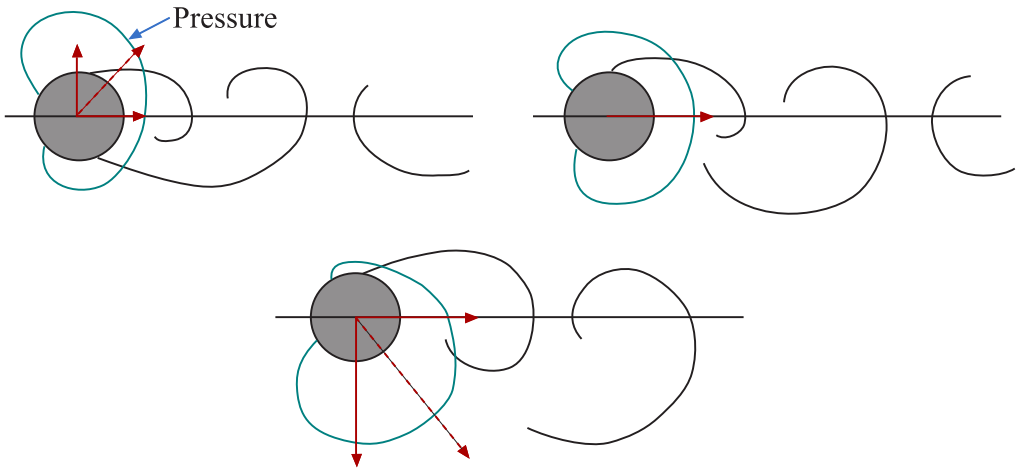

Figure 2.21: Sketch of time development of pressure distribution at different moments of the vortex shedding process. Based on Drescher (1956).

2.4.2.1 Mean drag

Form drag and friction drag For $Re > 10^4$, Achenbach (1968) proved that the form drag (or in-line pressure force) represents the 97-98% of the total drag force. For practical purposes, the friction drag can be omitted in most of the cases.

Following this idea, Fig. 2.22 shows the pressure distribution obtained from the potential flow theory, which is given by:

$$\overline{p} - p_0 = \frac{1}{2}\rho U^2 \left(1 - 4\sin^2\phi\right) \tag{2.60}$$

where p_0 is the hydrostatic pressure. As it can be seen, the measured pressure distribution is negative at the rear side of the cylinder. In contrast, the potential flow theory gives a significantly different result. One may think that as a result of separation, the pressure on the cylinder remains constant at the rear side because the flow in the wake is very weak compared to the outer-flow. This result is important because it shows that sometimes the potential flow theory is not close to reality, and the outcomes obtained with it cannot always be applied to certain problems.

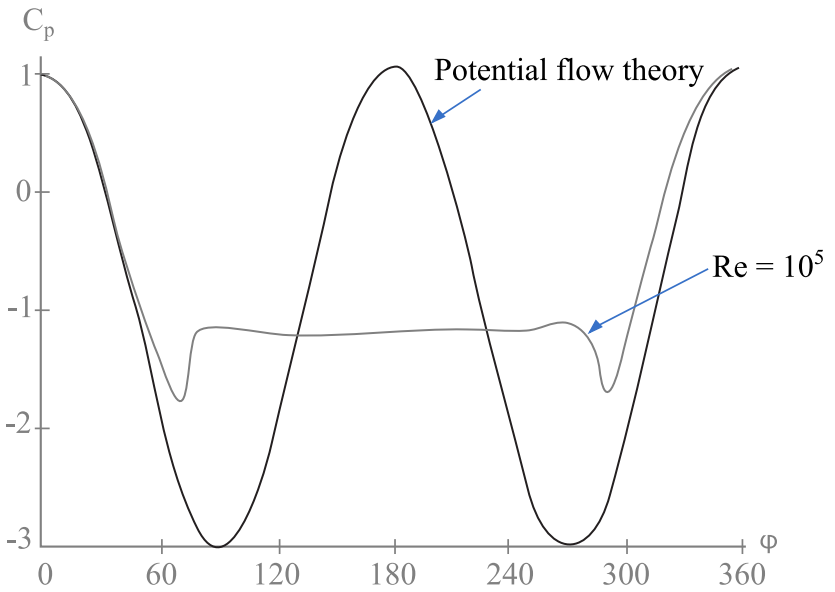

Figure 2.22: Sketch of pressure distributions, potential flow theory and Re = 10^5. Based on Achenbach (1968).

Drag coefficient The drag force can be calculated as

$$\overline{F}_D = \int \left(\overline{p}\cos\left(\phi\right) + \overline{\tau}_0 \sin\left(\phi\right)\right) r_0 d\phi \tag{2.61}$$

manipulating the equation, it can be written as

$$\frac{\overline{F}_D}{\frac{1}{2}\rho D U^2} = \int \left[\left(\frac{\overline{p} - p_0}{\rho U^2}\right)\cos\left(\phi\right) + \left(\frac{\overline{\tau}_0}{\rho U^2}\right)\sin\left(\phi\right)\right] d\phi \tag{2.62}$$

where $D = 2r_0$, is the cylinder diameter and $d\phi$ is defined from 0 to 2π. The right-hand of the Eq. 2.62 is a function of Re. Consequently, it can be written in the form

$$\frac{\overline{F}_D}{\frac{1}{2}\rho D U^2} = \overline{C}_D \tag{2.63}$$

where C_D is known as the mean drag coefficient or drag coefficient.

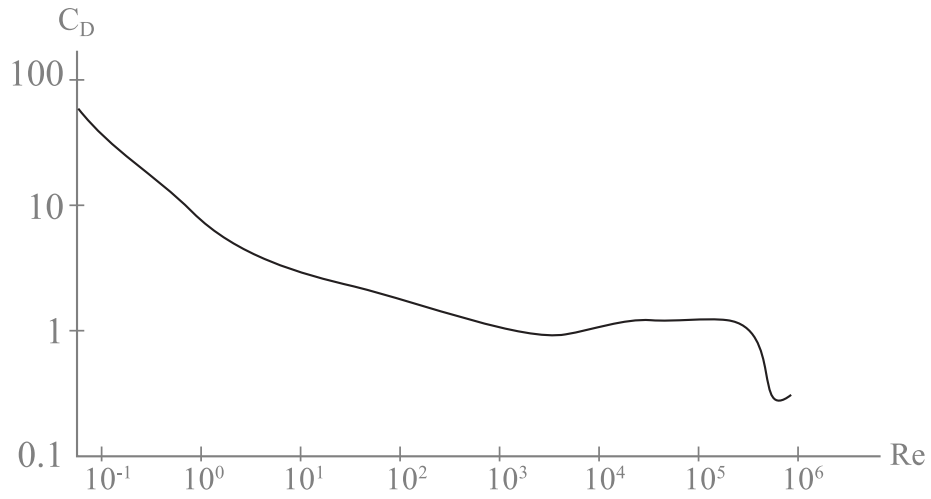

Figure 2.23: Drag coefficient for a smooth circular cylinder as function of the Re number. Based on data from: Schewe (1983) and Schlichting (1979).

Fig. 2.23 present the behavior of the drag coefficient when Re varies. A critical point occurs when $\mathrm{Re} = 3 \times 10^5$, here the drag coefficient drops drastically. This is known as the drag crisis and it can be explained with the pressure diagrams (see Fig. 2.24).

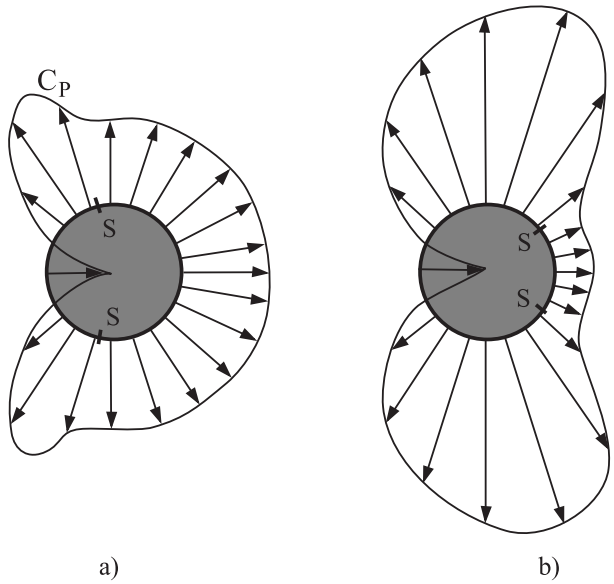

Figure 2.24: Pressure distributions. **S** denotes the separation points. a) Circular cylinder in the subcritical regime, and b) Circular cylinder in the supercritical regime. Based on Achenbach (1968).

The separation points moves from $\phi = 78^\circ$ in a laminar separation, to $\phi = 140^\circ$ in turbulent separation. This results in a narrow wake with a smaller negative pressure, which will lead to a smaller drag coefficient.

2.4.3 Drag force in oscillatory flow

Now that the forces and its origin were explained. Forces in oscillatory flows, which are more like those on VIV, will be explained in detail in this section. The drag force in a steady current is given by:

$$F_D = \frac{1}{2}\rho C_D D U\,|U| \tag{2.64}$$

in which F_D is the in-line force per unit length of the cylinder and C_D is the drag force coefficient. Here, instead of writing U^2, the expression is $U\,|U|$, so the force can conserve the sign (direction) of the velocity. For oscillatory flows, where $U =$

$U_m \sin(\omega t)$, the drag force has two more components, namely:

$$F_D = \frac{1}{2}\rho C_D D U |U| + m'\dot{U} + \rho V \dot{U} \tag{2.65}$$

in which the second term of the right hand is the hydrodynamic mass force and the third term is the Froude-Krylov force; here m' denotes the hydrodynamic mass and V is the volume of the cylinder.

2.4.3.1 Hydrodynamic mass force

In order to understand the hydrodynamic mass, one might think of a plate submerged into still water. When the plate moves from rest in the horizontal position (see Fig. 2.25a), it undergoes practically no resistance. When the plate moves from rest in the vertical position, Fig. 2.25b, not only the plate but also the fluid surrounding, is moving along. This phenomenon occurs due to the pressure from the plate. This mass of fluid that is accelerated with the plate due to the pressure, is known as the hydrodynamic mass. The existence of the hydrodynamic mass means that the total force to move the body is not $F = ma$ but $F = (m + m')a$, where m is the mass of the solid object and a is the acceleration.

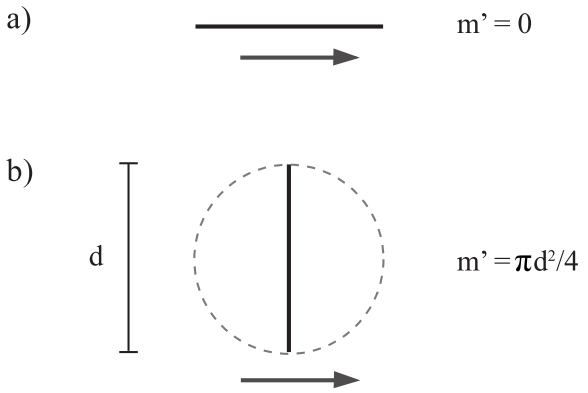

Figure 2.25: Movement of a plate in a still fluid; a) horizontal plate, and b) vertical plate. Based on Sumer & Fredsøe (1997).

The hydrodynamic mass is normally calculated excluding the frictional effects. That is to say that the flow is calculated using only the pressure forces and the inertia forces. As a result, the hydrodynamic mass may be calculated using potential flow theory.

In order to known m' for a body in still water, first the body needs to be accelerated, later the flow field around the body needs to be calculated (if it is possible using potential flow theory). With the flow field the pressure on the surface of the body can be known, and finally the force on the body due to pressure may be determined.

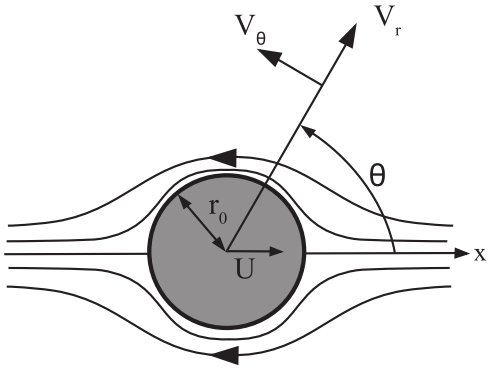

Figure 2.26: Sketch of potential flow around an accelerated cylinder moving in the x axis at U velocity in otherwise still fluid.

Considering the case sketched in Fig. 2.26, the velocity potential is given by (Milne-Thomson, 1962),

$$\phi = U\frac{r_0^2}{r}\cos(\theta) \tag{2.66}$$

from which the velocity components can be obtained:

$$v_\theta = -\frac{1}{r}\frac{\partial\phi}{\partial\theta} = U\frac{r_0^2}{r^2}\sin(\theta) \tag{2.67}$$

$$v_r = -\frac{\partial\phi}{\partial r} = U\frac{r_0^2}{r^2}\cos(\theta) \tag{2.68}$$

Now the pressure around the cylinder can be calculated using the Bernoulli equation

$$\frac{p}{\rho} + \frac{1}{2}v^2 - \frac{\partial\phi}{\partial t} = cte \tag{2.69}$$

in which $v^2 = v_r^2 + v_\theta^2 = U^2(\sin^2(\theta) + \cos^2(\theta)) = U^2$ on the cylinder surface. Since v^2 does not vary with r or θ, the pressure can be written as

$$\frac{p}{\rho} = \frac{\partial \phi}{\partial t} + cte \tag{2.70}$$

Now the pressure can be calculated neglecting the constant term

$$p = \rho \frac{\partial \phi}{\partial t} = \rho \frac{\partial}{\partial t}\left(U \frac{r_0^2}{r} \cos(\theta)\right) = \rho r_0 \cos(\theta) \frac{\partial U}{\partial t} = \rho r_0 a \cos(\theta) \tag{2.71}$$

Integrating around the cylinder, the total force due to pressure is

$$F_{p,s} = -\int \rho r_0 a \cos(\theta)\, d\theta = -\rho r_0^2 a \pi \tag{2.72}$$

The force required to accelerate a cylinder in an otherwise still fluid is

$$F = ma + \rho r_0^2 \pi a = (m + m')\, a \tag{2.73}$$

from where $m' = \rho r_0^2 \pi$. Usually the hydrodynamic mass is written as

$$m' = \rho C_m A \tag{2.74}$$

in which A is the cross-sectional area, for a circular cylinder $A = \pi r_0^2$, and C_m is the hydrodynamic coefficient. For a circular cylinder:

$$C_m = 1 \tag{2.75}$$

It is important to notice that this result is based on several assumptions and simplifications. For example, a circular cylinder with velocity U in otherwise still fluid; frictional effects equal to zero; namely, this calculation implies that the fluid can be described using the potential flow theory. If these requirements are not well accomplished, the C_m needs to be calculated using other techniques.

2.4.3.2 The Froude-Krylov force

As seen in the previous section, the hydrodynamic mass force is caused by the acceleration of the fluid in the nearby surroundings. However the accelerated motion of the fluid in the not-so-close surroundings, outer flow region, will also generate a pressure gradient:

$$\frac{\partial p}{\partial x} = -\rho \frac{dU}{dt} = -\rho a \tag{2.76}$$

where U is the velocity in the main flow, far away from the cylinder. This force will produce an extra force, known as the Froude-Krylov force. This force is also calculated using the pressure:

$$F_{p,f} = -\int p dS \tag{2.77}$$

where S is the surface of the body. Using the Gauss theorem, the equation now is

$$F_{p,f} = -\int \frac{\partial p}{\partial x} dV = \rho V a \tag{2.78}$$

If the body moves in an otherwise still water, there will be no pressure gradient in the outer flow, and therefore there will be no Froude-Krylov force.

2.4.3.3 The Morison equation

The total in-line (drag) force for an accelerated fluid environment, where the cylinder is held stationary, can be calculated using the in-line force in steady current, the hydrodynamic mass force and the Froude-Krylov force. The force F_D is now:

$$F_D = \frac{1}{2}\rho C_D D U |U| + \rho C_m A \dot{U} + \rho A \dot{U} \tag{2.79}$$

Manipulating the equation, it can be written as

$$F_D = \frac{1}{2}\rho C_D D U |U| + \rho \left(C_m + 1\right) A \dot{U} \tag{2.80}$$

$$F_D = \frac{1}{2}\rho C_D D U |U| + \rho C_M A \dot{U} \tag{2.81}$$

where $C_M = C_m + 1$, is referred to as the inertia coefficient. Eq. 2.81 is known as the Morison equation. And in the case of a body that moves relative to the flow in the in-line direction, the Morison equation can be written as:

$$F_D = \frac{1}{2}\rho C_D D \left(U - U_b\right) |U - U_b| + \rho C_m A \left(\dot{U} - \dot{U}_b\right) + \rho A \dot{U} \tag{2.82}$$

where U_b is the b. The last term in Eq. 2.82 only depends on U because this force is associated with the motion of the fluid and not with the motion relative to the body.

Measurements of the C_D and C_M coefficients Nowadays, there are several numerical codes to calculate the flow around and the forces on a circular cylinder in oscillatory flows but they are under development and are not fully able to describe the variation of the force coefficients. Despite technological advances in the numerical field, experiments are still the best source of information at the present time.

2.4.4 Lift force in oscillatory flow

Under an oscillatory flow, a cylinder may experience a lift force. This lift force oscillates at a fundamental frequency different from the one of the flow. The frequency in the lift force depends on the frequency of vortex shedding. That is why if the flow around the cylinder is a creeping flow, no lift will be generated.

For oscillatory flow, a helpful parameter is the so-called Keulegan-Carpenter number (KC). This quantity is equal to:

$$KC = \frac{2\pi a}{D} \tag{2.83}$$

where a is the amplitude of the motion and D is the diameter of the cylinder. Small KC numbers mean that the motion of the water particles is small compared to the total width of the cylinder, therefore separation may not even occur. On the other hand, large KC numbers mean that water particles travel large distances compared to the width of the cylinder, causing separation and vortex shedding. For the vortex

street to exist, KC is approximately 4. Therefore, at this point the lift force starts to grow. In order to have a well-established lift force KC need to be around 6 or 7.

The lift force undergoes two maxima values (see Fig. 2.27), the first and the biggest one at $KC = 10$ and the second when $KC = 16$. Williamson (1989) poses that these peaks may reflect an increase in the repeatability of the shedding patterns. Each peak corresponds to a certain pattern of shedding. The first peak corresponds to a single-pair regime and the second peak corresponds to a double-pair regime.

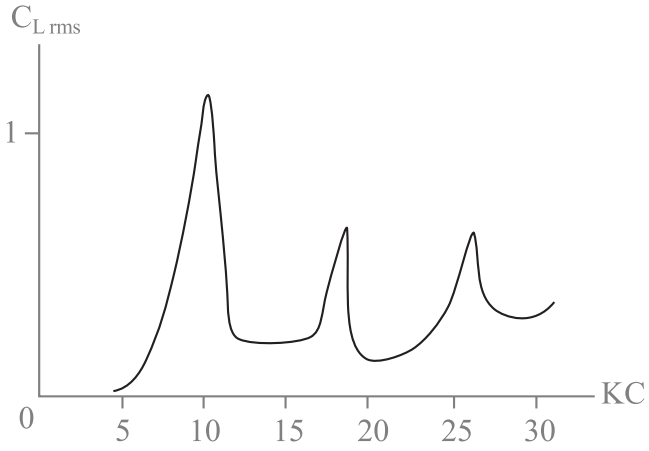

Figure 2.27: Sketch of the lift force coefficient (RMS) as function of KC number. Based on Williamson (1985).

The lift force (and also the drag force) has a sinusoidal behavior, so the force can be described using the maximum value or its corresponding RMS (root-mean-square) value:

$$F_{Lmax} = \frac{1}{2}\rho C_{Lmax} D U_m^2 \tag{2.84}$$

$$F_{Lrms} = \frac{1}{2}\rho C_{Lrms} D U_m^2 \tag{2.85}$$

in which U_m is the maximum velocity. Both lift coefficients are related by the equation:

$$C_{Lmax} = \sqrt{2} \cdot C_{Lrms} \tag{2.86}$$

2.5 Circular cylinders in Vortex-Induced Vibration

2.5.1 Cross-flow vortex-induced vibrations

As mentioned before, for Re > 40 a cylinder in a steady current will experience vortex shedding. Due to the vortex shedding, the lift and drag forces will oscillate. Now considering a flexibly-mounted cylinder, these forces may induce vibrations of the cylinder. The lift force causes cross-flow vibrations and the drag produces in-line vibrations (see Fig. 2.28).

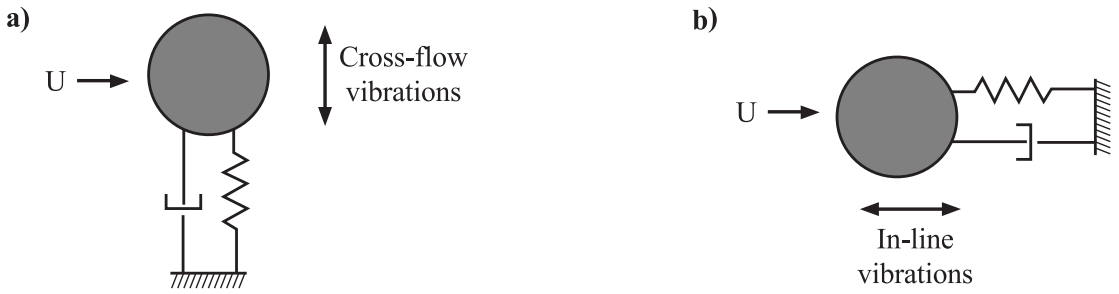

Figure 2.28: Different type of oscillations.

In 1968, Feng carried out an experiment where a circular cylinder with one degree of freedom was exposed to air flow. He noticed that at a certain air velocity, the cylinder experienced small vibrations. At that point the natural frequency and the vibration frequency of the system coincided. He also noted that before that particular point, the vortex-shedding frequency was identical to the stationary-cylinder frequency. However, after that point the vortex shedding frequency (f_v), the vibration frequency (f) and the natural frequency (f_n) of the system were the same despite the air velocity. This phenomenon was known as 'lock-in', 'synchronization', 'resonance', among others. As a note, recent studies have proven that this phenomenon is shown even when the frequencies are not equal, synchronization can be achieved at hundreds of times the natural frequency.

It can be concluded that at that specific point, the lift force and the movement of the cylinder occur at the same frequency and therefore the amplitude of the cylinder oscillations will be large (which in fact happens). When the air flow velocity overpassed some value, Feng noticed that the shedding frequency unlocked from the natural frequency and jumped to follow the stationary-cylinder frequency again; that means that the large amplitudes stopped.

For small vibrations in still fluid, $A/D < 0.8$, C_m is close to 1. When the cylinder is subject to a current the value of C_m will be different (see Fig. 2.29). In fact, the new

hydrodynamic mass coefficient will be denoted as C_{mc}, therefore the hydrodynamic mass will be defined as

$$m'_c = \rho C_{mc} \frac{\pi D^2}{4} \tag{2.87}$$

Figure 2.29: Hydrodynamic mass in still fluid and in current.

C_{mc} values have been measured by Sarpkaya (1978) for a circular cylinder subject to a steady current and oscillating in the cross-flow direction (forced oscillations), see Fig. 2.30.

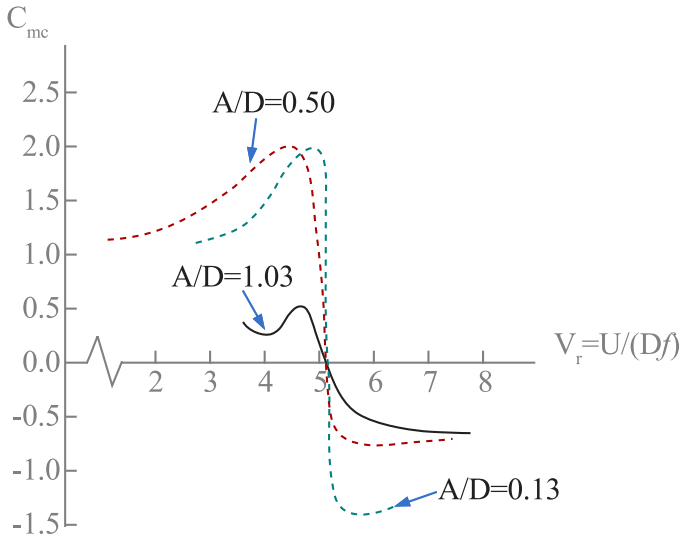

Figure 2.30: Sketch of the hydrodynamic mass coefficient for a circular cylinder vibrating in the cross-flow direction (forced oscillations) and subject to a current. V_r is the reduced velocity, where U is the velocity of the main flow, D is the diameter of the cylinder and f is the frequency of the forced vibrations. Based on Sarpkaya (1978).

2.5.2 The Griffin plot

In 1975 Griffin et. al. made the first compilation of results from different researches in VIV and compared them using the same parameter, the Skop-Griffin parameter S_G. In 1980, Griffin plotted a logarithmic axes representation to cluster the maximum amplitude of the cylinders in VIV, A^*_{max}, versus the parameter S_G (see Fig. 2.31). Even though this representation, known as the Griffin plot, is widely used in engineering to design structures, it is not well known under which circumstances it may or not apply. Actually, several validity issues under different circumstances are pointed out in Sarpkaya (1979, 1993).

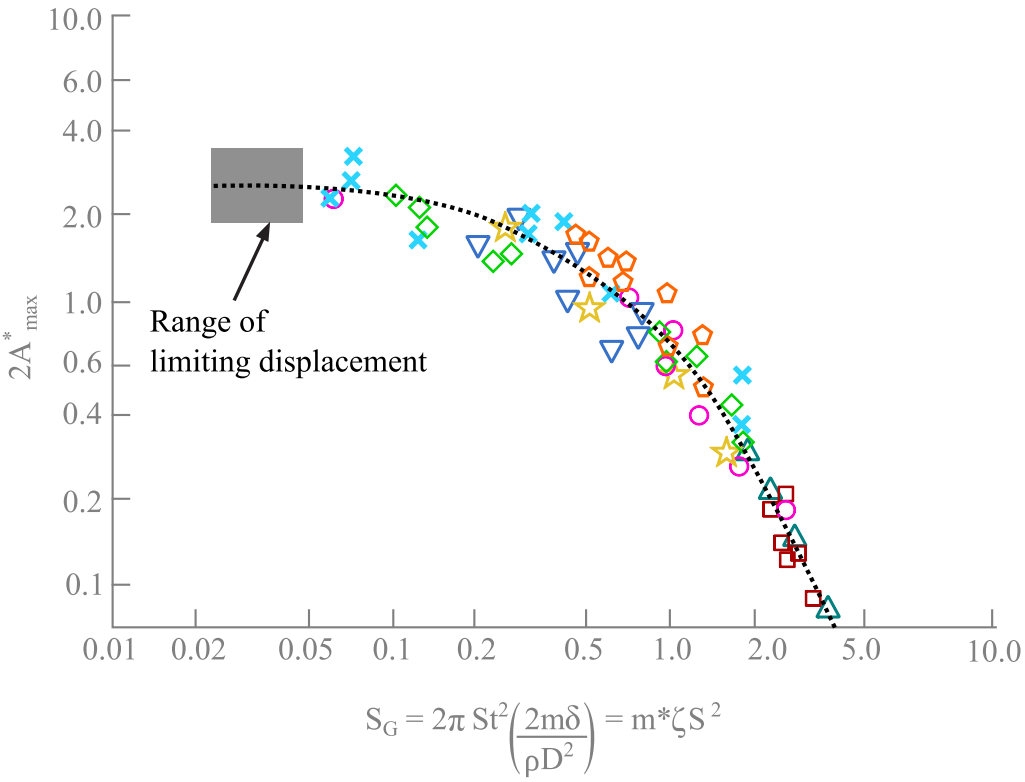

Figure 2.31: First extensive compilation of several studies, Griffin et al. (1975).

If similar data were plotted considering a linear representation in the y-axis, it can be observed a dispersion like in Fig. 2.32. This dispersion is "hidden" by the logarithmic axis. As stated by Williamson & Govardhan (2004), it seems no logic to collapse data from different systems undergoing VIV (elastic base, pivoted or cantilevered cylinders).

Considering data in Fig. 2.32 several authors, cited in Blevins (1990), have developed different empirical functions to relate A^*_{max} with S_G. However, none of them has been accepted by the scientific community.

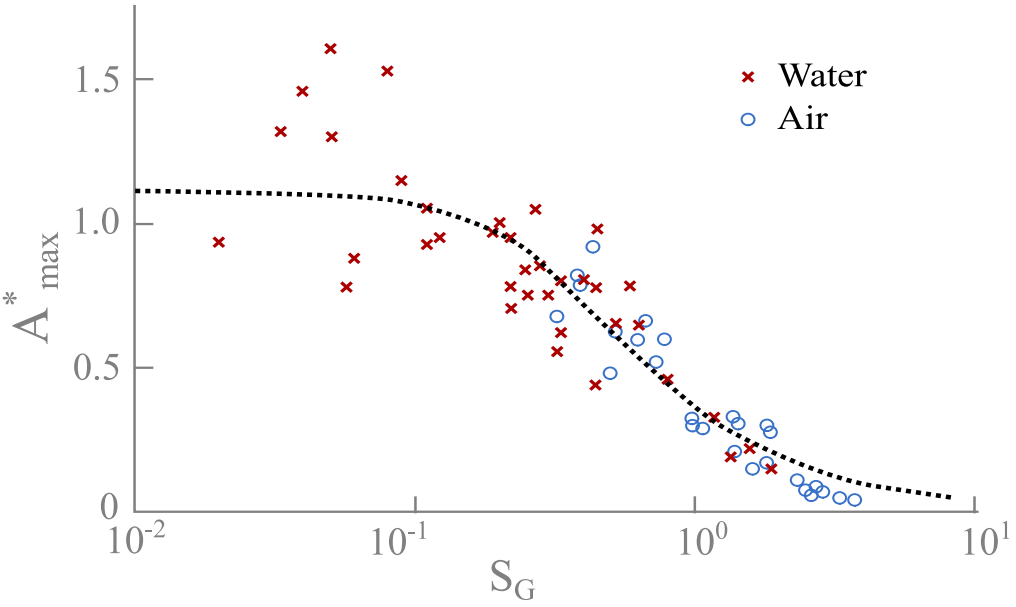

Figure 2.32: Updated Griffin plot using a linear representation in the y-axis, Williamson & Govardhan (2004).

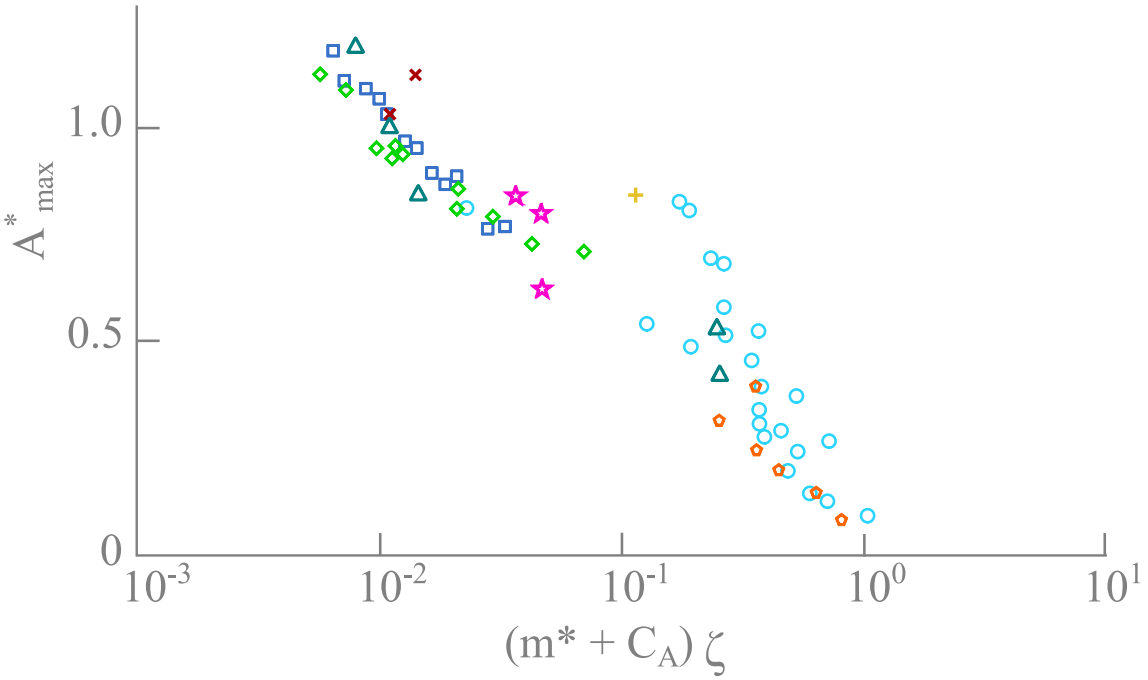

Figure 2.33: Modified Griffin plot, using the $(m^* + C_A)\,\zeta$ instead of the S_G parameter.

Williamson & Govardhan (2004) plotted A^*_{max} versus $(m^* + C_A)\,\zeta$ in another effort to find an easy-to-use simple relation, see Fig. 2.33. Although data seems to collapse better in a trend line, certain dispersion exists. This dispersion does not allow to use a general formula to describe the maximum amplitude behavior. Citing Williamson (2005) himself: "After 30 years the Griffin Plot is not yet fully defined!".

As mentioned above, there are still several unknowns as far as VIV is concerned. Most of the works in the literature have been developed using rigid cylinders elastically mounted, with forced vibrations, or with direct numerical simulations in 2-D. There are relatively few investigations that use flexible cylinders in cantilever with free vibrations, configuration proposed for this thesis.

2.5.3 The Williamson-Roshko map

In 1988, Williamson & Roshko published a vortex shedding modes map, see Fig. 2.34.

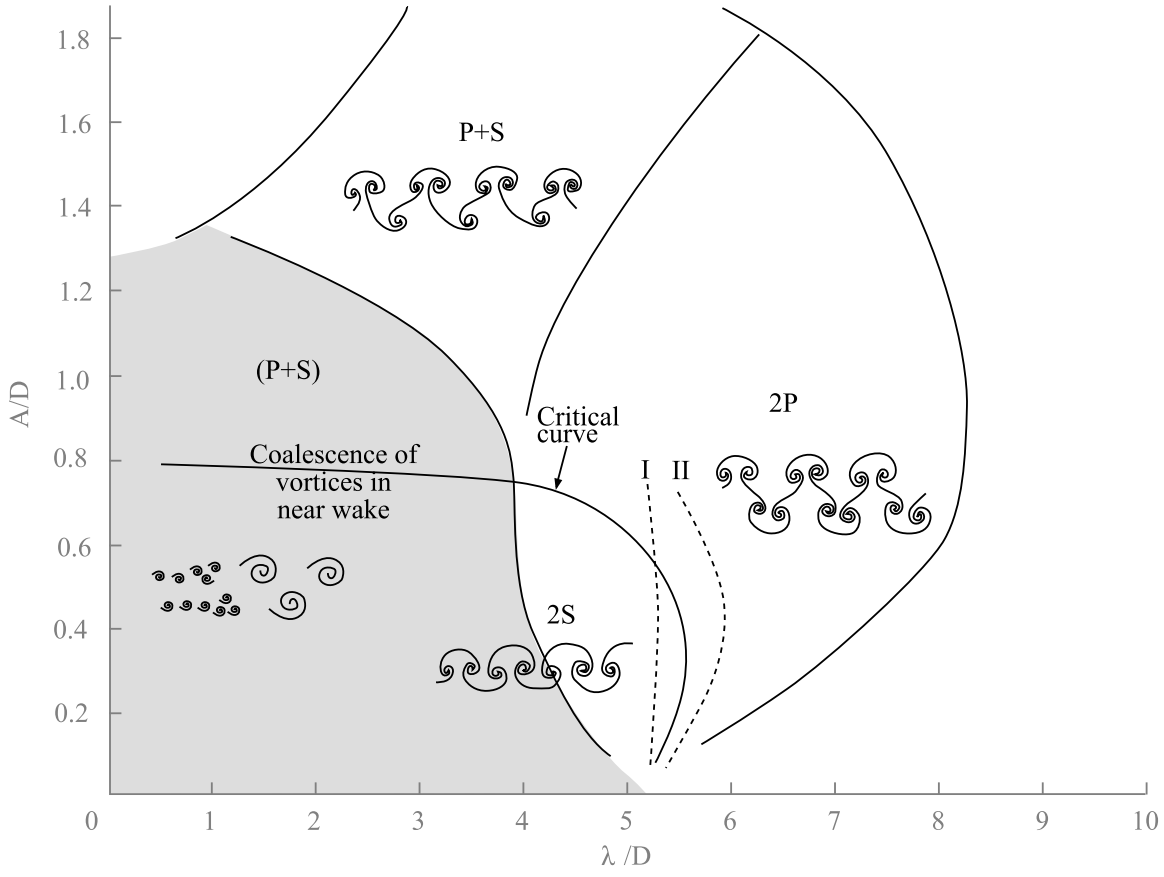

Figure 2.34: Williamson-Roshko map, Williamson & Roshko (1988).

This map was originally obtained with data of controlled forced vibrations. This means, instead of vortex induced vibrations (a cylinder moving by the effect of the formed vortex in the rear part) in these cylinders vortex induced by vibrations exists (the cylinder is forced to vibrate by external means and the vortex appear due to the cylinder movement). In many cases, these two types of vibrations are used as a VIV even though they have different configurations and properties. There are regions in which the comparison is valid and the results agree, however, regions where the comparison is far from accurate have also been found. It is still an open question of whether or not using this Williamson-Roshko map to predict the vortex shedding mode for different vibrating systems.

Williamson & Govardhan (2004) suggested to use the parameter U^* (normally used in free vibrations) to compare with A^*_{max} in the Williamson-Roshko map, Fig. 2.35. According to data obtained by them, the map shows a good correlation between the branches and the vortex shedding modes in each of them.

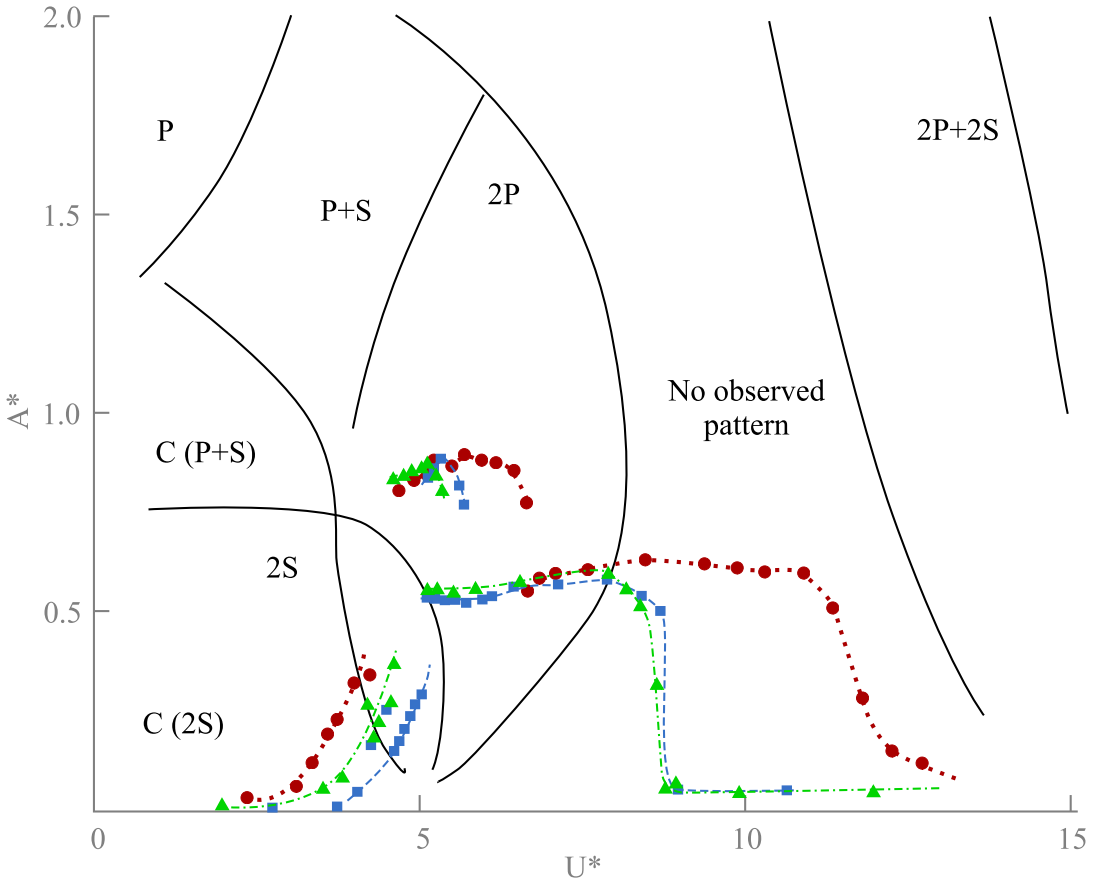

Figure 2.35: Updated Williamson-Roshko map, Williamson & Govardhan (2000).

Although data published by Williamson & Govardhan (2000, 2004) coincide with the Williamson-Roshko map, recent research suggests that it can not be used generally for all cylinder configurations. As shown in Fig. 2.35, the map suggests that the vortex shedding mode of the system is 2S in the initial branch, while the upper and lower branches correspond to a 2P. However, in the data obtained in Monreal (2015) for a flexible cylinder in cantilever, the vortex shedding pattern observed is the same in the whole synchronization zone, corresponding to a 2S.

3 Dynamic and hydrodynamic analysis of circular cylinder undergoing vortex induced vibrations

In this chapter, the experimental setup is explained. The dynamic response in free vibrations is processed in order to get the parameters of each cylinder. These parameters: m (total mass of the system), c (structural damping), and k (spring constant) are useful to calculate forces acting on the cylinder along with the synchronization regime. The dynamic response in the entire lock-in region is studied and the maximum amplitude and frequency at different Re numbers are given. At the end of the chapter, also, the hydrodynamic response is shown.

3.1 Experimental setup

In order to study the lock-in region, and therefore the VIV phenomenon, cantilevered uniform flexible circular cylinders were used. Fig. 3.1 illustrates the schematic diagram of the experimental apparatus. It consists of a 19 mm thick solid aluminum plate, whose dimensions are shown in the figure. To avoid flow perturbations, one side was beveled at 30 degrees.

External lighting was used to assure that the high-speed video camera record the tip of the cylinder. The lighting consisted of two 3-watt and 250-lumen LED lamps, facing each other, both pointing to the tip of the cylinder. The high-speed video camera was an "Edgertronic ®". It is designed with a specialized 1280 × 1024 CMOS Image Sensor, ultra-high-speed electronics, memory, and image processing electronics. This camera allows up to 17,791 frames per second at 192 × 96 pixels resolution.

A schematic diagram of the entire experimental setup is presented in Fig. 3.2. The experimental apparatus was placed in a water tunnel, which has a test section of 0.381m × 0.508m × 1.5 m. The operating velocity range varies between 0.01 and 0.3 m/s. Levels of turbulence in the test section are less than 1% RMS. The aluminum

plate was placed ensuring the in-line flow direction was in the x axis and the cross-flow direction corresponded to the y axis.

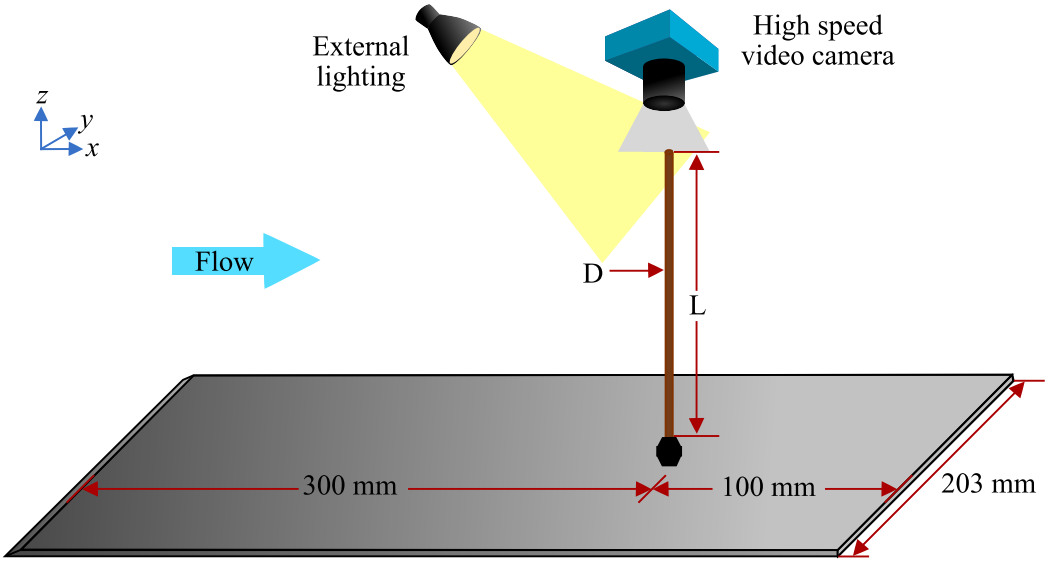

Figure 3.1: Experimental model scheme.

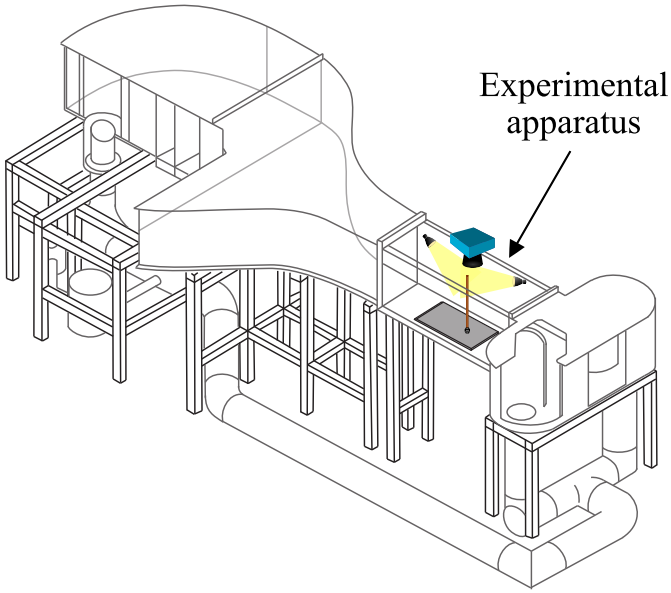

Figure 3.2: Experimental setup: schematic diagram of the water tunnel and the apparatus.

3.2 Test cylinders

In this thesis, different cantilevered uniform flexible circular cylinders were tested. To cover as much Re numbers as possible in the lock-in region several different materials, diameters and lengths were chosen for the cylinders. Geometrical ranges corresponding to diameter and length are 1.56 mm $\leqslant$ D $\leqslant$ 3.19 mm and 30 cm $\leqslant$ L $\leqslant$ 40 cm, respectively. Materials tested are aluminum, bronze, copper and stainless steel. The different combinations of length, diameter, and material are presented in Tab. 3.1. The mass ratio,m^*, is taken for simplicity and is the ratio between the cylinder density and the working fluid density (in this case water).

Each of these cylinders was placed in the experimental apparatus to run several tests. To measure the dynamic response of the cylinder, the Particle Tracking Velocimetry (PTV) technique was implemented. The PTV technique consists of finding a specific figure, in this case the tip of the cylinder represented in Fig. 3.3, and track its position along each frame of the video. A code in Matlab ® specifically developed for this study computed the (x, y) location coordinates of the tip of the cylinder by using circular Hough transform. This allows to get the path of the cylinder over time in both axes separately.

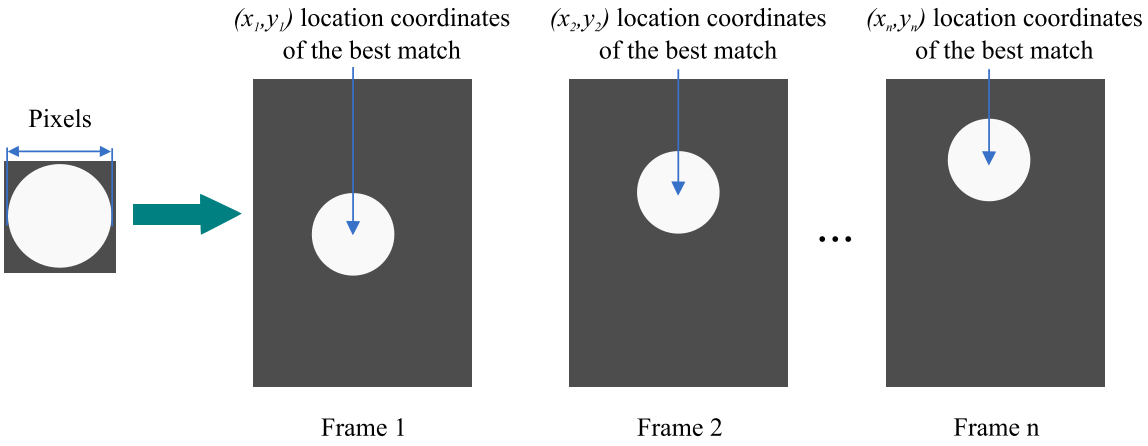

Figure 3.3: PTV technique in the tip of the cylinder.

The path can be processed by the discrete Fourier transform. The Fourier analysis converts time into frequency by decomposing a sequence of values into components of different frequencies. In this way, the natural frequency of the system can be determined. In Tab. 3.2 the different paths and their respective frequency histograms in air are shown. Tab. 3.3 presents the corresponding results in water.

Material	L [m]	D [mm]	$m^* = \rho/\rho_f$
Aluminum	0.30	1.57	2.66
Aluminum	0.35	1.57	2.66
Aluminum	0.35	2.39	2.66
Aluminum	0.35	3.18	2.66
Aluminum	0.40	1.57	2.66
Aluminum	0.40	2.38	2.66
Aluminum	0.40	3.18	2.66
Bronze	0.30	1.56	8.49
Bronze	0.30	2.30	8.49
Bronze	0.35	1.58	8.49
Bronze	0.35	2.33	8.49
Bronze	0.35	3.16	8.49
Bronze	0.40	1.58	8.49
Bronze	0.40	2.33	8.49
Bronze	0.40	3.15	8.49
Copper	0.30	1.58	7.89
Copper	0.30	2.36	7.89
Copper	0.35	1.58	7.89
Copper	0.35	2.38	7.89
Copper	0.35	3.20	7.89
Copper	0.40	1.58	7.89
Copper	0.40	2.38	7.89
Copper	0.40	3.20	7.89
Stainless Steel	0.30	1.57	7.91
Stainless Steel	0.30	2.34	7.91
Stainless Steel	0.35	1.57	7.91
Stainless Steel	0.35	2.34	7.91
Stainless Steel	0.35	3.19	7.91
Stainless Steel	0.40	1.57	7.91
Stainless Steel	0.40	2.34	7.91
Stainless Steel	0.40	3.19	7.91

Table 3.1: Different combinations of length, diameter and mass ratio (m^*) of the cylinders under study.

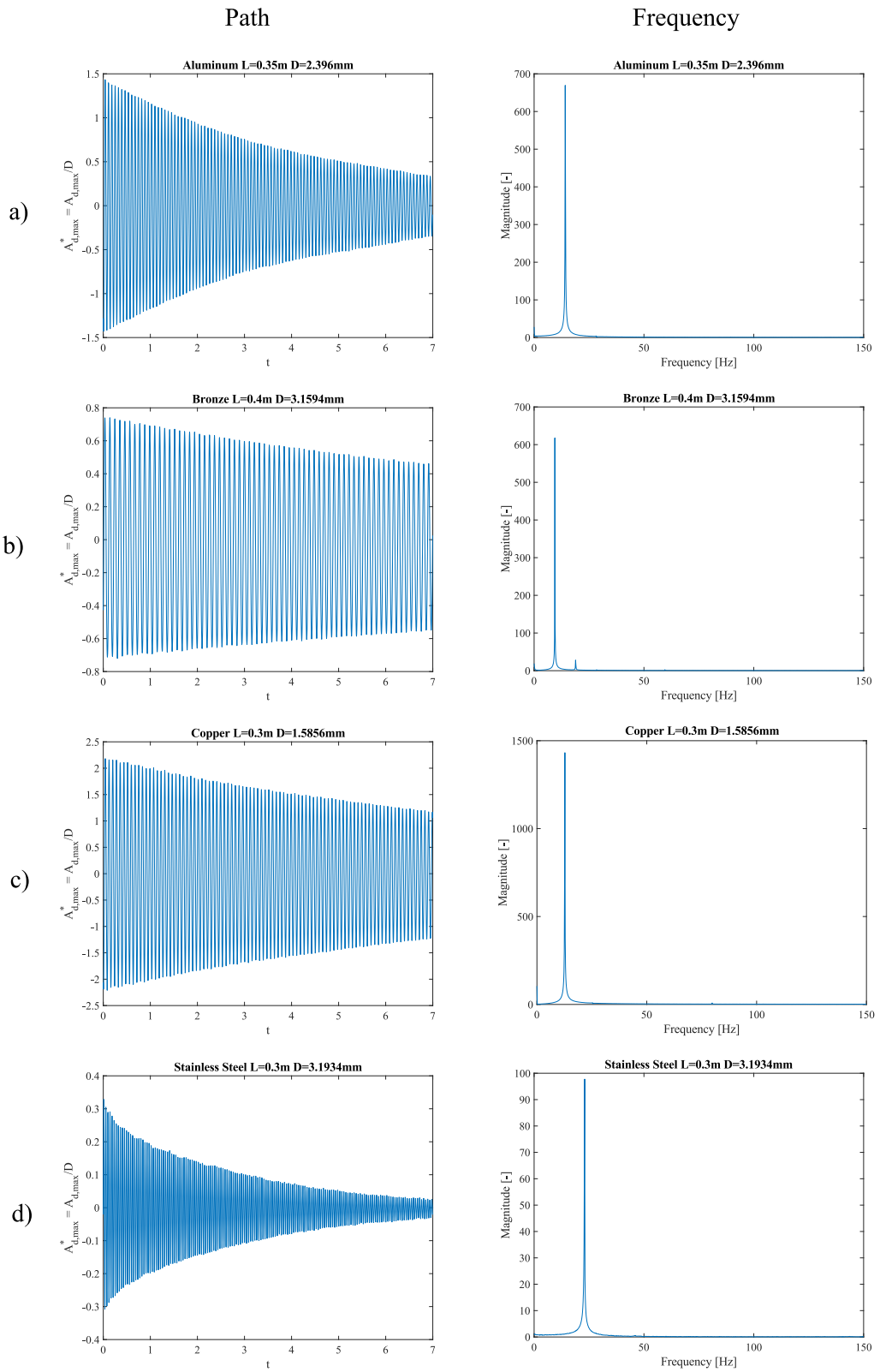

Table 3.2: Impulse response of the different materials in still air. a) Aluminum, b) Bronze, c) Copper, and d) Stainless steel.

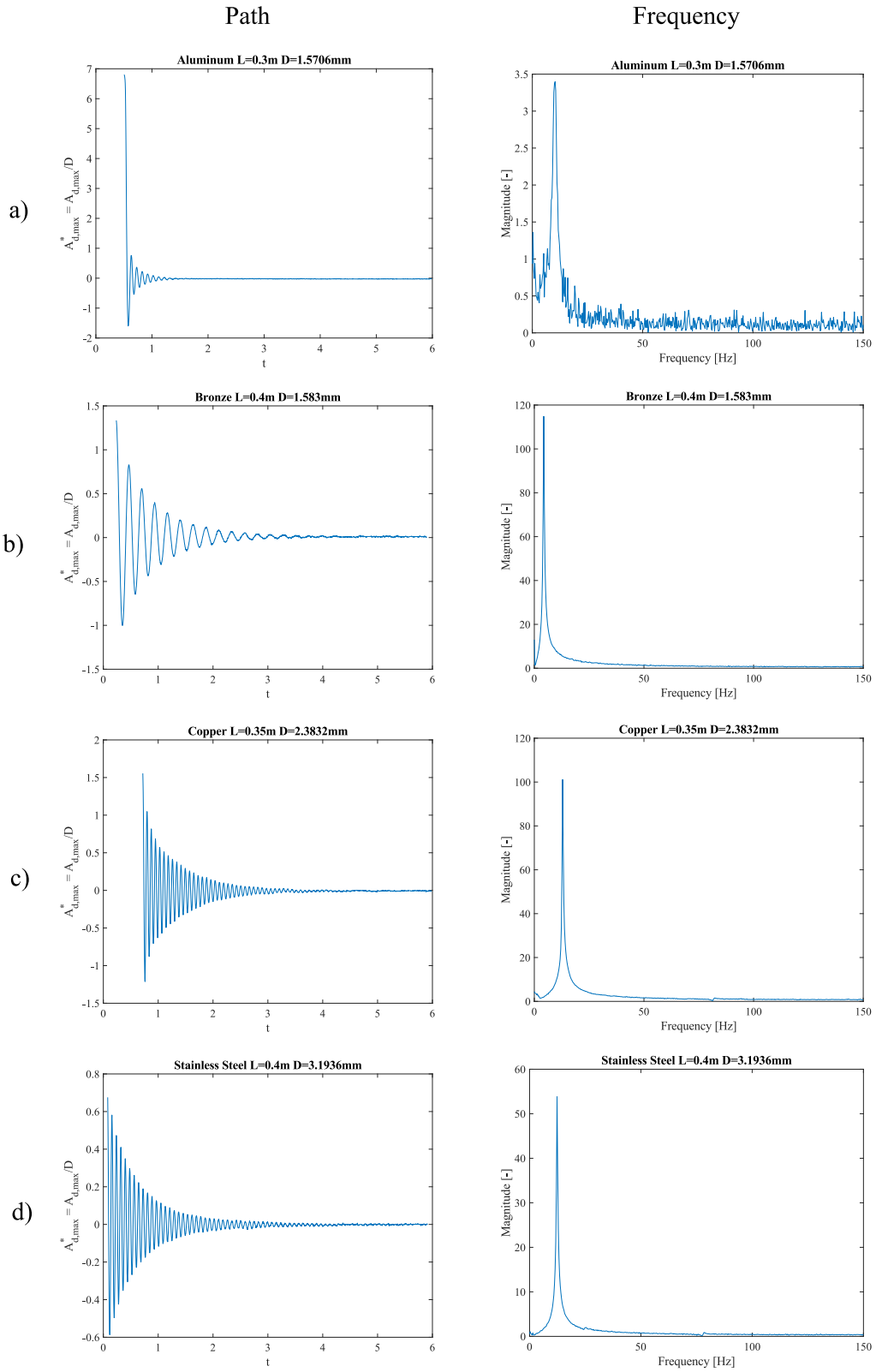

Table 3.3: Impulse response of the different materials in still water. a) Aluminum, b) Bronze, c) Copper, and d) Stainless steel.

3.3 Obtaining parameters

3.3.1 Stiffness of the cylinder (k)

For each cylinder, the specific mass, spring and damper coefficients need to be determined. The first step was to find the stiffness (k). To accomplish this, a picture of the top view of the cylinder in the equilibrium position was taken. Then using a set of weights and pulleys, a known perpendicular force was applied (Fig. 3.4), and a picture with the same camera position was taken. This procedure was repeated with several weights to obtain different measurements, so they can be compared. With the acquired photos, the displacement of the center of the cylinder relative to the equilibrium point was calculated (Fig. 3.5). Finally Eq. 3.1 was used:

$$k = \frac{F}{x} \tag{3.1}$$

where F represents the known force applied to the cylinder and x is the displacement of the center of the cylinder.

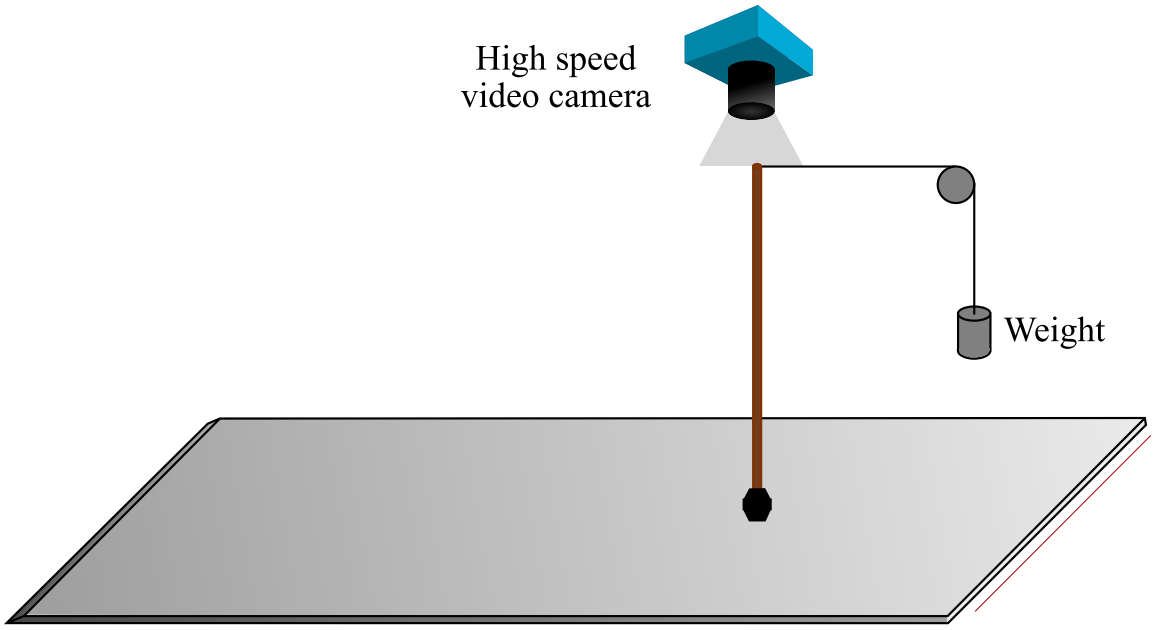

Figure 3.4: Schematic diagram: experimental procedure for the estimation of stiffness of the cylinder.

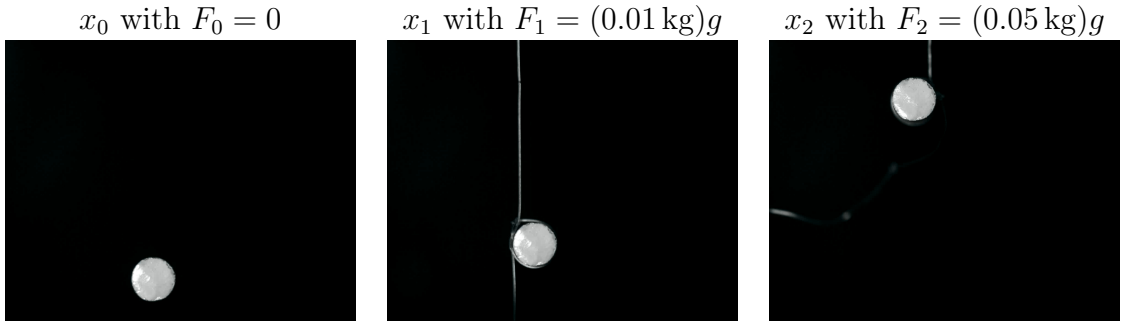

Figure 3.5: Actual photos of the stiffness experiment. Where g is the gravity. a) equilibrium position, b) displacement x_1 with a force applied F_1, c) displacement x_2 with a force applied F_2.

In Fig. 3.6, the quantitative results of the test are shown.To see the experimental results of the estimation of stiffness of each cylinder, refer to sec. 5.2.

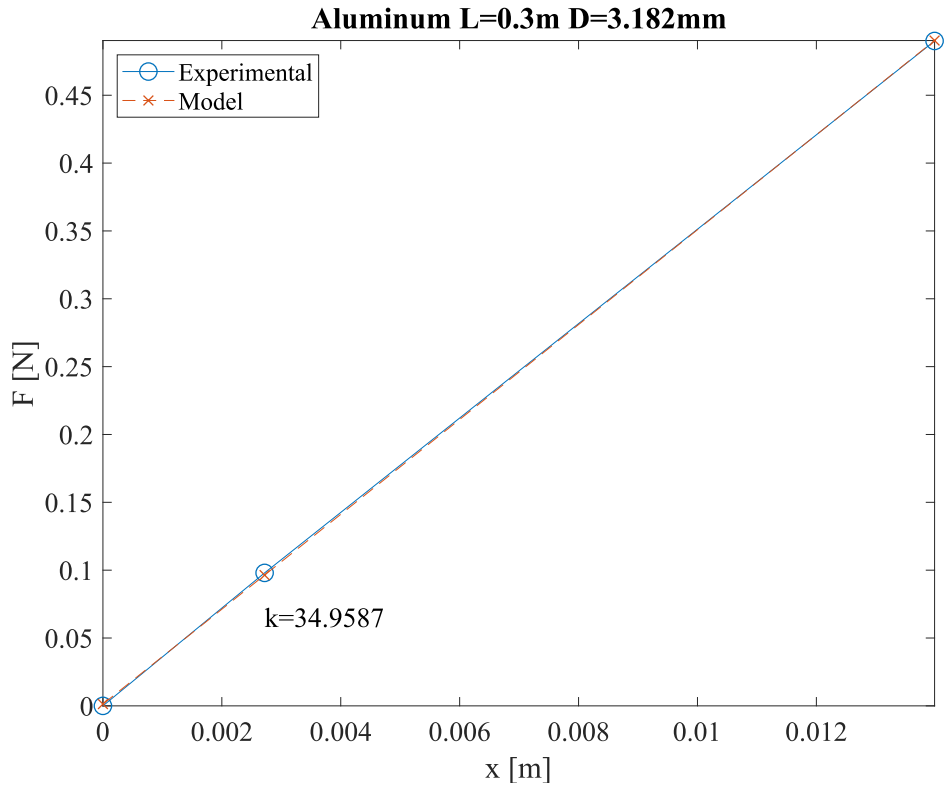

Figure 3.6: Plotted results of the stiffness experiment for one cylinder.

3.3.2 Viscous damping (ζ)

The next step was to find the damping of the cylinder. To achieve this, the experimental apparatus was subjected to a small impulse perturbation and the dynamic response was recorded (free vibration). These images were processed using the PTV technique, see Fig. 3.7. The recorded answer was adjusted to the mathematical model:

$$y\left(t\right) = A_0 \exp\left(-\zeta\omega_d t\right) \sin\left(\omega_d t + \varphi\right) \tag{3.2}$$

where A_0 is the maximum amplitude, ω_d is the damped angular frequency, and φ is the phase that determines the behavior needed to match the initial conditions. Here the damping ratio, ζ, consists of the structural damping , ζ_s, and the damping due to the surrounding fluid, ζ_f. For detailed information about the solutions to vibration equation, and structural and fluid damping see sec. 2.5.

$$\zeta = \zeta_s + \zeta_f = \frac{\delta}{\sqrt{\delta^2 + (2\pi)^2}} \tag{3.3}$$

Free vibration with air as surrounding fluid In this case, the assumption that the response in air is practically equal to the response in vacuum was made. This means that the damping ratio corresponds only to the structure damping, namely $\zeta = \zeta_s$. Using the response in air to fit Eq. 3.2, the coefficients ζ and ω_d were known. And with Eq. 3.4 the value of ω_n was calculated.

$$\omega_d = \omega_n \sqrt{\frac{1}{1+\zeta^2}} \tag{3.4}$$

Knowing ω_n and using Eq. 3.5, the value of m was known. Here m represents the equivalent mass coefficient needed for the discretized model, see Fig. 3.8a.

$$\omega_n = \sqrt{\frac{k}{m}} \tag{3.5}$$

Strictly speaking, Eq. 3.5 should have not only m but $m + m'$ in the right hand of the equation. However, the assumption that the response in air is practically equal to the response in vacuum allows to neglect the hydrodynamic mass, m' (see sec. 2.4.3.1 for detailed information about m').

Finally, the only unknown parameter was the viscous damping coefficient, c. Using Eq. 3.6, this last parameter could be calculated.

$$\omega_d = \sqrt{\frac{k}{m} - \left(\frac{c}{2m}\right)^2} \tag{3.6}$$

It is important to highlight that all three parameters (m, c and k) calculated here are assumed to be calculated in vacuum, and their values will be used on the discretized model.

Free vibration with water as surrounding fluid As can be seen from Fig. 3.7, the response in water is different from the response in air. In water, the frequency is lower and the damping of oscillations is bigger. This is because here the damping ratio, ζ, corresponds to both structural and fluid damping, namely $\zeta = \zeta_s + \zeta_f$. The viscosity of water is bigger than air viscosity, and this leads to an increased energy dissipation. In this case the value of ζ_f is so big that it dominates the total damping, ζ.

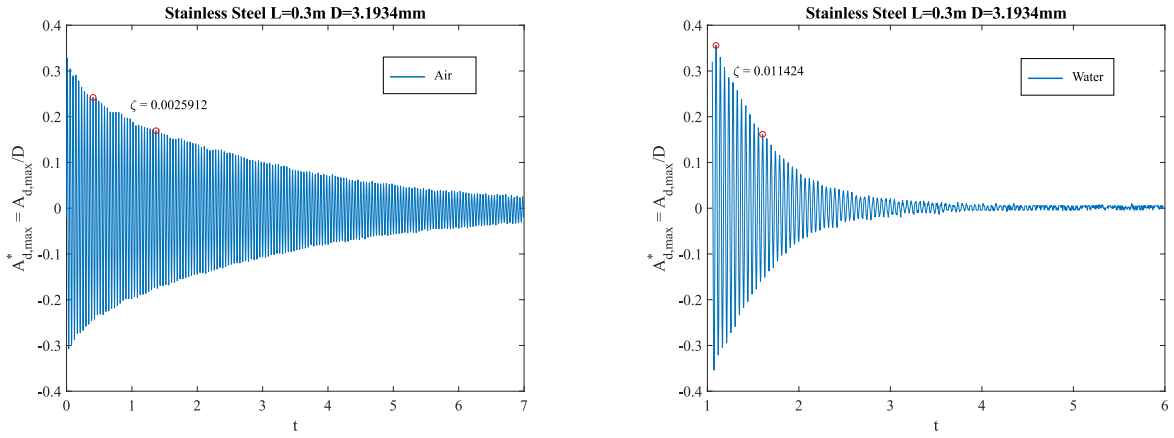

Figure 3.7: Response of a stainless steel cylinder in free vibration. In air at the left and in water at the right.

The same method to know the parameters used in free vibration with air as surrounding fluid was applied. Using Eq. 3.2 to fit the response in water, the coefficients ζ and ω_d were known; and using Eq. 3.4 the value of ω_n was calculated.

Then in order to calculate the mass coefficient, Eq. 3.5 becomes

$$\omega_n = \sqrt{\frac{k}{m + m'}} \tag{3.7}$$

Here the mass involves not only the mass due to the structure, m, but also the hydrodynamic mass, m', which is the mass of fluid accompanying the displacement of the cylinder due to the inherent viscosity of the fluid (see Fig. 3.8 b). From the free vibration with water as surrounding fluid, the value of m is known and m' can be calculated.

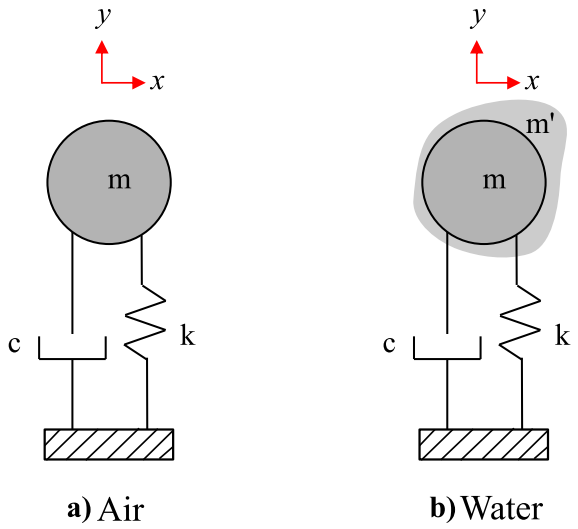

Figure 3.8: Discretized model. a) In air the equations only include the mass due to the structure, b) in water the equations include the mass due to the structure and the hydrodynamic mass.

In sec. 5.2 the path and frequency for each cylinder in air is shown, in chapter 5.2 there are the same plots but in water. In the path plot, two red circles mark the values used to determine ζ by using the Eq. 2.28, where the logarithmic decrement is calculated by $\delta = 1/i \ln(y_n/y_{n+i})$ and i represents the number of cycles or periods from y_n to y_{n+i}. This is mentioned in sec. 2.1.4.3.

3.3.3 Mass (m)

Finally, the mass is obtained by weighing the metallic cylinder in a scale. It is important to mention that the parameters calculated in air are considered as vacuum due to its small ζ_f.

3.4 Dynamic response

Once the parameters are known, the next test is to find the lock-in region and record the dynamic response of the tip. For tracking the tip, the experimental apparatus with the cylinder was placed on the tunnel test section, with the in-line direction (axis x) and cross-flow direction (axis y) fixed, as shown in Fig. 3.1 and Fig. 3.2. The flow starts at a very low Reynolds numbers, Re, until the cylinder starts to oscillate, then the velocity is increased and therefore the Re. The experiments cover the entire synchronization regime, with Re ranging from 75 to 1050. A variable $\triangle$Re was used depending on the cylinder, the Re numbers, among others.

In this test, the most significant result is the maximum amplitude in the cross-flow direction against Re. This is illustrated in Fig. 3.9. It is important to note that in this work the amplitude of the in-line oscillations differs by one order of magnitude with the amplitude of the cross-flow oscillation, which is in accordance with Jauvtis (2003). Therefore, the results obtained only consider the cross-flow direction.

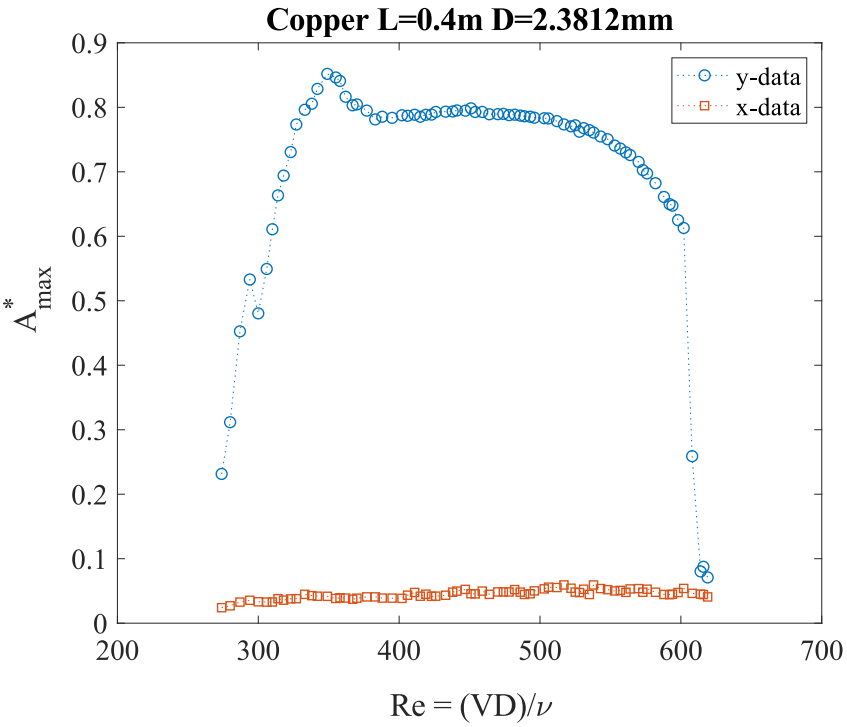

Figure 3.9: Maximum amplitude in the transverse direction vs Reynolds number.

Fig. 3.10 represents an example of the behavior of the tip of the cylinder in the three different points of the synchronization regime.

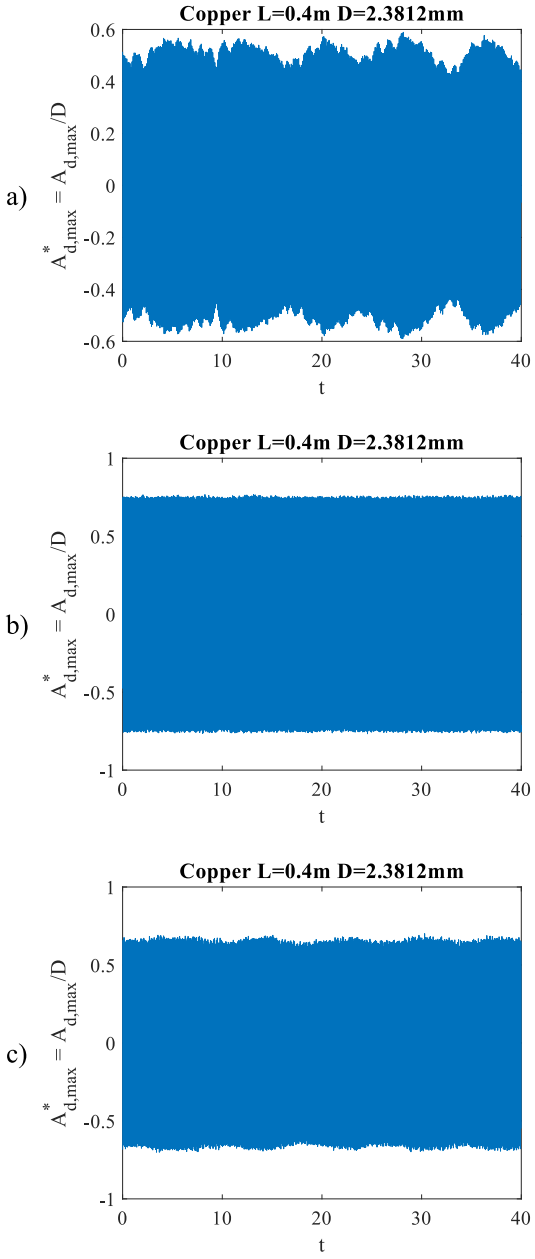

Figure 3.10: Path of the tip of the cylinder at different Re. a) Re = 310, b) Re = 438 and c) Re = 564.

The results proved that the dynamic of the cylinder is consistent with that described in several scientific articles presented by Oviedo et al. (2014) and Khalak & Williamson (1999). In Fig. 3.11, the left column depicts the orbits of the free-end of the cylinder. In the right column the cylinder displacements over time are shown in both axes, blue

line for the y axis and red line for the x axis. Both columns show the three same points shown above.

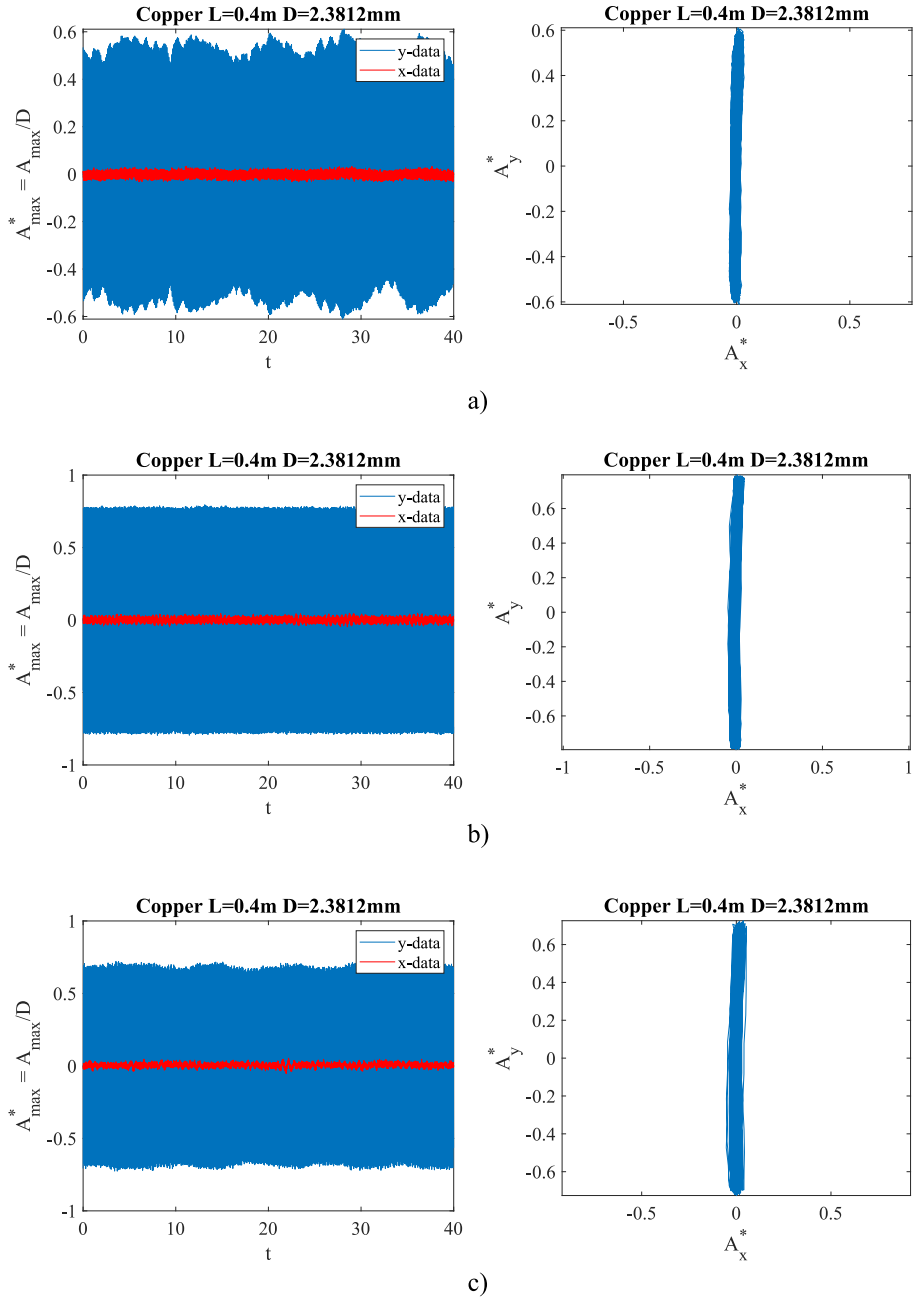

Figure 3.11: Orbits of the free-end of the cylinder and cylinder displacements over time in both axes. Both columns show three different points of the lock-in region: a) Re = 310, b) Re = 438 and c) Re = 564.

3.4.1 Standard Error of the Mean and Residual Standard Deviation

For the experimental campaign, several repetitions were made according to the physical or geometric parameter. For the case of mass (m) and diameter (D), three repetitions of each measurement were made. For damping ratio (ζ), frequency (f_{water}, f_{vacuum}) and spring coefficient (k), six experiments were carried out. Finally, each experimental point in the lock-in region was repeated five times. This means that five videos, eight seconds each, were taken. Fig. 3.12 illustrates the amplitude vs time corresponding to 5 repetitions for a specific point.

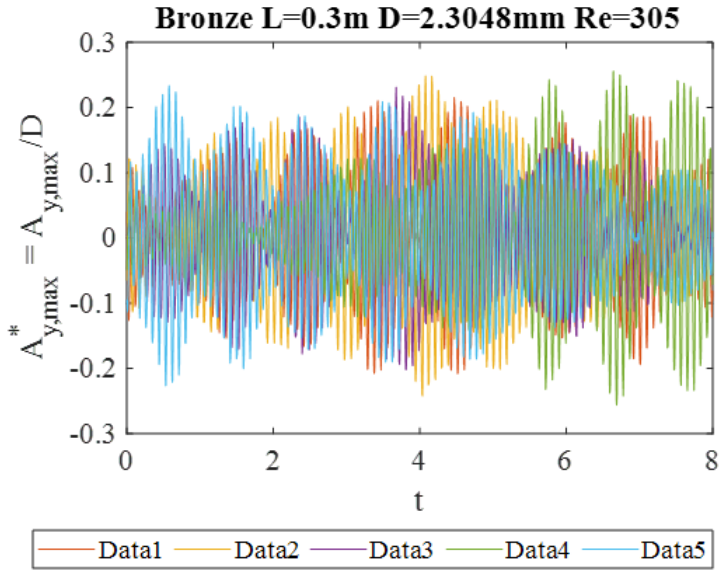

Figure 3.12: Amplitude vs time corresponding to 5 repetitions for a specific point: Bronze, L=0.3m, D=2.4 mm and Re=305.

To obtain the error bars, the standard error of the mean (SEM) was used. Considering all data available to calculate the SEM, the error for this example is 8.1064e-04. On the other hand, if only the five maxima (one per each replica) values are used, the SEM is 0.0071. In both cases, it is practically negligible.

Based on these results, the error bars are calculated using the residual standard deviation (RSD), which uses the difference between predicted and actual values. The predicted values are obtained from:

$$Y_{est} = A^*_{y,max} = A \sin(\omega t) \tag{3.8}$$

To calculate the RSD the formula below is used:

$$S_{res} = \sqrt{\frac{\sum (Y_i - Y_{est})^2}{(n-1)}} \tag{3.9}$$

Where S_{res} is the residual standard deviation, Y_i is the experimental value, Y_{est} is the estimated value and n is the amount of data. Fig. 3.13 presents the experimental and estimated data corresponding to the case represented in Fig. 3.12.

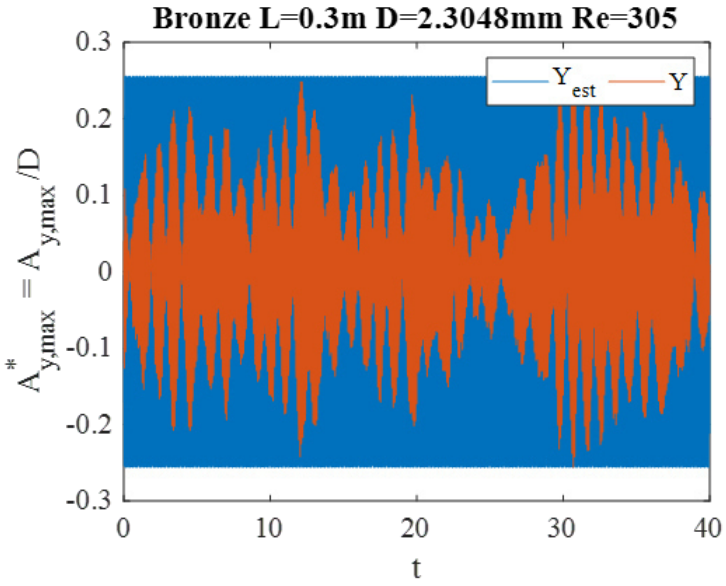

Figure 3.13: Example of estimated and experimental values for a specific point: Bronze, L=0.3m D=2.3948 mm and Re=305.

Using this method, the standard error of the residual is calculated by dividing the S_{res} by the square root of n. The resulting value is 0.0017, also negligible. The described procedure was performed for each experimental point. The calculations are not included in this thesis because only group one presents significant, but still small $<5\%$, error bars.

3.5 Hydrodynamic response

3.5.1 Particle Image Velocimetry

To study the hydrodynamics around the cylinders, the Particle Image Velocimetry (PIV) technique was used. The apparatus used to perform the experiments is shown in Fig. 3.14. For this technique the fluid was seeded with hydrogen bubbles. In this case, the bubbles were produced by electrolysis. The size of the bubbles is controlled principally by modifying the diameter of the cathode and the voltage input. One of the greatest advantages of this technique is that bubbles allow to keep the tunnel water clean, unlike other methods as using glass nanoparticles.

When the fluid is seeded correctly, a spatial plane is illuminated with external LED lighting from the bottom. This allows the bubbles to shine and be visible for the camera. An example of the frame captured during these tests is in Fig. 3.15.

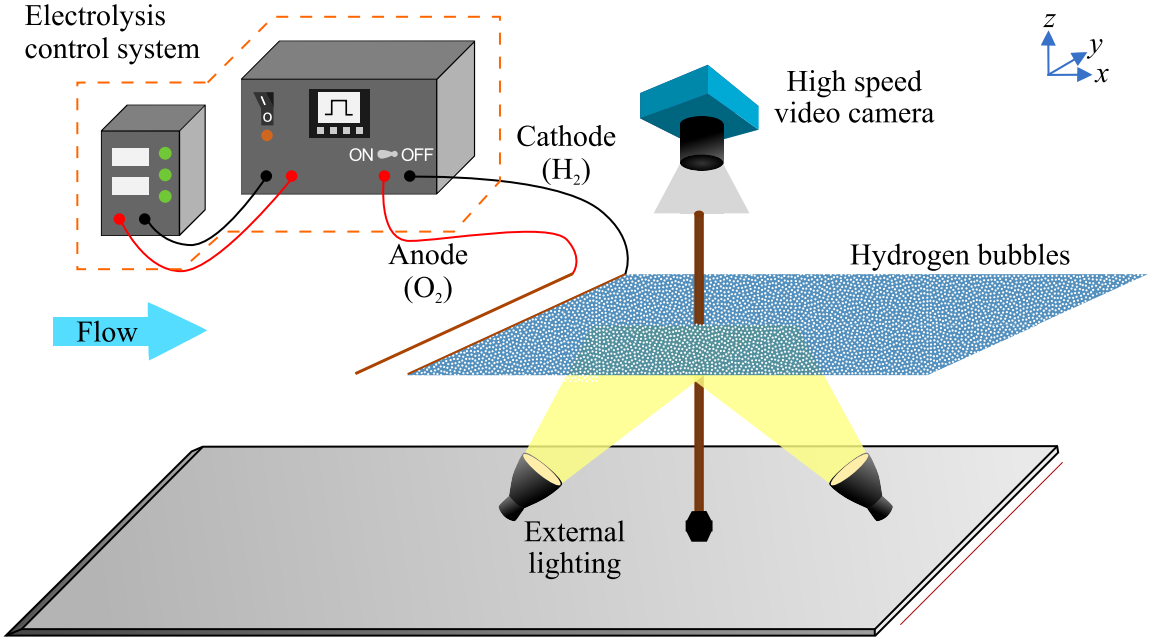

Figure 3.14: Experimental model with an electrolysis control system.

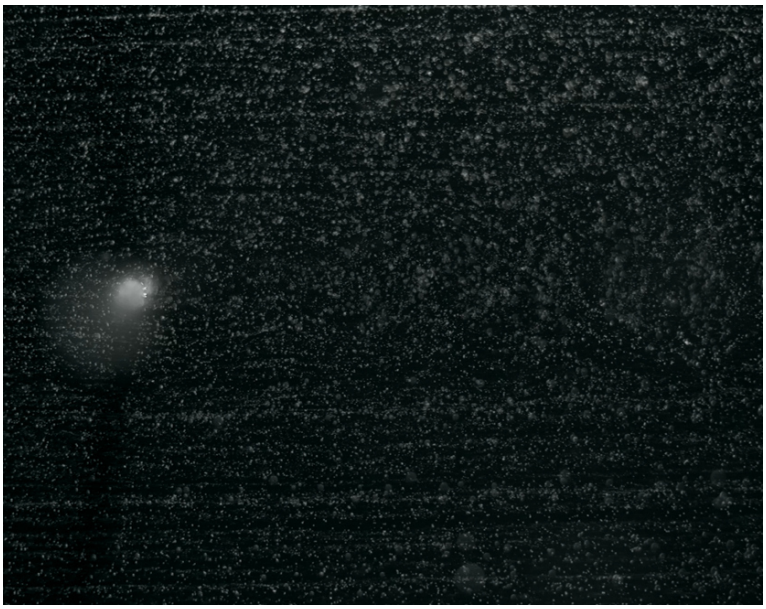

Figure 3.15: Actual frame of the hydrodynamic test. .

The high-speed video camera used to record the cylinder was an "Edgertronic ®". The motion of the seeding bubbles was used to calculate speed and direction (the velocity field) of the flow being studied. In Fig. 3.16 a simplified graphical explanation of this technique is shown. To perform the PIV, the images were processed using the "PIVlab" software. Detailed information about how pre-processing, correlation and post-processing techniques affect the accuracy and the quality of PIV results are explained in Thielicke 2014a and Thielicke 2014b.

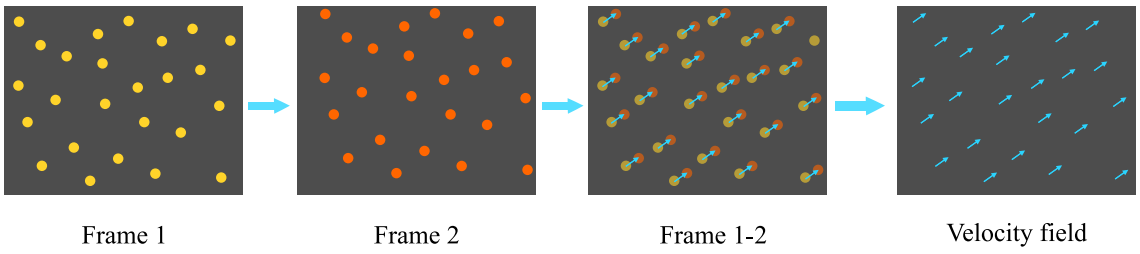

Figure 3.16: Simplified model of PIV technique.

3.5.2 Vortex shedding pattern

The hydrodynamic response is expected to be the same in the three branches. In this case, it can be observed that the hydrodynamic is 2S mode (two-pair of single vortex),

as can be observed in Fig. 3.17. This means two pairs of vortices are shed per period, one vortex spins clockwise and the other spins counter-clockwise.

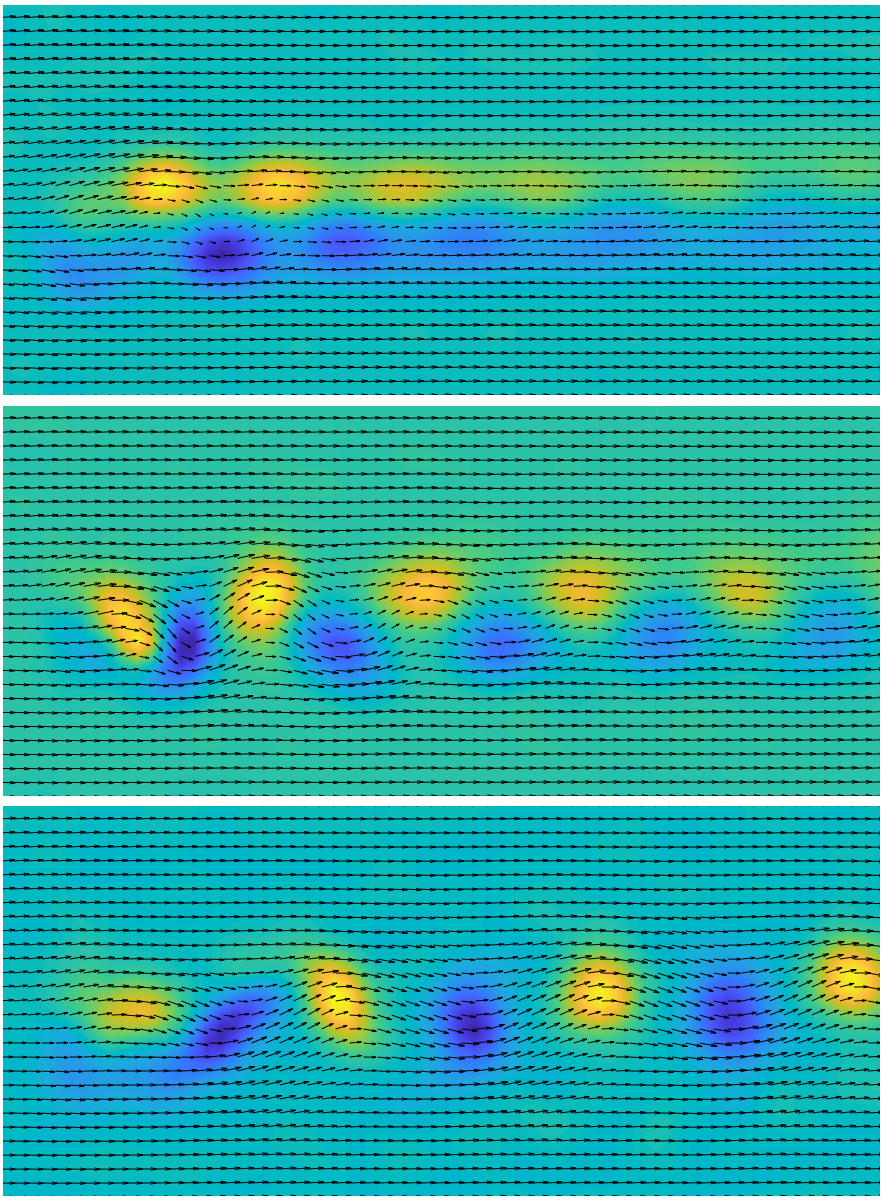

Figure 3.17: Vorticity in the synchronization regime. All the images correspond to the aluminum 40 cm length and 1.57 mm diameter cylinder. a) Re = 95, b) Re = 119 and c) Re = 167.

It is important to notice that in all the experiments developed in this thesis, a one millimeter Mitutoyo® calibration pattern was used. This pattern allows to calculate

the uncertainty of the experiments, as well as having traceability and accurate values in the measurements and calculations. In Fig. 3.18 a picture of the calibration pattern and a 2.3 mm cylinder is shown, due to illumination only half of the cylinder is visible on the right side of the image.

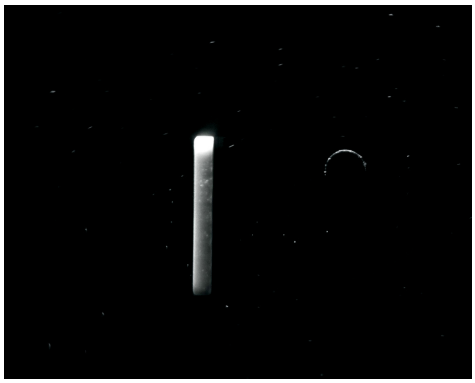

Figure 3.18: 1mm Mitutoyo® calibration pattern. .

4 Results and discussion of amplitude response in the Griffin plot and its comparison with classification parameters

The first part of this chapter shows the existence of four different groups, corresponding to different behaviors of the maximum amplitude as a function of Re. Atypical branches are distinguished and explained in detail. An analysis was developed in order to classify this branches with a characteristic parameter, resulting in the slope of the reduced velocity, V, and Re numbers the best arrangement parameter.

4.1 Classification of different groups

This section presents the experimental results obtained through the synchronization regime for all the cylinders tested. The maximum amplitude as a function of Re is illustrated in Fig. 4.1. Based on the different behavior patterns, four different groups are recognized and named groups 1 to 4. Fig. 4.1b is presented to point out the difference in magnitude order between the in-line and cross-flow direction. It is important to highlight that in this work the amplitude of the in-line oscillations differs by one order of magnitude with the amplitude of the cross-flow oscillation, which agrees with (Jauvtis and Williamson, 2003). Therefore, the results obtained only consider the cross-flow direction.

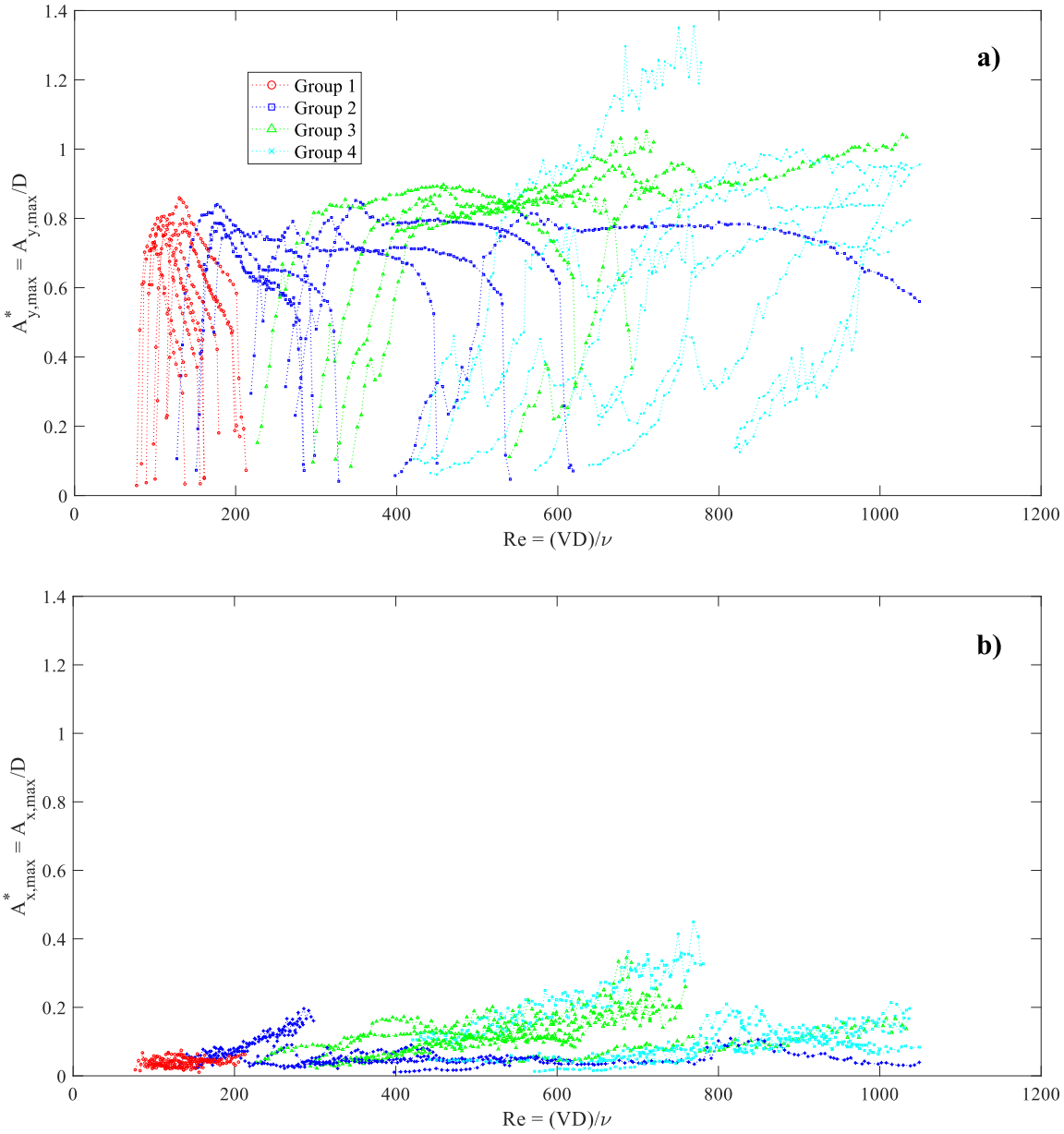

Figure 4.1: Maximum amplitude vs Re for all the cylinders tested. a) cross-flow direction, and b) in-line direction.

Results corresponding to the first group can be observed separately in Fig. 4.2. They correspond to slender cylinders with 1.58±0.05 mm diameter, for the different lengths and materials. Two different zones or branches characterize this group.

- The initial branch includes the first oscillations of the cylinder until it reaches its maximum amplitude. A rapid increase in the amplitude is observed.

- The lower branch includes the points from the maximum amplitude until the cylinder stops oscillating: where the amplitude decreases constantly (the Re vs A_y slope is constant).

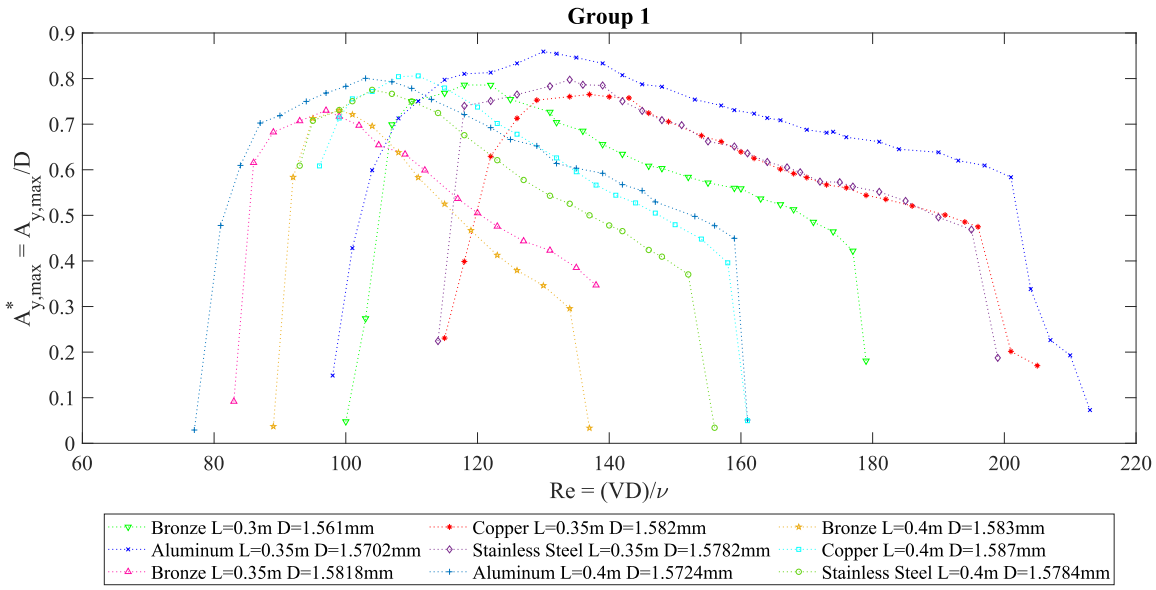

Figure 4.2: Maximum amplitude against Re for different materials and lengths corresponding to group 1. Results for $D = 1.58 \pm 0.05$ mm.

The second group, Fig. 4.3, comprises all ranges of different diameters and lengths. This group is the most common amplitude pattern seen in the literature, in concordance with (Cicolin and Assi, 2017; Fujarra et al., 2001; Oviedo-Tolentino et al., 2014; Wang et al., 2017), to name some. Govardhan and Williamson (2000) defines this group for cylinders with low mass-damping ratios, showing three typical branches: initial, upper and lower. According to Govardhan and Williamson (2000), the frequency of oscillation of the cylinder passes through the natural frequency of the cylinder in water in the transition from initial to upper branch. In like manner, the frequency of oscillation of the cylinder passes through the natural frequency of the cylinder in vacuum in the transition from upper to lower branch. In this work, frequency is not used as a way for classifying the branches. Instead, the amplitude is the main criterion for categorizing the branches.

Based on experimental results, a slightly different description of the branches is proposed:

- The initial branch, which includes the start of the cylinder oscillations and ends at the point of maximum amplitude. The amplitude increases rapidly.
- The upper branch, starts at the maximum amplitude and contains all points where the amplitude decreases rapidly at a practically constant slope.

- The lower branch, in which a change of slope is observed in the fall of the amplitude (slightly lower or even constant) until the cylinder stops oscillating.

The main difference between groups 1 and 2 lies in the behavior after the maximum amplitude is reached. For group 1, most of the points in the lower branch fit in a single straight line, see Fig. 4.4a. For group 2, a straight line with negative slope can be visualized for points in the upper branch, but a change in the slope (indicating the beginning of lower branch) can be clearly observed, see Fig. 4.4b.

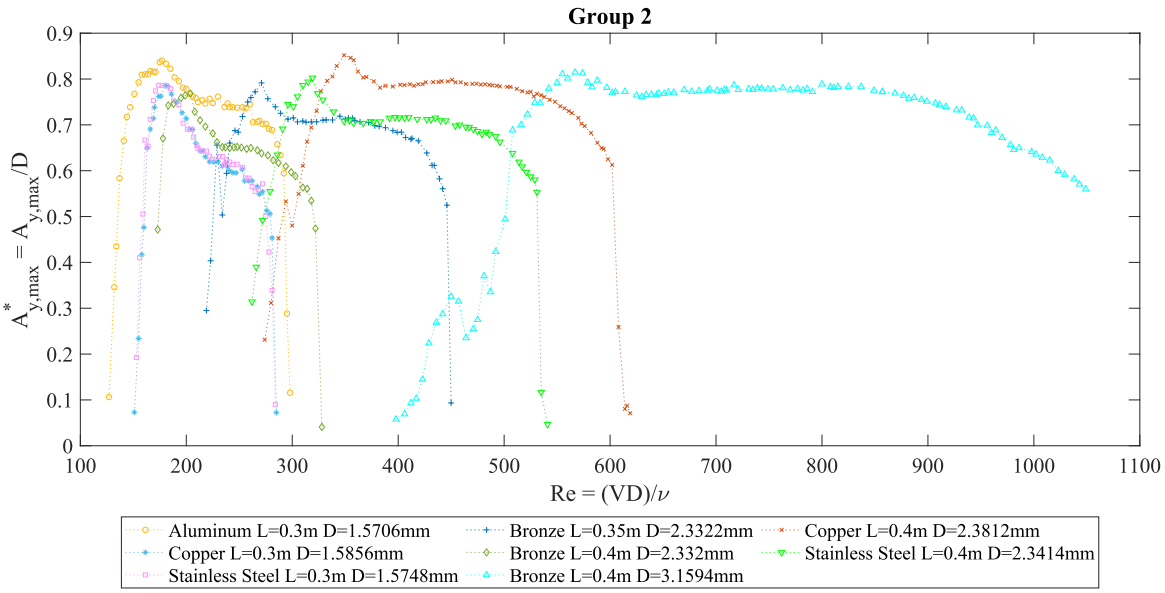

Figure 4.3: Maximum amplitude against Re for different materials, diameters and lengths corresponding to group 2.

In the previous two groups, the maximum amplitude value is always reached somewhere between the natural frequency in vacuum and the natural frequency in the working fluid (water in this case). An example of this can be seen in Fig. 4.4 for each group. The maximum, marked with an arrow, will be named "typical maximum" hereafter.

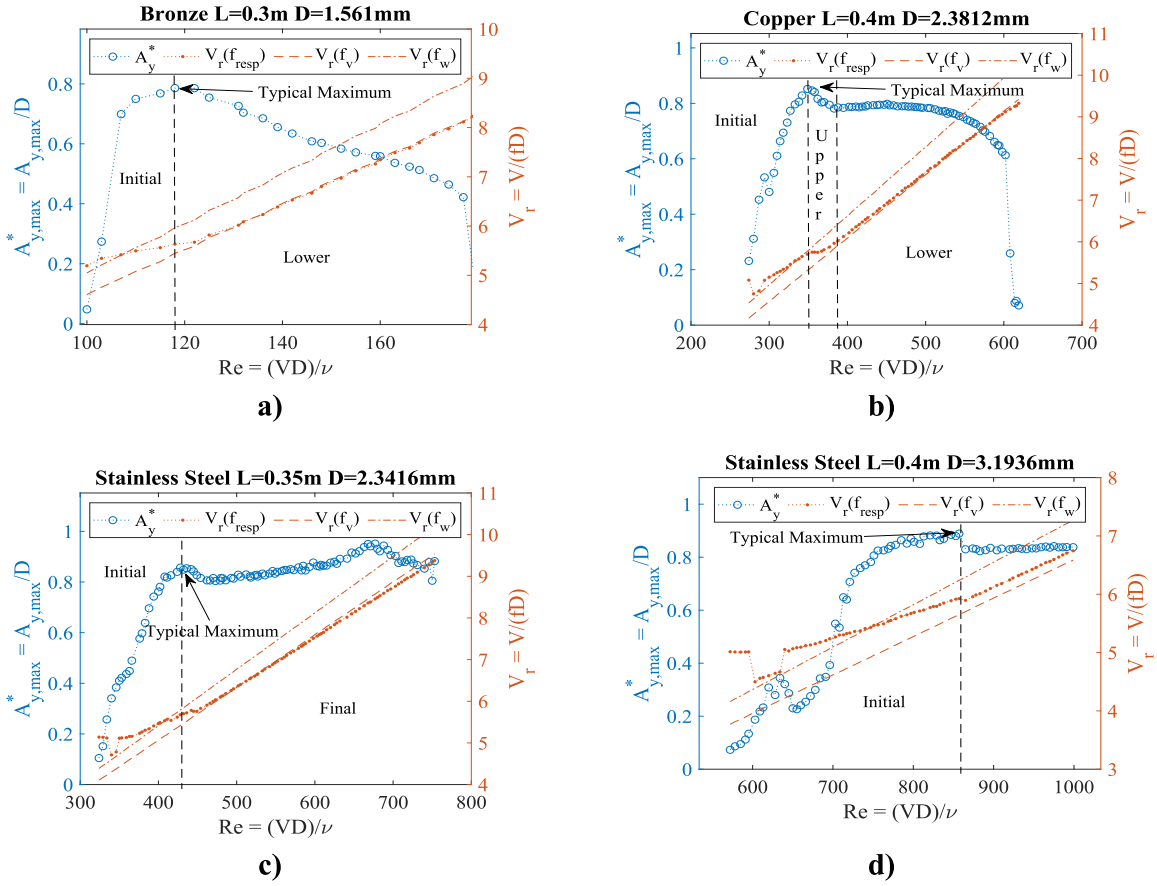

Figure 4.4: Amplitude and reduced velocity against Reynolds number. Selected cylinders corresponding to different groups: a) Group 1; b) Group 2; c) Group 3; d) Group 4.

Fig. 4.5 illustrates the third group. This is characterized by an increase in the amplitude, even after the typical maximum value observed in previous groups (as well in the literature in general). Due to operational limitations of the tunnel, the entire lock-in region of all the cylinders could not be obtained. However, the Re range obtained is wide and sufficient to classify the data into two branches:

- The initial branch, from the starting point of the cylinder oscillations until its typical maximum amplitude is reached (between the natural frequency in vacuum and water).
- The final branch, from the typical maximum amplitude until the cylinder stops oscillating. In this last branch, unlike groups 1 and 2, a gradual increase is observed after the typical maximum until it reaches a second maximum (a global one). In Fig. 4.5, for the case of aluminum cylinder ($L = 40$ cm, $D = 2.3$ mm) the amplitude in this last branch seems similar to a parabola concave downward. For

the case of bronze cylinder ($L = 30$ cm, $D = 2.3$ mm) the amplitude increases constantly until it leaves the lock-in region.

Similar behavior is found in (Yamamoto et al., 2004) in which an amplitude that does not follow the classical conduct is reported, theoretically, for a cantilever flexible cylinder. Furthermore, in (Vicente-Ludlam et al., 2018) their results show a notably similar behavior although they studied a slender elastically mounted circular cylinder with Re ranges from 1500 to 10 000. This remarkable behavior is relevant due to the importance of the maximum (global) amplitude. For some specific applications, like harvesting energy, it is desirable to have large oscillations.

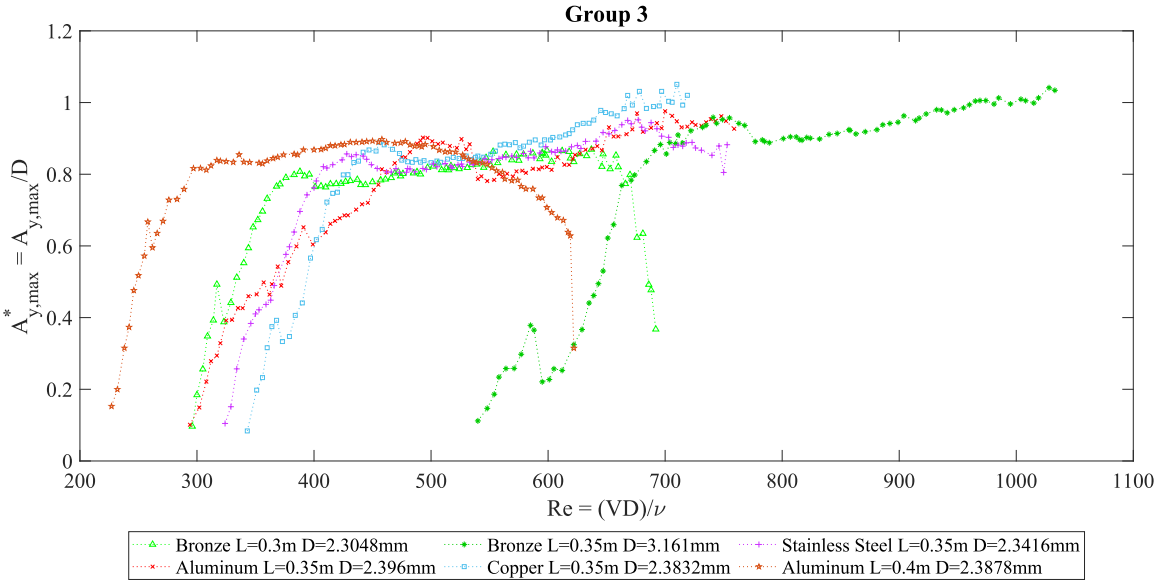

Figure 4.5: Maximum amplitude against Re for different materials, diameters and lengths corresponding to group 3.

Vicente-Ludlam et al. (2018) offer detailed experimental results for a slender elastically mounted circular cylinder under the effect of imposed rotation. For specific values where an amplitude-type extremely similar to group 3 appears, $f^* = f_{resp}/f_d$ reaches a near-constant value after $V_r \approx 10$. According to the authors, this result reinforces the idea that the cylinder undergoes galloping-type oscillations. Although in the present work the f^* is also near-constant, the V_r is around 6 for all the groups.

Moreover, they conclude that a loss in synchronization between vortex shedding and oscillations is responsible for the distinct amplitude responses. However, in at least one cylinder of group 3 this is not the case. It is important to highlight the obviously differences between data for a flexible cylinder and for an elastic cylinder. Not to mention that in this study there is no rotation in the cylinder.

However, Vicente-Ludlam et al. mention that when A^* seems to adopt a quasi-linear dependence on the reduced velocity, it resembles the dependence of galloping-type instability where motion-induced forces are dominant, in contrast to VIV where fluid forces are mainly driven by vortex shedding. This asseveration may apply to flexible cylinders but more detailed experiments in hydrodynamic response is needed.

The fourth group, depicted in Fig. 4.6, includes cylinders that exhibit a notorious amplitude peak in the initial branch. This peak is consistent with a jump in the response frequency. This jump is shown in Fig. 4.4d, where the V_r number decreases its value and then jumps up again, following the typical behavior. In all cases, the jump occurred before the response frequency reaches the natural frequency in the working fluid. In addition, in all cases the amplitude returns to normal behavior also before reaching the natural frequency in the working fluid.

In this group, due to the mentioned operational restrictions, the entire lock-in region could not be achieved. Nevertheless, the peak in the initial branch is clearly shown.

It is important to highlight that not always, based on the experimental results, the maximum amplitude is reached at the exact natural frequency in the working fluid or in vacuum. However, in all the cylinders, a local maximum exists in the amplitude between natural frequencies.

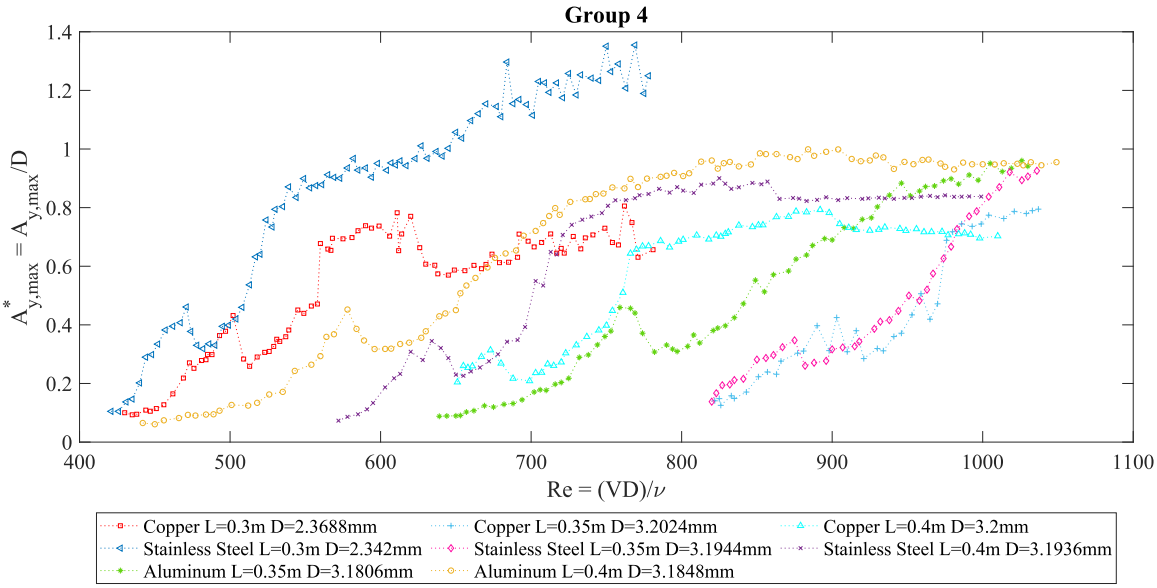

Figure 4.6: Maximum amplitude against Re for different materials, diameters and lengths corresponding to group 4.

To find an adequate parameter for the classification of cylinders into groups one to four, 15 different parameters were analyzed. Fig. 4.7 shows the scatter plot matrix

for material, length, diameter and "groups", represented with colors and markers. A good classifying parameter should show as little dispersion as possible. For instance, focusing attention on the material, there are four (aluminum, bronze, copper and Stainless steel). For material 1, there are four different markers, which means that all four groups are scattered here. This is repeated for all materials. Therefore, this parameter is not a good parameter to classify the groups. Otherwise, all red circles (group 1) would be gathered in a column over material 1, all blue squares over material 2, and so on. The same behavior is observed for lengths, which are three (see Tab. 3.1). In the case of diameter, this classifies correctly group 1 but not the other groups.

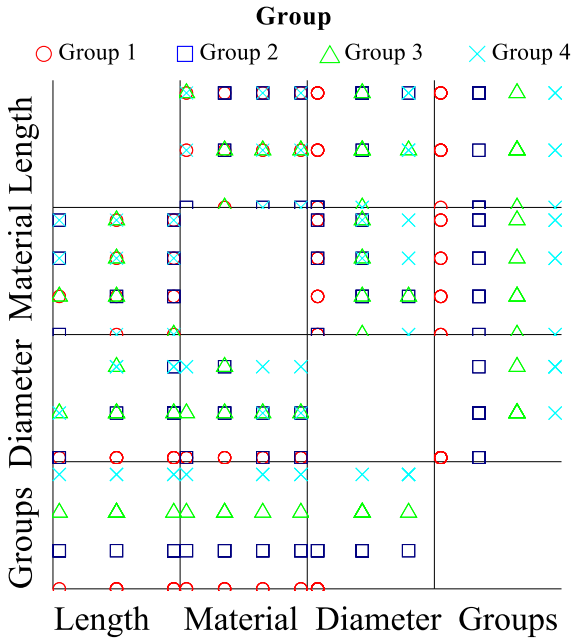

Figure 4.7: Scatter plot matrix between materials, lengths, diameters and groups.

It must be clarified that each point represents one cylinder and that they can be overlapped in Fig. 4.7. Therefore, although the matrix allows appreciating the dispersion of the groups according to the analyzed parameter, Fig. 4.8 is presented with the same analysis but expanding the points to avoid overlapping and detailing the values of parameters. The y axis represents the groups without such overlapping to observe all the cylinders.

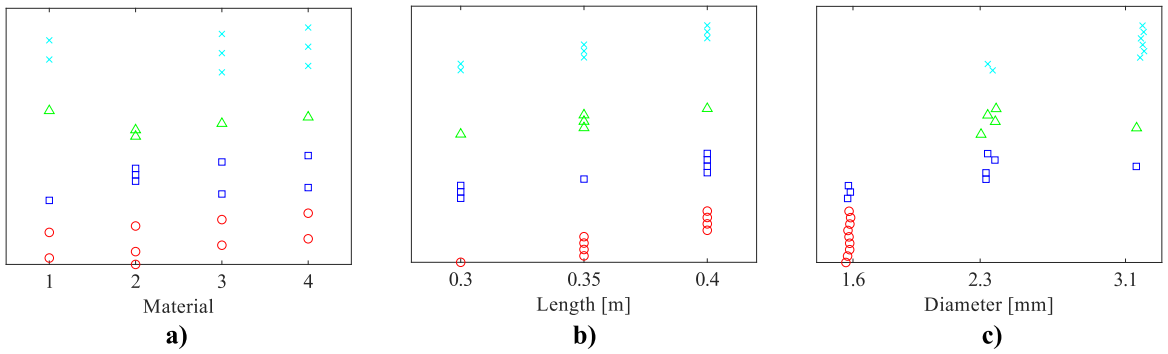

Figure 4.8: Scatter analysis between groups and a) materials: 1-Aluminum, 2-Bronze, 3-Copper, 4-Stainless steel, b) lengths, and c) diameters.

Other parameters analyzed were mass-damping ratio, spring constant, natural frequency in vacuum and in water, among others (Fig. 4.9-Fig. 4.13). The mass ratio is not shown because is equivalent to Fig. 4.8a. None of the parameters shown in Fig. 4.9 or Fig. 4.10 classifies the groups adequately for the same reasons explained in Fig. 4.7 and Fig. 4.8. As in the previous case, Fig. 4.11 is presented for expanding the points to avoid overlapping and detailing the values of parameters.

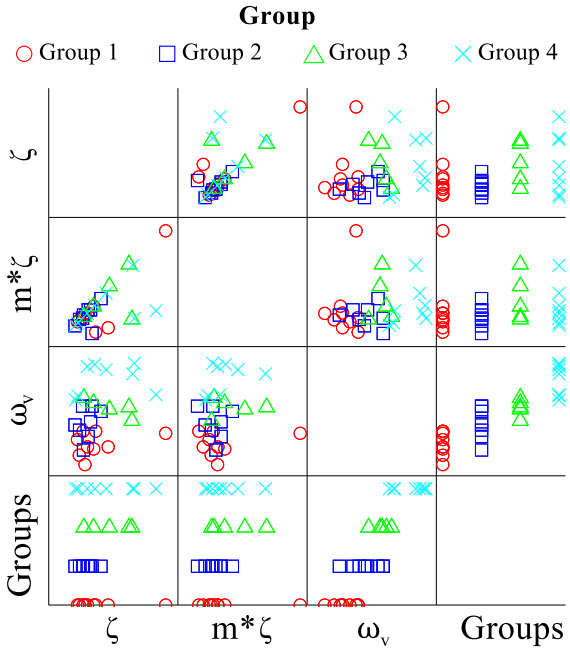

Figure 4.9: Scatter plot matrix between damping ratio, mass-damping parameter, natural frequency in vacuum and groups.

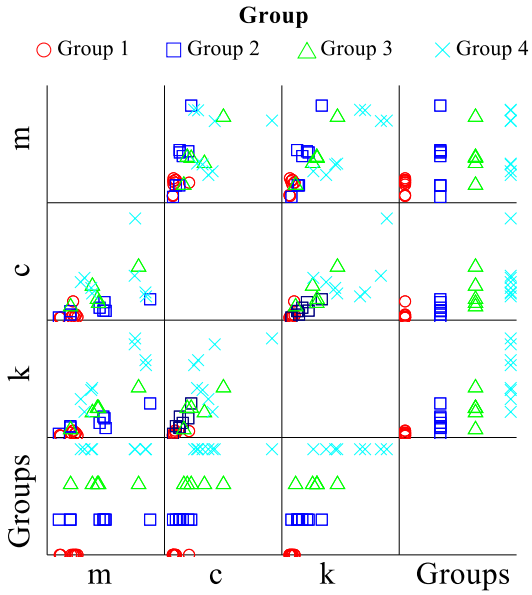

Figure 4.10: Scatter plot matrix between mass, damping coefficient, spring constant and groups.

In Fig. 4.11 the parameters were calculated considering vacuum values for frequency and damping ratio, and without considering the added mass. The parameters shown in Fig. 4.12 and Fig. 4.13 were calculated considering water as the working fluid. However, as shown, even with these parameters there is not a good classification.

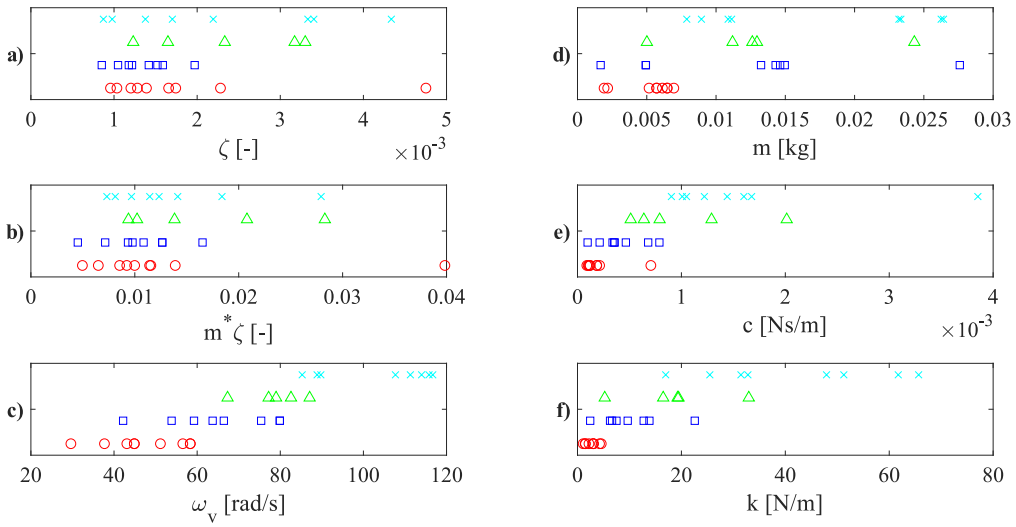

Figure 4.11: Scatter analysis between groups and a) damping ratio, b) mass-damping ratio, c) natural frequency in vacuum, d) mass, e) damping coefficient and f) spring constant.

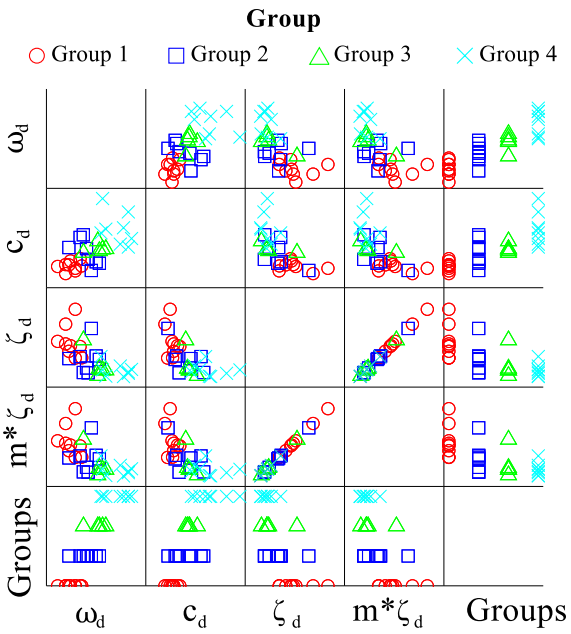

Figure 4.12: Scatter plot matrix between natural frequency in water, damping coefficient in water, damping ratio in water, mass-damping ratio in water and groups.

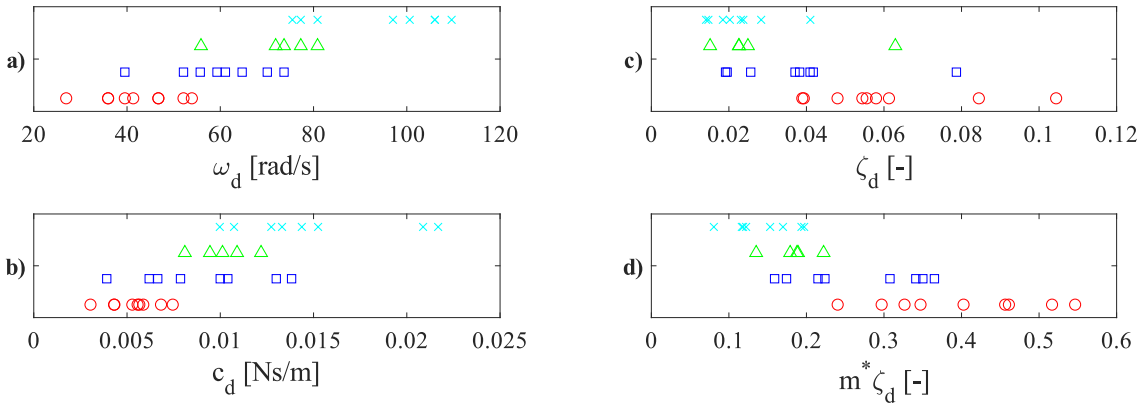

Figure 4.13: Scatter analysis between groups and a) natural frequency in water, b) damping coefficient in water, c) damping ratio in water, d) mass-damping ratio in water.

The analysis corresponding to the slope obtained between V_r and Re numbers is represented in Fig. 4.14. To appreciate the results in a better way, in Fig. 4.15a all points have the same height and in Fig. 4.15b each group has been separated. The classifica-

tion is almost perfect except for two cylinders: a blue square (group 2) and a green triangle (group 3) located out of their corresponding ranges.

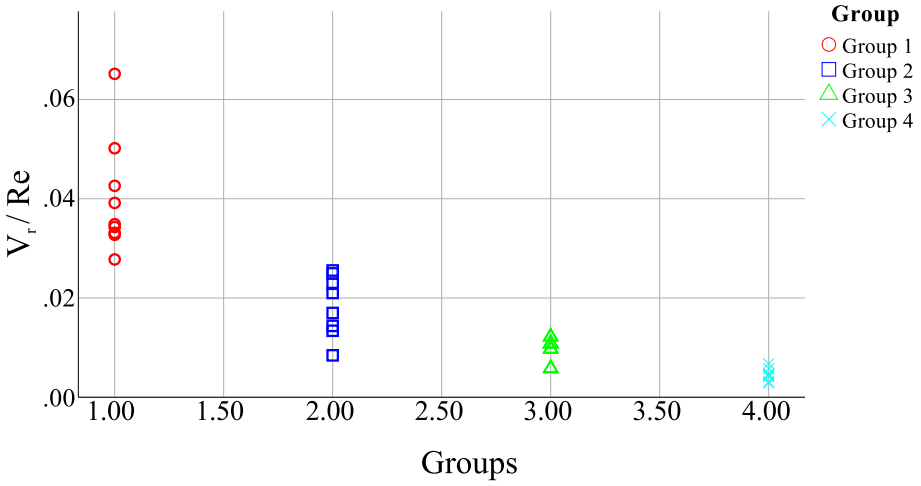

Figure 4.14: Scatter plot between the slope of V_r vs Re and groups.

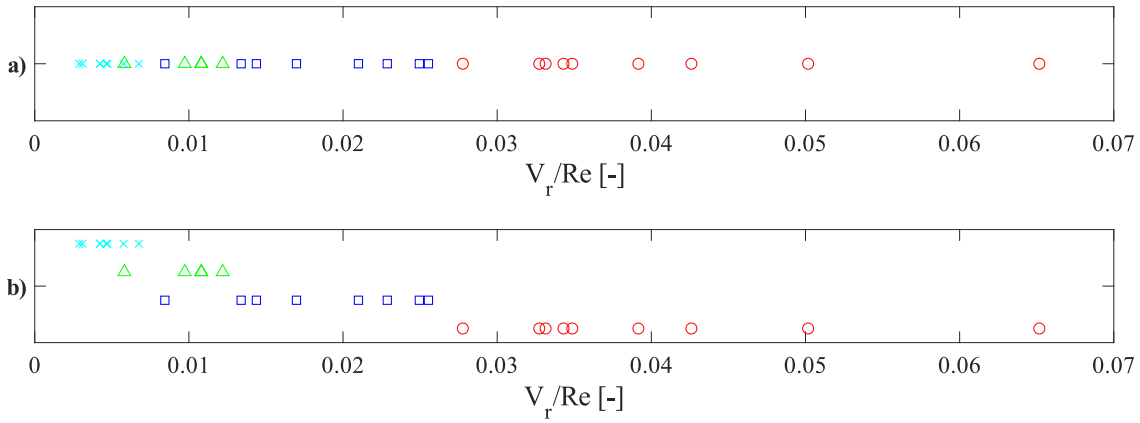

Figure 4.15: Scatter analysis between groups and V_r vs Re slope.

A closer analysis demonstrates that both cylinders have a jump in frequency, which corresponds perfectly with the characteristic behavior of group 4, see Fig. 4.16. In Fig. 4.16a the cylinder amplitude exhibits behavior as described in group 2, but it shows a jump in frequency and amplitude at the initial branch as described in group 4. Similarly, in Fig. 4.16b the cylinder presents characteristics of group 3 but also shows a jump at the initial branch as group 4.

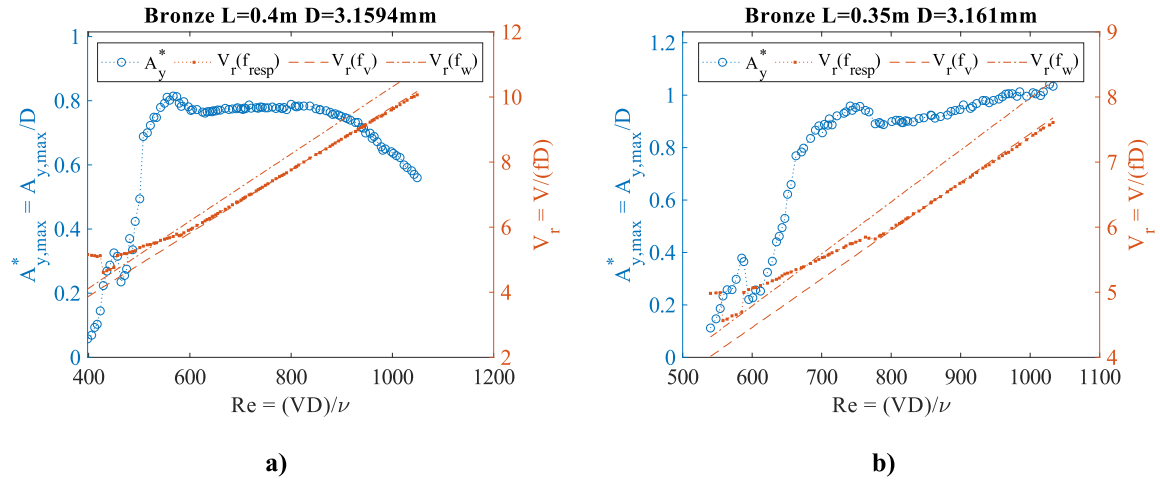

Figure 4.16: Amplitude and reduced velocity against Reynolds number. Selected cylinders: a) group 2 and b) group 3.

In Fig. 4.17 all the cylinders tested are shown in the same plot. This time each line represents one cylinder. Even so, the groups are still well classified. The cylinders labeled in Fig. 4.17 as "Cylinder A" and "Cylinder B" correspond to Fig. 4.16a and Fig. 4.16b, respectively.

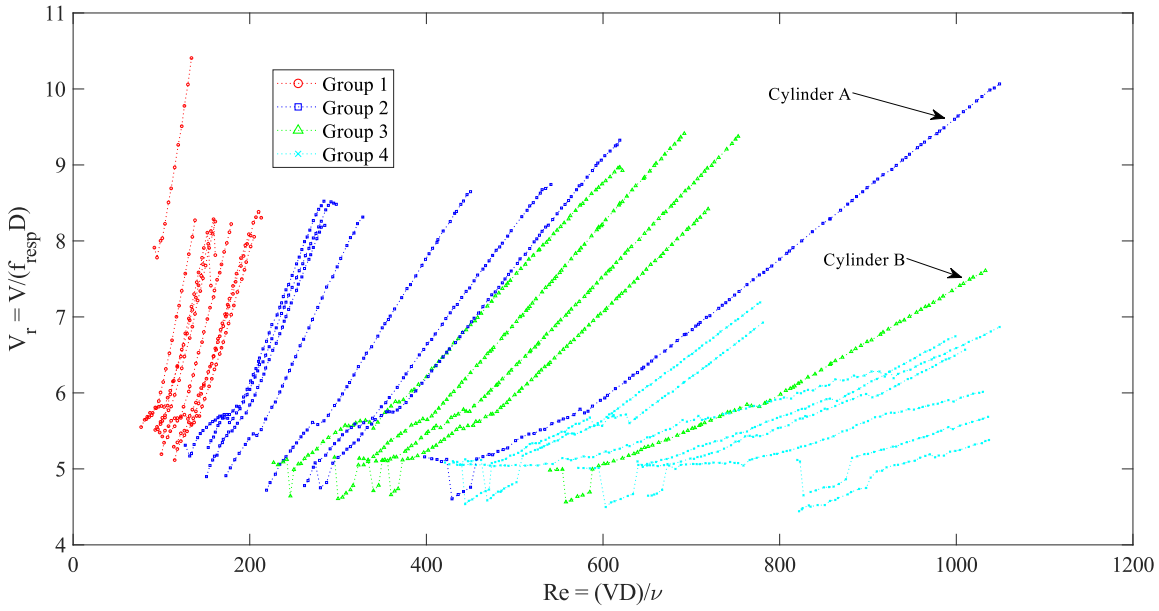

Figure 4.17: V_r vs Re for the four different groups.

The experimental data obtained in this work can be classified according to this pa-

rameter as follows:

Group	Range ($\times 10^{-3}$)
Group 1	$65.1 > V_r/Re > 27.7$
Group 2	$25.5 > V_r/Re > 8.4$
Group 3	$12.2 > V_r/Re > 5.8$
Group 4	$6.7 > V_r/Re > 2.9$

Table 4.1: Group classification according to V_r/Re parameter.

These ranges are valid for flexible cylinders in cantilever vibrating at their first mode and operational conditions and geometrical ranges specified in sec. 3.2. To interpolate the results obtained in this work, a 2D polynomial linear fit is presented, see Fig. 4.18.

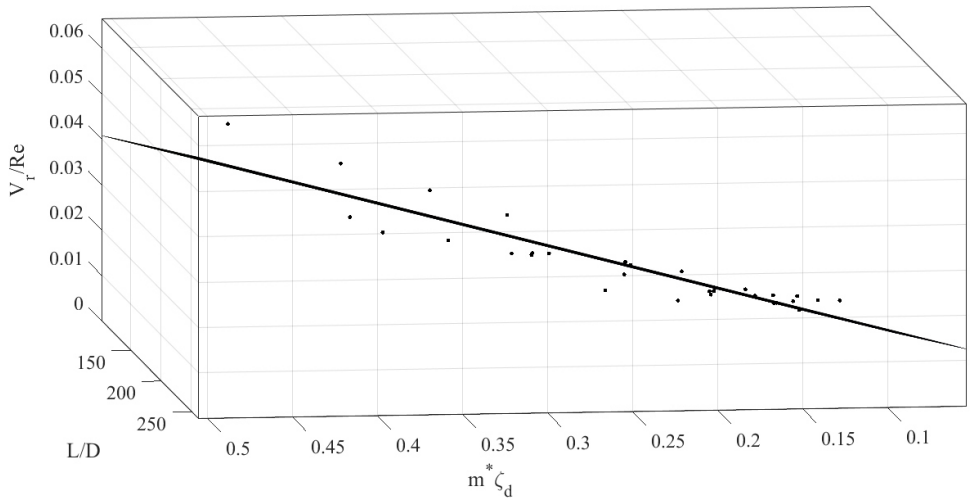

Figure 4.18: Polynomial linear model plot used to predict V_r/Re using L/D and ω_v.

The curve fitting equation is described by Eq. (3) with 95% confidence.

$$\frac{V_r}{\mathrm{Re}} = C_0 + C_1 \times \omega_v + C_2 \times \left(\frac{L}{D}\right) \tag{4.1}$$

The coefficient values are shown in Tab. 4.2. Resulting in a goodness of fit of $R^2_{adj} = 0.8213$.

Coefficient	Value
C_0	-0.008227
C_1	-0.0001579
C_2	0.0002312

Table 4.2: Coefficients of polynomial fit equation-

By knowing only the L/D ratio and ω_{vacuum} before performing experiments through the entire synchronization zone, Eq. 4.1 can be used to predict the maximum amplitude behavior for a given cylinder. If a certain behavior is more useful for an application, then the cylinder can be selected based on the V_r/Re parameter.

4.2 Natural frequencies in water and vacuum

This section presents the experimental results obtained through the synchronization regime for all the cylinders tested. By following the procedure described in subsection sec. 2.2.2.2, the natural frequencies were obtained for the first mode. The experimental and calculated values corresponding to natural frequencies in vacuum and water, ω_v and ω_d, are presented in Tab. 4.3.

Material	L [m]	$\alpha = L/D$	$\omega_{v,exp}$	$\omega_{v,calc}$	$\omega_{w,exp}$	$\omega_{w,calc}$
Aluminum	0.30	191.01	79.89	75.68	64.69	70.42
Aluminum	0.35	222.90	58.34	56.02	46.72	53.03
Aluminum	0.35	110.04	116.69	113.37	97.03	108.30
Aluminum	0.40	254.39	44.88	43.16	35.94	40.69
Aluminum	0.40	167.52	67.32	65.63	55.86	61.54
Aluminum	0.40	125.60	89.76	87.36	75.47	80.39
Bronze	0.30	192.18	51.16	53.31	46.72	52.49
Bronze	0.30	130.16	78.99	78.95	73.67	74.45
Bronze	0.35	221.27	37.70	39.87	35.94	37.82
Bronze	0.35	150.07	53.86	58.96	52.11	55.27
Bronze	0.35	110.72	77.19	79.95	71.88	71.97

Material	L [m]	$\alpha = L/D$	$\omega_{v,exp}$	$\omega_{v,calc}$	$\omega_{w,exp}$	$\omega_{w,calc}$
Bronze	0.40	252.68	29.62	30.69	26.95	28.96
Bronze	0.40	171.53	42.19	45.41	39.53	42.65
Bronze	0.40	126.61	59.24	61.36	55.70	58.60
Copper	0.30	189.20	79.89	72.03	73.67	72.40
Copper	0.30	126.65	115.79	106.99	109.61	109.22
Copper	0.35	221.24	58.34	52.86	53.91	53.51
Copper	0.35	146.86	87.07	79.64	80.86	80.00
Copper	0.35	109.29	113.99	107.46	106.02	106.75
Copper	0.40	252.05	44.88	40.93	41.33	41.04
Copper	0.40	167.98	66.42	61.25	61.09	61.23
Copper	0.40	125.00	88.86	82.56	80.86	81.79
Stainless Steel	0.30	190.50	75.40	72.93	70.08	71.94
Stainless Steel	0.30	128.10	111.30	108.69	160.02	106.32
Stainless Steel	0.35	221.77	56.55	54.04	52.11	52.40
Stainless Steel	0.35	149.47	82.58	80.04	77.27	77.55
Stainless Steel	0.35	109.57	107.71	109.52	100.63	103.30
Stainless Steel	0.40	253.42	43.08	41.53	39.53	41.49
Stainless Steel	0.40	170.84	63.73	61.53	59.30	61.33
Stainless Steel	0.40	125.25	85.27	84.22	77.27	81.33

Table 4.3: Experimental vs theoretical values for natural frequency in water and vacuum, all frequencies are in rad/s.

4.3 Comparison with results found in literature

Griffin et. al (1975). made the first compilation of results from different researches in VIV and compared them using the same parameter, the Skop-Griffin parameter S_G. In sec. 2.5.2, a brief history of the Griffin plot is given.

Fig. 4.19 shows the modified Griffin plot, presented in Williamson & Govardhan (2004), overlaying data from experimental results obtained in this thesis. Each point in the plot represents the maximum amplitude of one cylinder through the entire synchronization

regime. Gray bullet points represent Williamson & Govardhan data and colored points correspond to data from this work.

At a glance, data reported here seem to fit well in the plot. However, this plot has a logarithmic scale on the x-axis. If the scale is replaced with a linear scale, with the same limits, the representation loses sense (see Fig. 4.20a). To avoid this, a zoom-in is made in Fig. 4.20b. In this plot data still seem to fit well.

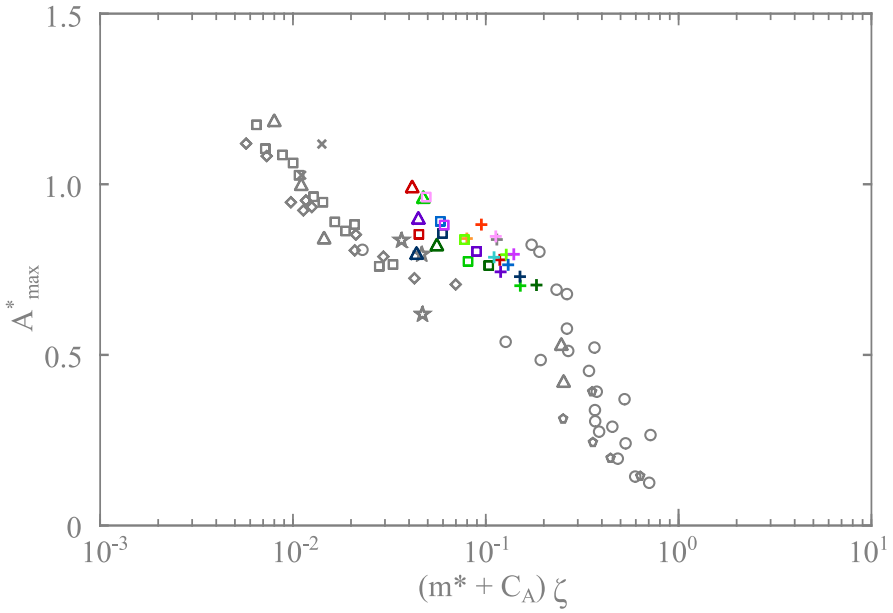

Figure 4.19: Modified griffin plot with a logarithmic scale in the x-axis, overlapping data from this work.

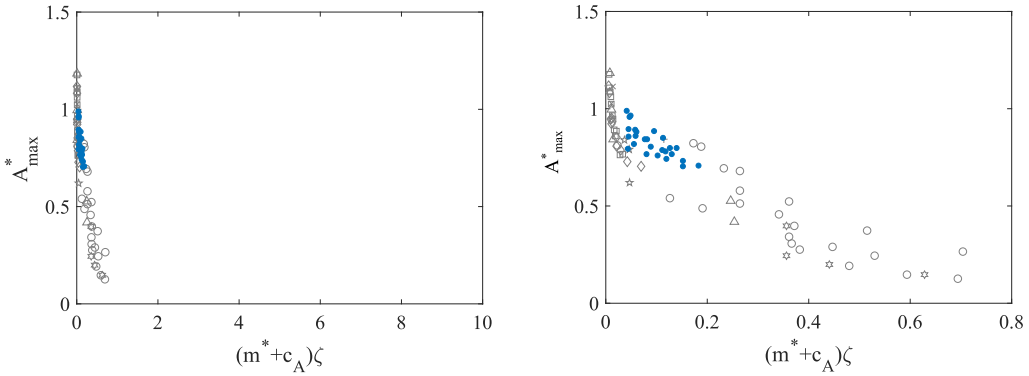

Figure 4.20: Modified Griffin plot with linear scale in the x-axis. In a) holding the limits, and b) with zoom in.

Finally, to prove if data truly matches the Griffin plot a curve fitting was performed with and without data from this work. The solid line represents the model for original data only with a $R^2 = 0.8761$. The dotted line describes original plus actual data with a $R^2 = 0.7842$. A lower R-square number is a signal that it will be "more problematic" to predict data with reasonable accuracy. The original model will underestimate the amplitude for cantilevered uniform flexible circular cylinders. An even wider study in this type of cylinders is needed to fulfill the Griffin plot and clearly see if there is a specific model that can suite accurate amplitude predictions. Regarding the groups explained in this chapter, no relevant observation was made suggesting that amplitude is specifically dependent on group classification.

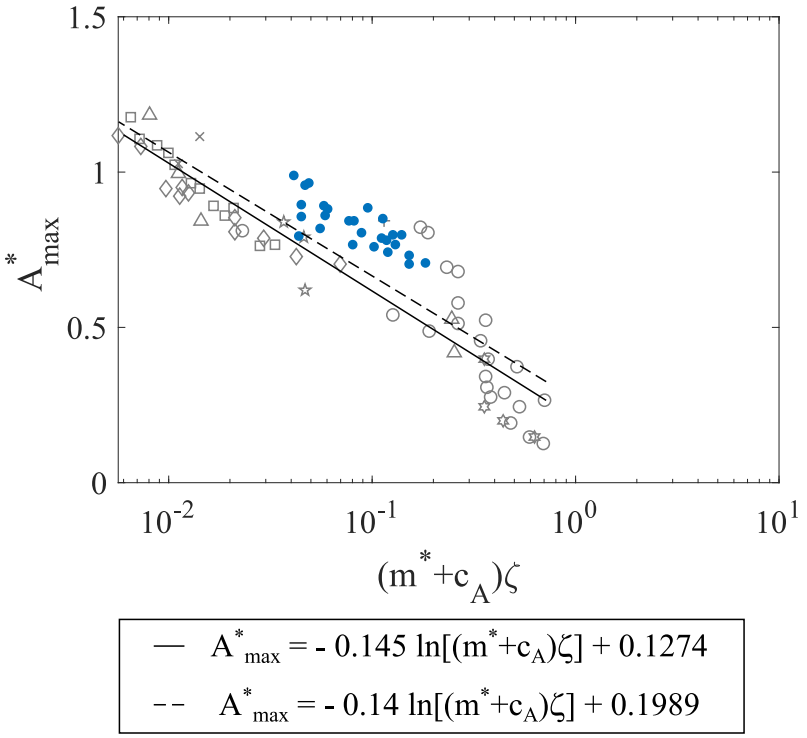

Figure 4.21: Comparison between modified Griffin plot (Williamson & Govardhan) and modified Griffin with actual data.

5 Results and discussion of modes of vortex shedding in the Williamson-Roshko map.

For a stationary cylinder with Re $\gtrsim$ 40, the wake structure is the classic von Kármán vortex street. In Fig. 2.15 the flow regimes around a smooth fixed circular cylinder in a steady current are shown. However, for cylinders undergoing vortex induced vibrations, the vortex shedding modes can vary (Fig. 1.20). In this chapter, the hydrodynamic response is detailed across the four different groups described in chapter 4. One cylinder was selected for each group and its main hydrodynamic characteristics are discussed. The vortex shedding modes and cylinder trajectories are illustrated at different V_r values.

5.1 Vortex shedding mode along the lock-in region

This section presents the experimental results obtained through the synchronization regime for the four cylinders selected. Fig. 5.1 presents the maximum amplitude against Re, and the vortex shedding mode, for the cylinder corresponding to group 1. All the images show the cylinder at the upper maximum amplitude of the cycle. In the entire synchronization regime, the vortex shedding is a 2S mode. This means two single vortices per cycle of oscillation.

For the initial branch (Re $<$ 103) it can be observed that the trajectory of the cylinder is a thin vertical line and the vortices are shed in two different horizontal lines, one for the clockwise and other for the counter-clockwise. These lines are close enough so that there is no free stream street between the vortex lines. At the maximum amplitude of the lock-in region, the trajectory has an eight-shape and the vortex lines are separated by a free stream street. In the lower branch (Re $>$ 103), the eight-shape trajectory starts to collapse into a vertical line and the vortex lines start to approach each other and the free stream street disappears.

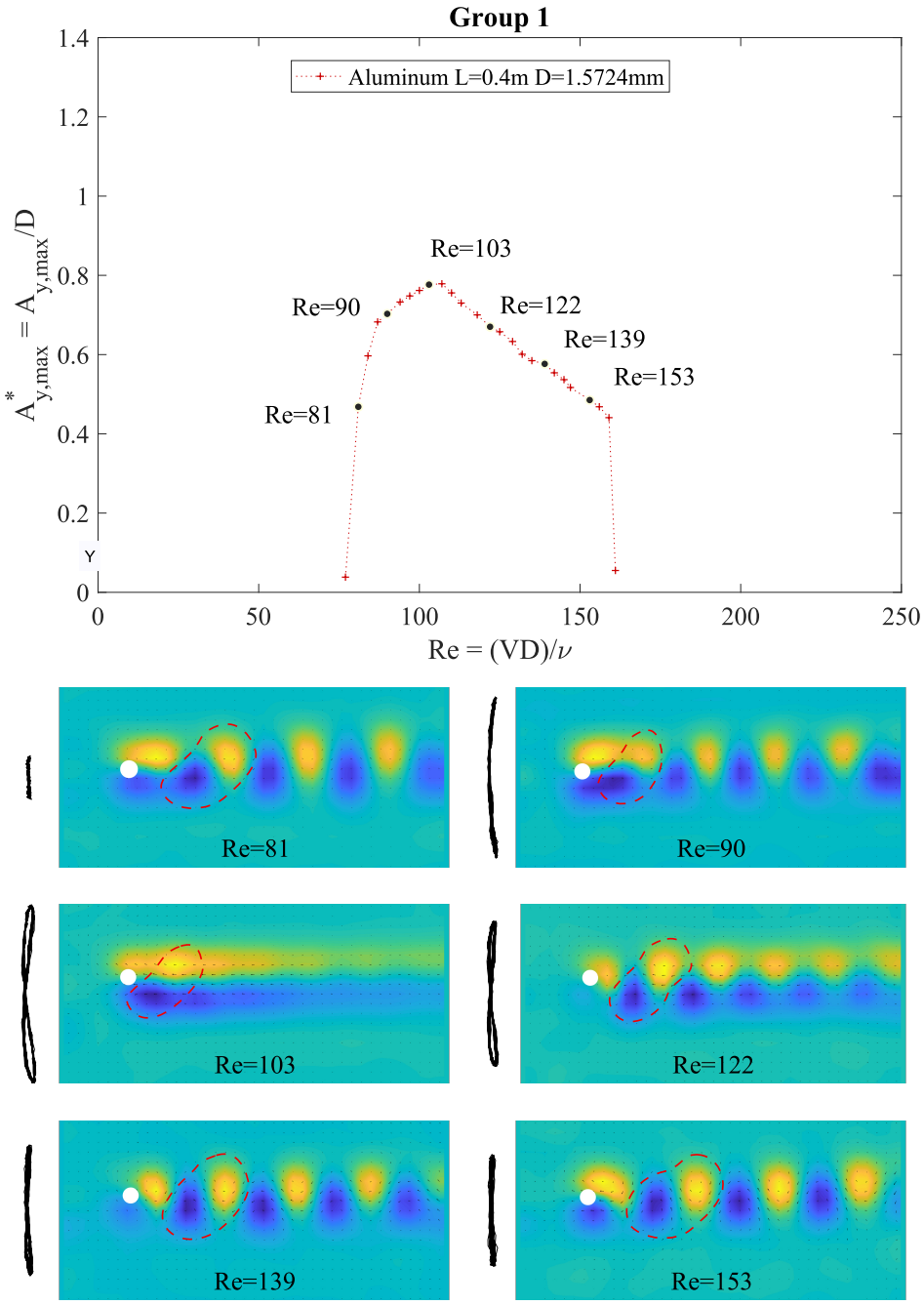

Figure 5.1: Vortex shedding mode for Aluminum $L = 0.4$ m and $D = 1.5724$ mm cylinder (Group 1). Yellow vortex is clockwise (CW) and blue are counter-clock wise (CCW) direction.

For the case of group 2, Fig. 5.2 allows appreciating the modes 2S, P+S, and 2P. Each

pattern is defined by the number of pairs and single vortices formed per cycle. S and P mode implies a single vortex and a vortex pair, respectively. In the initial branch ($Re < 355$), the only shedding mode is the 2S. At the beginning of the synchronization regime, the vortex lines are relatively close. As the Re increases, the distance between the vortex lines also increases whereas the trajectory remains as a thin vertical line. In the upper branch ($355 < Re < 396$), although the trajectory shape is the same, the vortex shedding mode jumps to a P+S (one pair and one single vortex are shed per cycle of oscillation). Here two CCW direction vortices and only one CW are shed. The CW vortex is placed vertically at the center of the other two vortices. The CCW vortex pair is separated downstream. In the lower branch ($Re > 396$) the P+S mode dominates until the amplitude decreases rapidly. In this last section, the 2P mode appears. Across this branch, the cylindrical trajectory remains the same and the only change in the hydrodynamics is the time that the separation of the two CCW vortices takes. As the Re increases, the vortex pair is separated in a shorter time. Finally, at the very last section of the lower branch, the 2P mode appears and four vortices are shed in each cycle, two CW and two CCW.

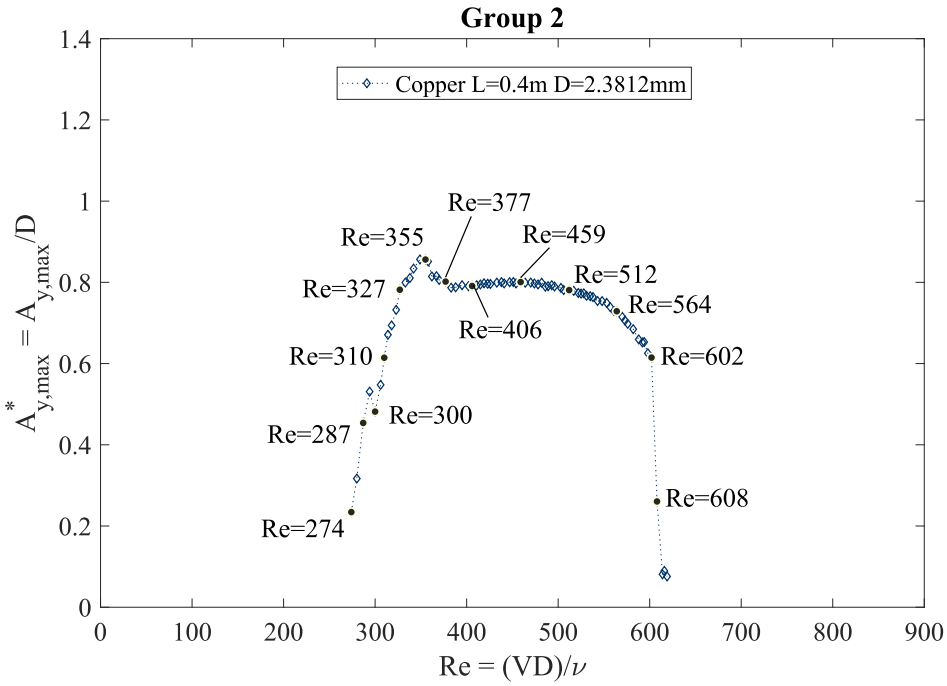
Group 2
Copper L=0.4m D=2.3812mm
Re=377
Re=355
Re=459
Re=327
Re=512
Re=564
Re=406
Re=310
Re=602
Re=300
Re=287
Re=608
Re=274
$A^*_{y,max} = A_{y,max}/D$
Re = (VD)/ν

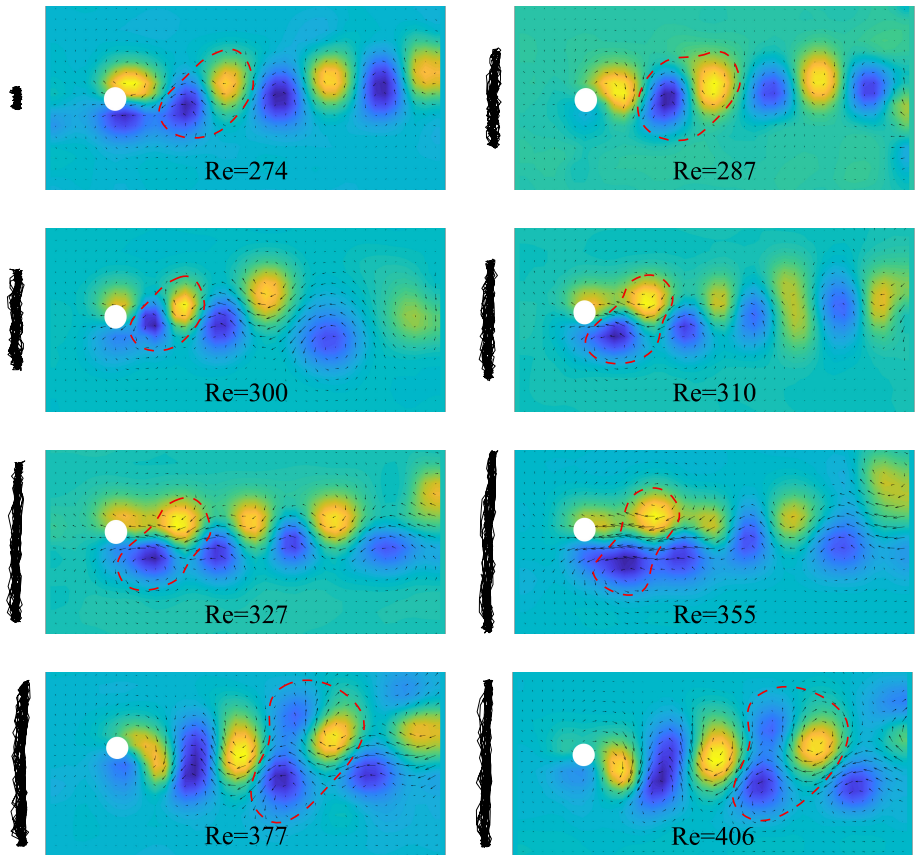
Re=274
Re=287
Re=300
Re=310
Re=327
Re=355
Re=377
Re=406

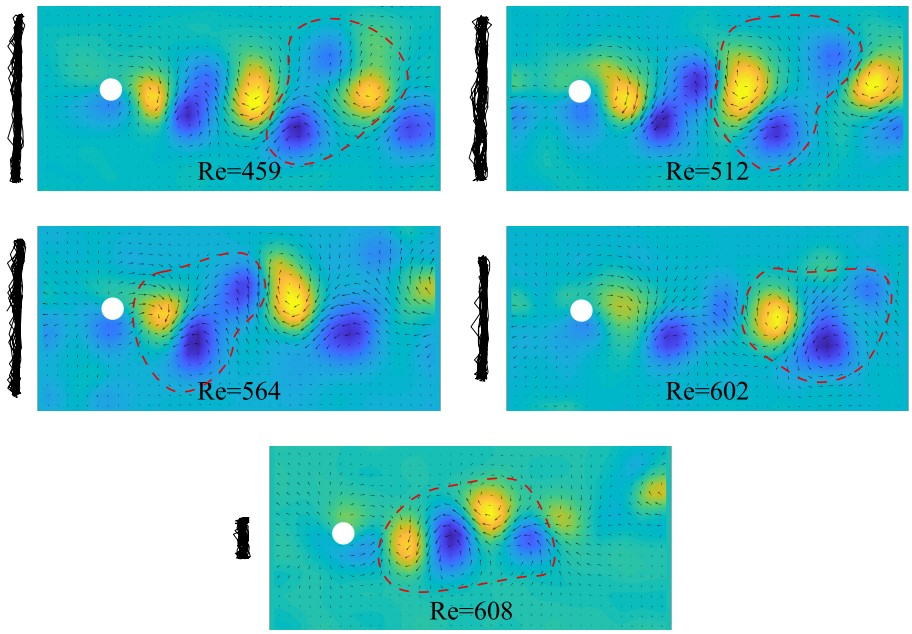

Figure 5.2: Vortex shedding mode for Copper $L = 0.4$ m and $D = 2.3812$ mm cylinder (Group 2).

Fig. 5.3 depicts the results corresponding to group 3. Two branches, the initial and final, are distinguished. The initial branch (Re $<$ 345) is dominated by the 2S mode. The trajectory begins as a thin line but as Re increases, the line widens gradually. In the final branch (Re $>$ 345), the vortex shedding mode undergoes a transition from 2S to P+S to 2P. The P+S mode, two CCW and one CW can be seen from the typical maximum to the global maximum. From there on the 2P mode is observed. It is important to note that in the last two images the CW vortex pair is separated downstream, even tough it is not shown.

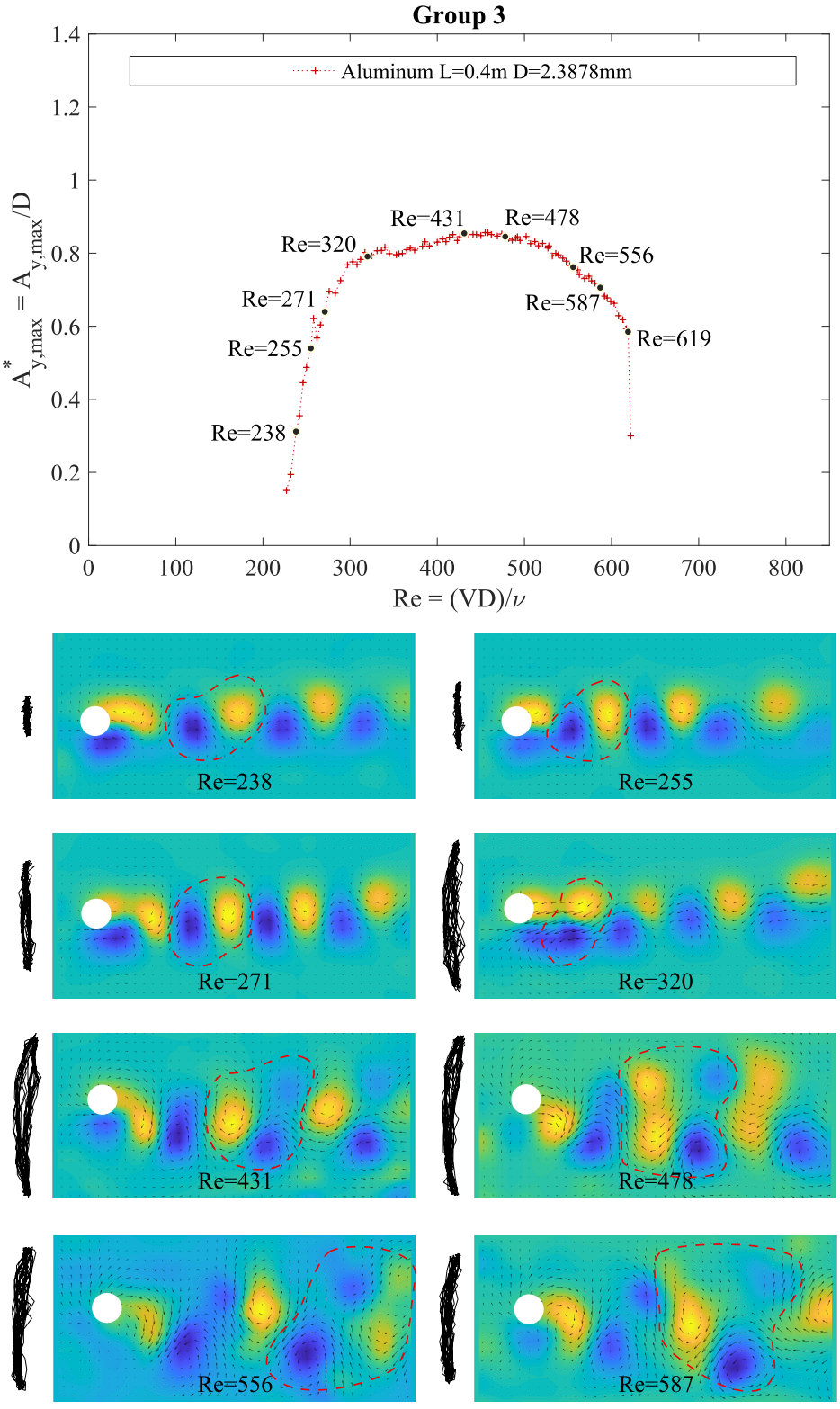
Group 3
Aluminum L=0.4m D=2.3878mm
$A^*_{y,max} = A_{y,max}/D$
Re = (VD)/ν
Re=238
Re=255
Re=271
Re=320
Re=431
Re=478
Re=556
Re=587
Re=619

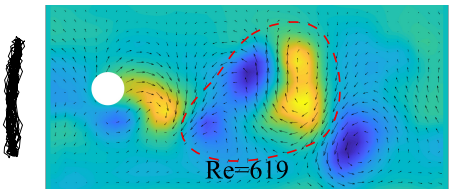

Figure 5.3: Vortex shedding mode for Aluminum $L = 0.4$ m and $D = 2.3878$ mm cylinder (Group 3).

Finally, group 4 (Fig. 5.4) includes cylinders that exhibit a notorious amplitude peak in the initial branch. This peak is consistent with a jump in the response frequency. In the beginning, the trajectory of the cylinder is a thin vertical line and the vortices are shed in two different horizontal lines. The vortex lines are nearby and they separate until the amplitude reaches its typical maximum. In this region, the vortex shedding mode is 2S. Passing this peak, where the amplitude starts to increase again, the mode switches to a 2P and the trajectory becomes a wider line.

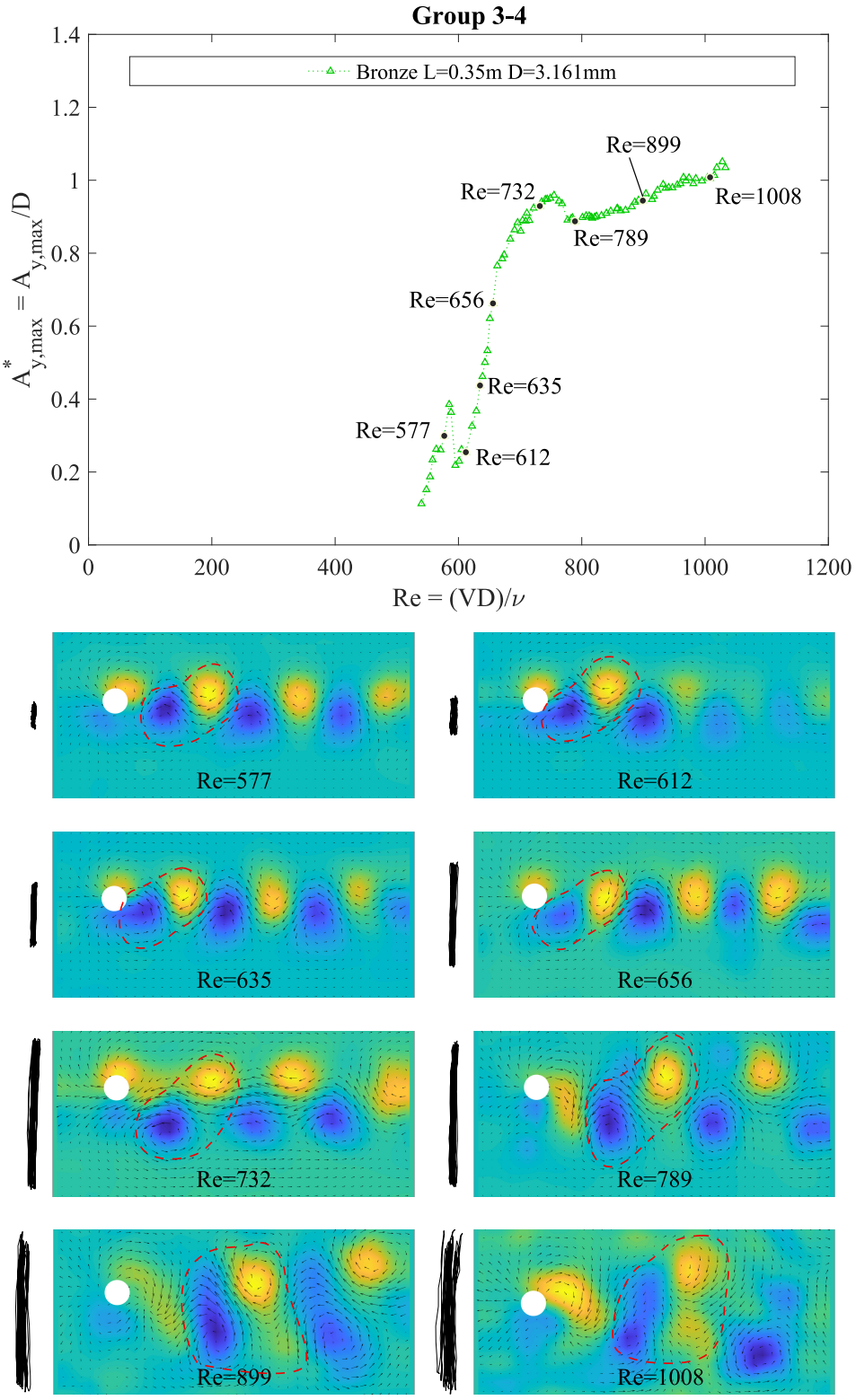

Figure 5.4: Vortex shedding mode for Bronze $L = 0.35$ m and $D = 3.161$ mm cylinder (Group 4).

Even though the hydrodynamics alone is not enough to explain the different behavior among the groups, the jump between modes are aligned with most of the different branches in each group.

5.2 Vortex shedding mode in the Williamson Roshko map

The Williamson & Roshko (1988) map of vortex modes was originally developed for forced transverse oscillations of circular cylinders. Govardhan & Williamson (2000) pointed out that this map collapses well with different systems including transverse freely oscillating elastically mounted cylinders. However, when the cylinder amplitudes obtained in this work are overlaid on the W-R map, it can be seen that the modes do not coincide. From Fig. 5.5 to Fig. 5.8, the different groups in the W-R map are shown.

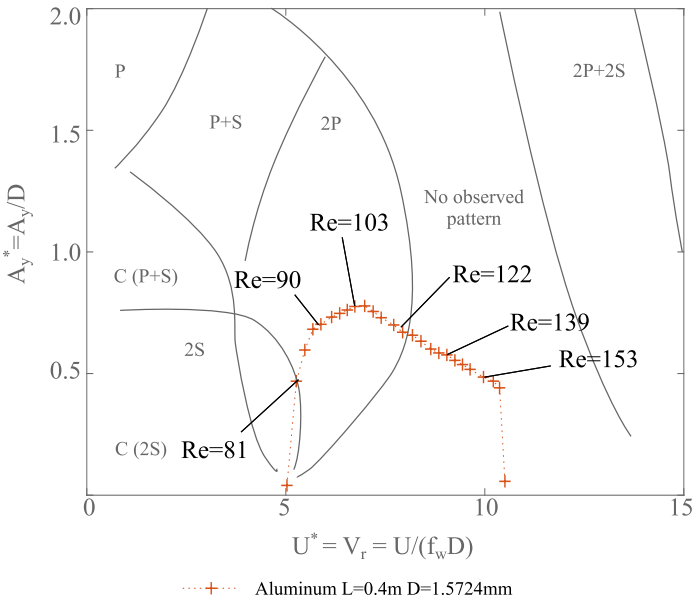

Figure 5.5: Hydrodynamic response in the W-R map for Aluminum $L = 0.4$ m and $D = 1.5724$ mm cylinder (Group 1).

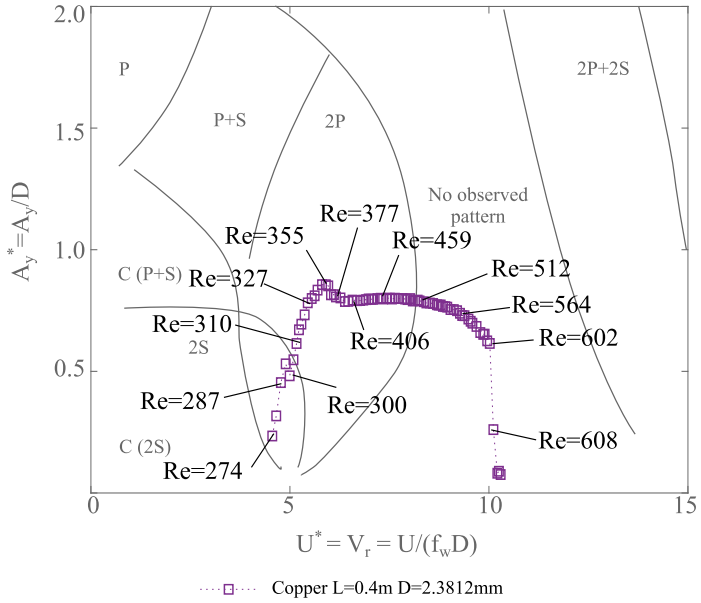

Figure 5.6: Hydrodynamic response in the W-R map for Copper $L = 0.4$ m and $D = 2.3812$ mm cylinder (Group 2).

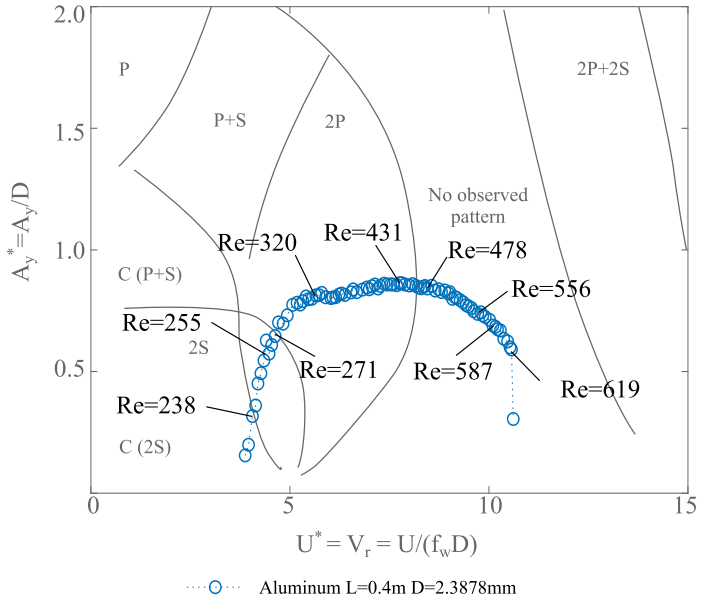

Figure 5.7: Hydrodynamic response in the W-R map for Aluminum $L = 0.4$ m and $D = 2.3878$ mm cylinder (Group 3).

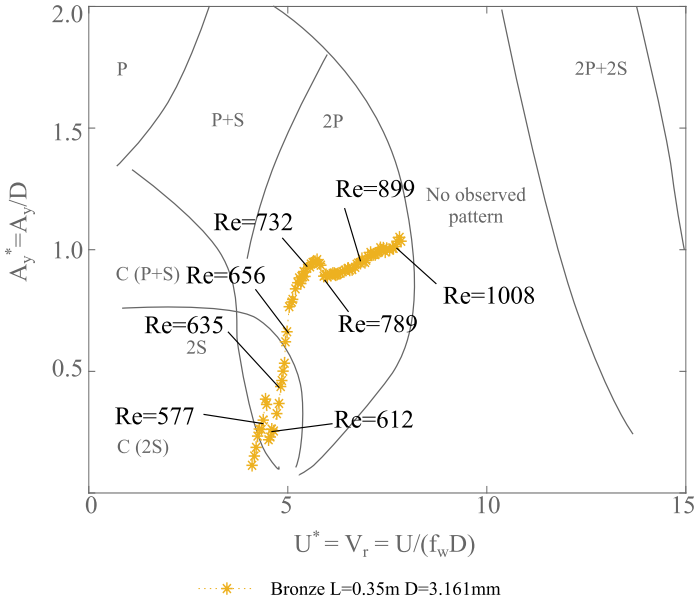

Figure 5.8: Hydrodynamic response in the W-R map for Bronze $L = 0.35$ m and $D = 3.161$ mm cylinder (Group 4).

Fig. 5.9 to Fig. 5.11 reveal the discordance between the Williamson Roshko map, developed for forced transverse oscillations, and the modes originated by *cantilevered uniform flexible circular cylinder*s. This clearly shows that not only the original W-R map is not suitable for all the different cylinders but, also, that even in the same type of cylinders this map is variable depending on the group classification. The P+S mode of group 3 is overlaid with the 2P mode from group 4.

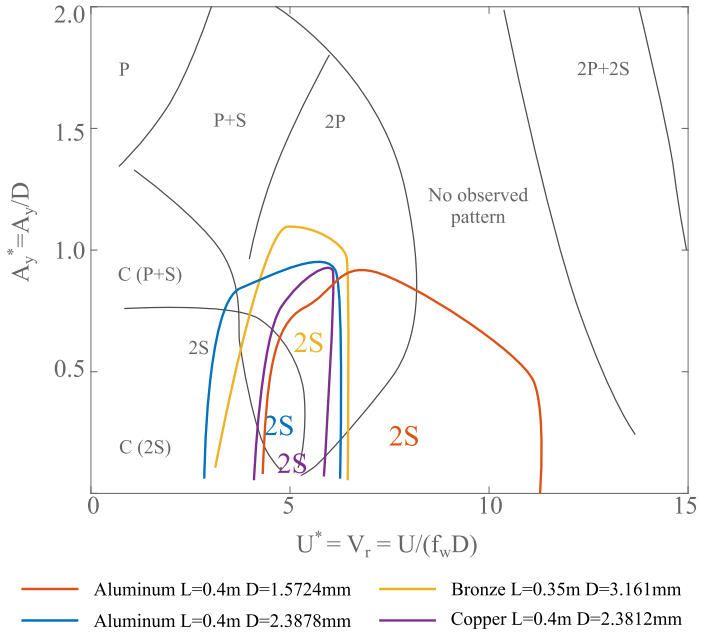

Figure 5.9: W-R map for 2S vortex shedding mode.

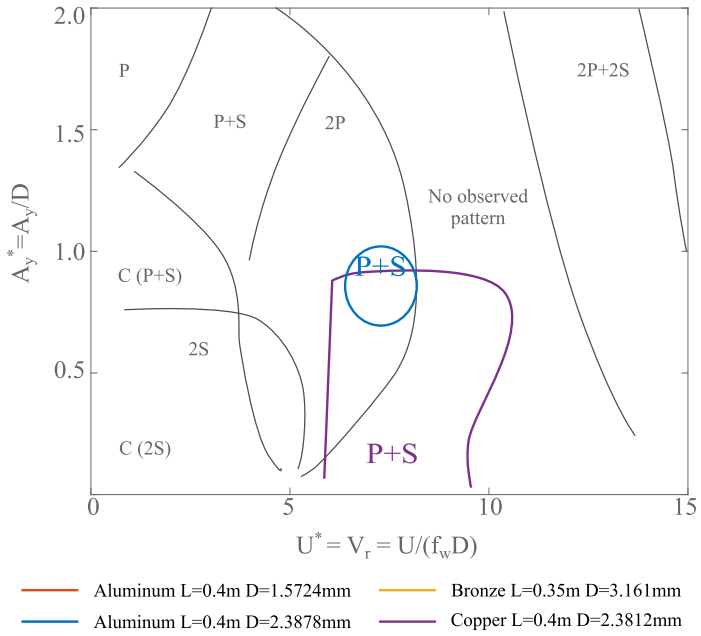

Figure 5.10: W-R map for P+S vortex shedding mode.

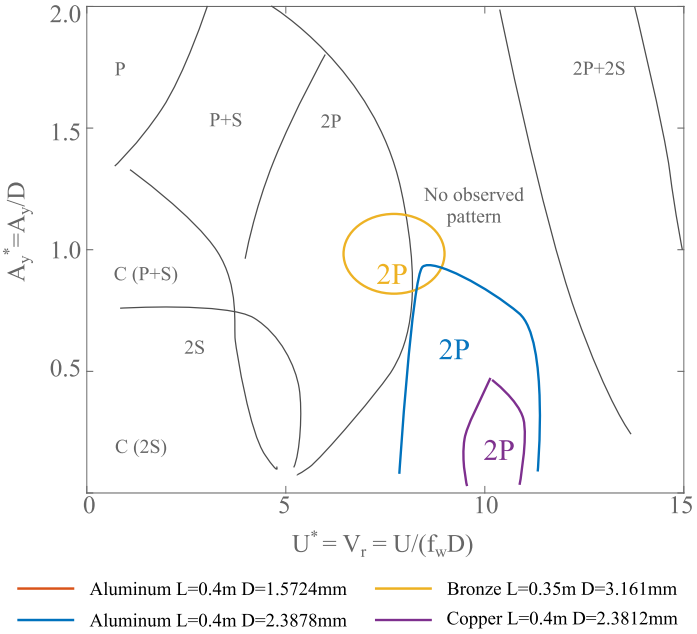

Figure 5.11: W-R map for 2P vortex shedding mode.

Conclusions

In this work, an experimental apparatus was built in order to investigate the vortex-induced vibrations (free oscillations) of a *cantilevered uniform flexible circular cylinder* in a steady current along the entire lock-in region. A Matlab ® code was developed to determine the dynamic response of the cylinder using the PTV technique. For the hydrodynamic response, in order to use the PIV technique, a customized system to seed the fluid was constructed. Conclusions derived from this study are:

- Experimental results demonstrate the existence of four distinct groups, corresponding to different behaviors of the maximum amplitude as a function of Re.
  - Group 1 is observed mainly in the smallest diameter cylinders, regardless of height and material. It consists only of two branches.
  - Group 2 represents the most common response found in the literature. It consists of three different branches. Contrary to the typical classification based in frequency, here an amplitude-based criterion is proposed.
  - Group 3 is rarely described in the literature and, as far as the authors are aware, no evidence of similar behavior in flexible cylinders has been reported earlier. This group consists of two branches and has two local maxima, one described in this work as "typical maximum" and other as global maximum.
  - Group 4 is characterized by a jump in frequency, which corresponds with a peak in the maximum amplitude in the initial branch. This peak is observed even in cylinders from groups 2 and 3.
- In all cases a local maximum amplitude named here "typical maximum", occurs at some point between natural frequency in a vacuum and natural frequency in the working fluid.

Several parameters were tested to classify the different groups. The slope obtained between V_r and Re numbers demonstrates the best results. Ranges corresponding to this slope and respective groups are offered in chapter 4. In addition, using a proposed polynomial fit, the V_r/Re slope can be calculated using L/D and m^* ratios. This allows to predict the maximum amplitude behavior for a given cylinder before performing any time-consuming experiment.

As pointed out in chapter 4, although some researches have proposed that a loss in synchronization between vortex shedding and oscillations is responsible for the distinct

amplitude responses (at least in group 3), the hydrodynamics studied so far in this work has not offered conclusive evidence. However, future work is needed to completely study all the cylinders in the entire synchronization regime. Research is still needed to reveal the exact reasons why there are different types of responses.

Regarding chapter 5 modes 2S, 2P and P+S were observed. There is a clear discordance between the data collected in this work and the original Williamson-Roshko map (developed for forced transverse oscillations). From what can be seen, all groups have different behavior. Also, the areas of the different modes overlap each other. For example, the 2S mode area from group 1 is overlap with the 2S mode area from group 2. But the same area from group 1 is also overlapped with the P+S area from group 2.

This clearly shows that not only the original W-R map is not suitable for all the different cylinders but, also, that even in the same type of cylinders this map is variable depending on the group classification.

Contributions and future work

This work represents an effort to better understand the behavior in the dynamics and hydrodynamics of cantilevered uniform flexible circular cylinders subjected to VIV. Meticulous experimental research with 32 cylinders was performed. Based on experimental results, dynamic atypical behaviors (different from reported in the literature) were observed and classified. Four different groups were presented and the properties of each of its characteristic branches were detailed. The V_r/Re parameter was proposed to predict the maximum amplitude behavior for a given cylinder by knowing only the L/D ratio and ω_{vacuum} before performing experiments through the entire synchronization regime. This can be useful to take advantage of the different behaviors for a specific application. Future work may consider testing the V_r/Re parameter in a real scale experiment to compare results with those presented here. In the Griffin plot data seams to fit the curve, however, the amplitudes for this specific type of cylinders will be underestimated. An even wider study in this type of cylinders is needed to fulfill the Griffin plot and clearly see if there is a specific model that can suite accurate amplitude predictions.

Regarding the hydrodynamic response, a relation between jumps in the vortex shedding modes and the change of branches were observed. Although phenomena correspond, with the information collected in this work, it is not possible to know if these jumps cause the dynamic response, or if the dynamic response causes these mode changes. More experiments on hydrodynamics are needed to answer that question. Vortex shedding modes do not match the Williamson-Roshko map, which is logical considering that it was originally developed for forced transverse oscillations of circular cylinders. Even more, for each group very clear differences are shown. This fact leads to thinking

that for each group found, the type of vortex shedding modes that exist in each branch should be maintained, but probably not where they are in a graph A^*_{max} vs V_r.

Bibliography

[1] M. M. Cicolin and G. R.S. Assi. Experiments with flexible shrouds to reduce the vortex-induced vibration of a cylinder with low mass and damping. *Applied Ocean Research*, 2017.

[2] Lin Ding, Qunfeng Zou, Li Zhang, and Haibo Wang. Research on flow-induced vibration and energy harvesting of three circular cylinders with roughness strips in tandem. *Energies*, 11(11):2977, 2018.

[3] Stéphane Étienne and Dominique Pelletier. The low Reynolds number limit of vortex-induced vibrations. *Journal of Fluids and Structures*, 2012.

[4] A. C. Fernandes, S. Mirzaeisefat, and L. V. Cascão. Fundamental behavior of Vortex Self Induced Vibration (VSIV), 2014.

[5] A. L.C. Fujarra, C. P. Pesce, F. Flemming, and C. H.K. Williamson. Vortex-induced vibration of a flexible cantilever. *Journal of Fluids and Structures*, 2001.

[6] Elizabeth M.H. Garcia and Michael M. Bernitsas. Effect of damping on variable added mass and lift of circular cylinders in vortex-induced vibrations. *Journal of Fluids and Structures*, 80:451–472, jul 2018.

[7] M. Gerardin, D. Rixen, Michel Géradin, and Daniel J. Rixen. *Mechanical Vibrations - Theory and Application to structural Dynamics*. 2015.

[8] R. GOVARDHAN and C. H. K. WILLIAMSON. Modes of vortex formation and frequency response of a freely vibrating cylinder. *Journal of Fluid Mechanics*, 2000.

[9] M. Gürgöze and H. Erol. Dynamic response of a viscously damped cantilever with a viscous end condition. *Journal of Sound and Vibration*, 298(1-2):132–153, nov 2006.

[10] Xiangxi Han, Wei Lin, Dongjiao Wang, Ang Qiu, Zhiqiang Feng, Youhong Tang, and Jiaming Wu. Numerical simulation of super upper branch of a cylindrical structure with a low mass ratio. *Ocean Engineering*, 2018.

[11] Shih Chun Hsieh, Ying Min Low, and Yee Meng Chiew. Flow characteristics around a circular cylinder undergoing vortex-induced vibration in the initial branch. *Ocean Engineering*, 2017.

[12] F. J. Huera-Huarte. On splitter plate coverage for suppression of vortex-induced vibrations of flexible cylinders. *Applied Ocean Research*, 2014.

[13] F. J. Huera-Huarte and M. Gharib. Flow-induced vibrations of a side-by-side arrangement of two flexible circular cylinders. *Journal of Fluids and Structures*, 27(3):354–366, apr 2011.

[14] N. Jauvtis and C. H.K. Williamson. Vortex-induced vibration of a cylinder with two degrees of freedom. *Journal of Fluids and Structures*, 2003.

[15] Shin Woong Kim, Seung Jae Lee, Cheol Young Park, and Donghoon Kang. An experimental study of a circular cylinder's two-degree-of-freedom motion induced by vortex. *International Journal of Naval Architecture and Ocean Engineering*, 8(4):330–343, jul 2016.

[16] J. H. Lee and M. M. Bernitsas. High-damping, high-Reynolds VIV tests for energy harnessing using the VIVACE converter. *Ocean Engineering*, 2011.

[17] Shuai Meng, Hiroyuki Kajiwara, and Weijing Zhang. Internal flow effect on the cross-flow vortex-induced vibration of a cantilevered pipe discharging fluid. *Ocean Engineering*, 137:120–128, 2017.

[18] Shuai Meng, Xiaoqing Zhang, Chidong Che, and Weijing Zhang. Cross-flow vortex-induced vibration of a flexible riser transporting an internal flow from subcritical to supercritical. *Ocean Engineering*, 139:74–84, 2017.

[19] Hidemi Mutsuda, Yoshikazu Tanaka, Rupesh Patel, and Yasuaki Doi. Harvesting flow-induced vibration using a highly flexible piezoelectric energy device. *Applied Ocean Research*, 2017.

[20] N. Navrose and Sanjay Mittal. Lock-in in vortex-induced vibration. *Journal of Fluid Mechanics*, 794:565–594, may 2016.

[21] F. Oviedo-Tolentino, F. G. Pérez-Gutiérrez, R. Romero-Méndez, and A. Hernández-Guerrero. Vortex-induced vibration of a bottom fixed flexible circular beam. *Ocean Engineering*, 2014.

[22] H. J. Pain. *The Physics of Vibrations and Waves: Sixth Edition*. 2005.

[23] Feifei Pan, Zhike Xu, Long Jin, Peng Pan, and Xiu Gao. Designed Simulation and Experiment of a Piezoelectric Energy Harvesting System Based on Vortex-Induced Vibration. *IEEE Transactions on Industry Applications*, 2017.

[24] Singiresu S. Rao. Mechanical Vibrations Fifth Edition in SI Units. *Mechanical Vibrations*, 2011.

[25] S. Graham Kelly. *Mechanical Vibrations: Theory and Applications, SI*. 2014.

[26] Banafsheh Seyed-Aghazadeh and Yahya Modarres-Sadeghi. Reconstructing the vortex-induced-vibration response of flexible cylinders using limited localized measurement points. *Journal of Fluids and Structures*, 2016.

[27] Ahmed A Shabana. *Theory of vibration - An introduction*. 2014.

[28] Atul Kumar Soti, Jisheng Zhao, Mark C. Thompson, John Sheridan, and Rajneesh Bhardwaj. Damping effects on vortex-induced vibration of a circular cylinder and implications for power extraction. *Journal of Fluids and Structures*, 2018.

[29] William Thielicke. *The flapping flight of birds: Analysis and application*. PhD thesis, University of Groningen, 2014.

[30] William Thielicke and Eize Stamhuis. Pivlab–towards user-friendly, affordable and accurate digital particle image velocimetry in matlab. *Journal of open research software*, 2(1), 2014.

[31] J. Kim Vandiver. Damping Parameters for flow-induced vibration. *Journal of Fluids and Structures*, 2012.

[32] D. Vicente-Ludlam, A. Barrero-Gil, and A. Velazquez. Flow-induced vibration control of a circular cylinder using rotational oscillation feedback. *Journal of Fluid Mechanics*, 847:93–118, jul 2018.

[33] X. K. Wang, C. Wang, Y. L. Li, and S. K. Tan. Flow patterns of a low mass-damping cylinder undergoing vortex-induced vibration: Transition from initial branch and upper branch. *Applied Ocean Research*, 2017.

[34] C. H.K. Williamson and R. Govardhan. A brief review of recent results in vortex-induced vibrations. *Journal of Wind Engineering and Industrial Aerodynamics*, 2008.

[35] Jie Wu, Halvor Lie, Carl M. Larsen, Stergios Liapis, and Rolf Baarholm. Vortex-induced vibration of a flexible cylinder: Interaction of the in-line and cross-flow responses. *Journal of Fluids and Structures*, 2016.

[36] Wude Xie, Xifeng Gao, Enhao Wang, Wanhai Xu, and Yuchuan Bai. An investigation of the nonlinear dynamic response of a flexible pipe undergoing vortex-induced vibrations and conveying internal fluid with variable-density. *Ocean Engineering*, 183:453–468, jul 2019.

[37] Wanhai Xu, Yexuan Ma, Ankang Cheng, and Hao Yuan. Experimental investigation on multi-mode flow-induced vibrations of two long flexible cylinders in a tandem arrangement. *International Journal of Mechanical Sciences*, 135:261–278, jan 2018.

[38] Wanhai Xu, Wenqi Qin, and Xifeng Gao. Experimental Study on Streamwise Vortex-Induced Vibration of a Flexible, Slender Cylinder. *Applied Sciences*, 2018.

[39] Wanhai Xu, Shuhai Zhang, Bin Liu, Enhao Wang, and Yin Bai. An experimental study on flow-induced vibration of three and four side-by-side long flexible cylinders. *Ocean Engineering*, 2018.

[40] C. T. Yamamoto, J. R. Meneghini, F. Saltara, R. A. Fregonesi, and J. A. Ferrari. Numerical simulations of vortex-induced vibration on flexible cylinders. *Journal of Fluids and Structures*, 19(4):467–489, 2004.

[41] W. Yao and R. K. Jaiman. Model reduction and mechanism for the vortex-induced vibrations of bluff bodies. *Journal of Fluid Mechanics*, 827:357–393, sep 2017.

[42] Kintak Raymond Yu, Alexander Hay, Dominique Pelletier, and Stéphane Étienne. Two degrees of freedom vortex-induced vibration responses with zero mass and damping at low Reynolds number. *Journal of Fluids and Structures*, 83:218–237, 2018.

[43] Weiwei Zhang, Xintao Li, Zhengyin Ye, and Yuewen Jiang. Mechanism of frequency lock-in in vortex-induced vibrations at low Reynolds numbers. *Journal of Fluid Mechanics*, 783:72–102, oct 2015.

[44] Jinchao Zhao, Hang Zhang, Fan Su, and Zhongjun Yin. A novel model of piezoelectric- electromagnetic hybrid energy harvester based on vortex-induced vibration. In *Proceedings of 2017 International Conference on Green Energy and Applications, ICGEA 2017*, 2017.

Appendix A

Stiffness of the cylinder (k)

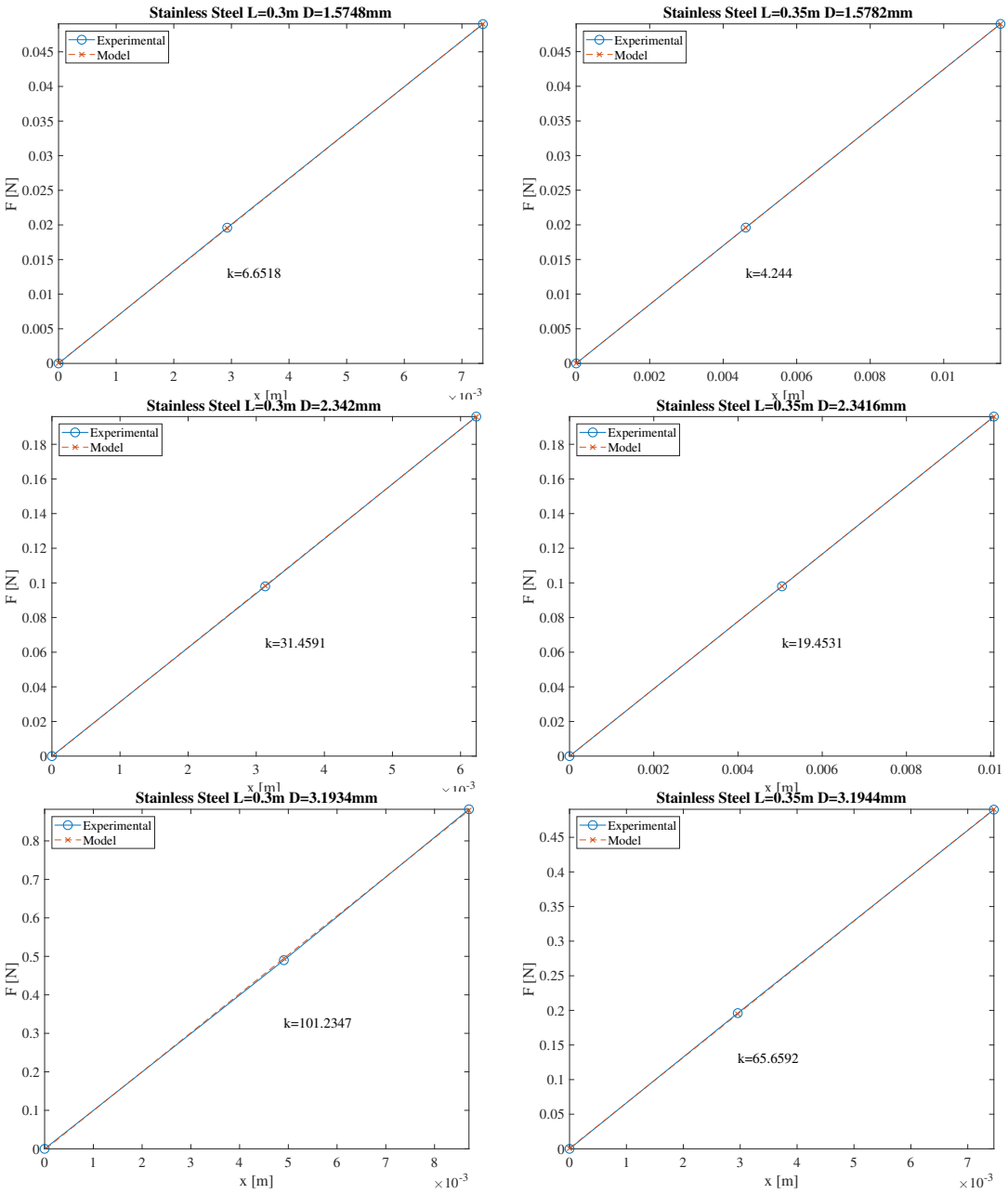

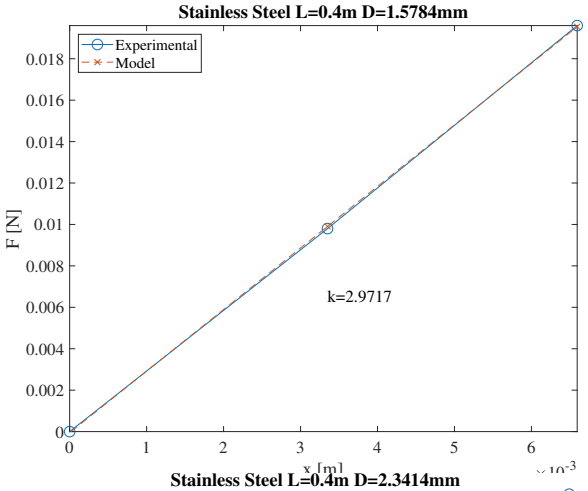
Stainless Steel L=0.4m D=1.5784mm
Experimental
Model
k=2.9717
F [N]
x [m]

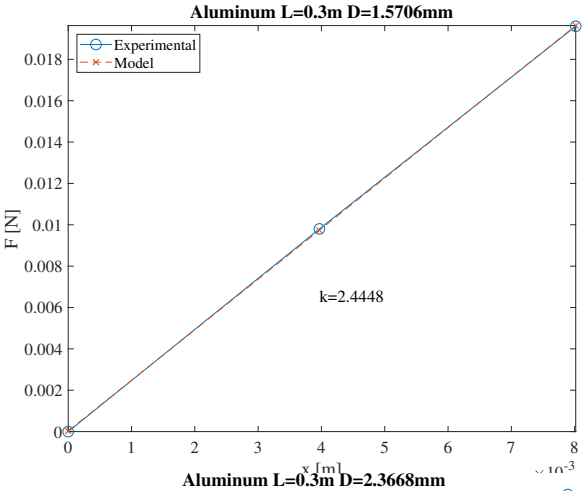
Aluminum L=0.3m D=1.5706mm
Experimental
Model
k=2.4448
F [N]
x [m]

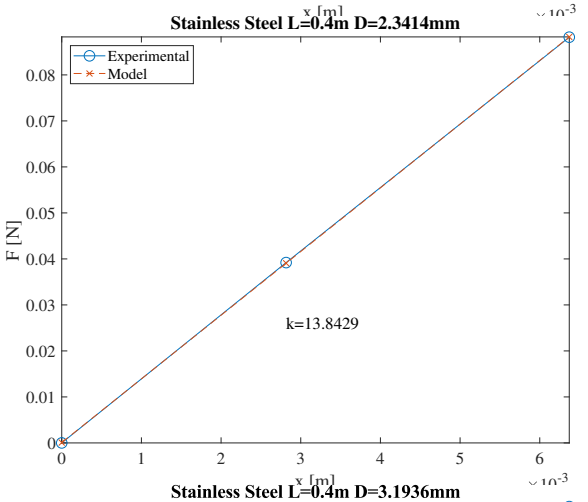
Stainless Steel L=0.4m D=2.3414mm
Experimental
Model
k=13.8429
F [N]
x [m]

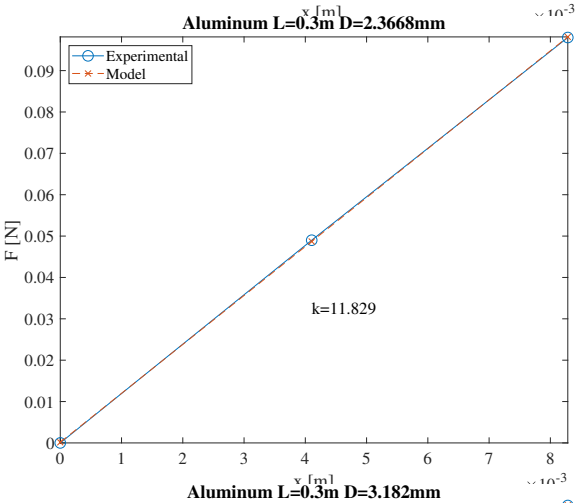
Aluminum L=0.3m D=2.3668mm
Experimental
Model
k=11.829
F [N]
x [m]

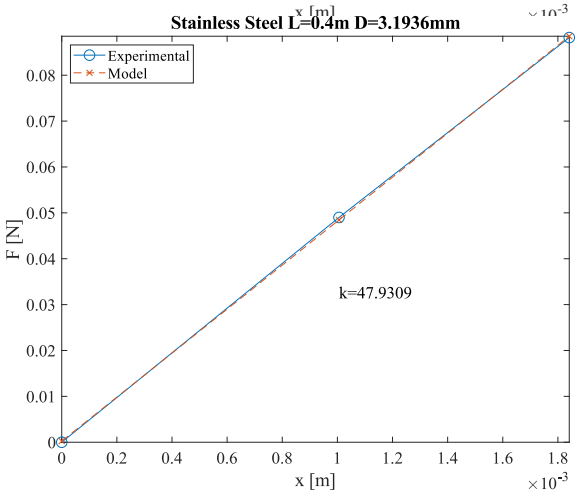
Stainless Steel L=0.4m D=3.1936mm
Experimental
Model
k=47.9309
F [N]
x [m]

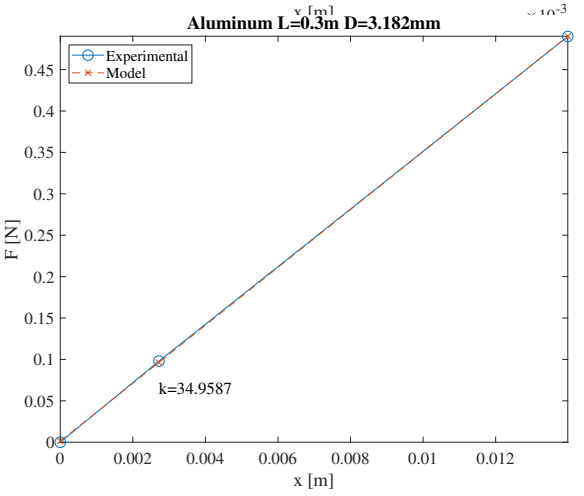
Aluminum L=0.3m D=3.182mm
Experimental
Model
k=34.9587
F [N]
x [m]

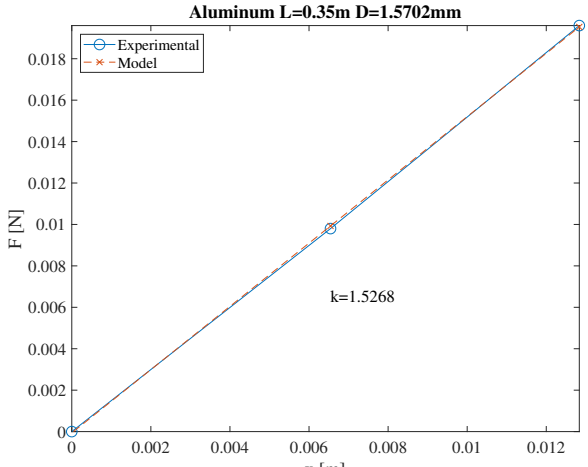
Aluminum L=0.35m D=1.5702mm
Experimental
Model
k=1.5268
F [N]
x [m]

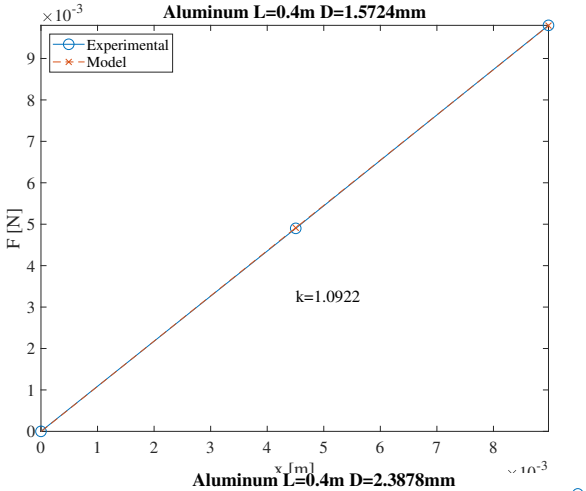
Aluminum L=0.4m D=1.5724mm
Experimental
Model
k=1.0922
F [N]
x [m]

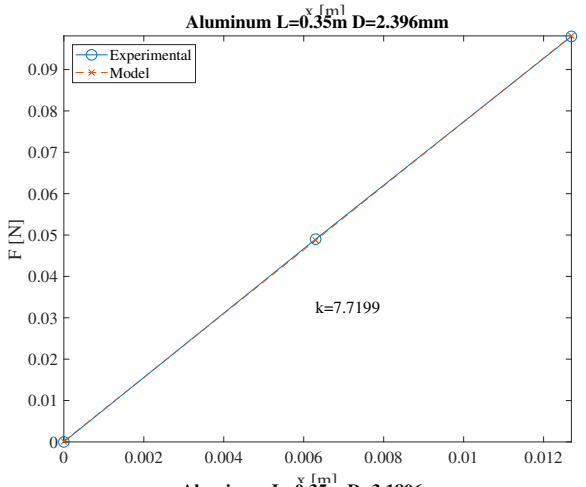
Aluminum L=0.35m D=2.396mm
Experimental
Model
k=7.7199
F [N]
x [m]

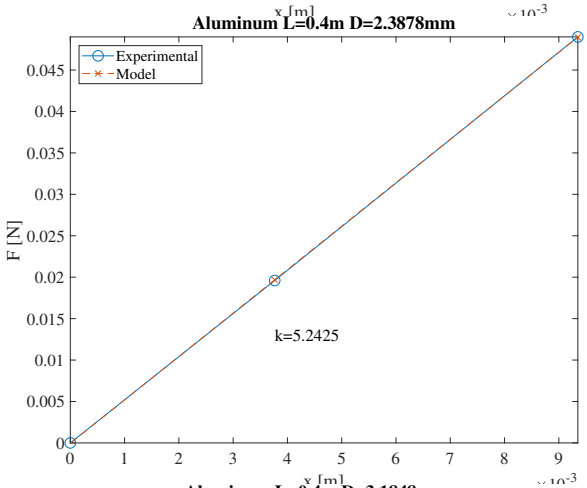
Aluminum L=0.4m D=2.3878mm
Experimental
Model
k=5.2425
F [N]
x [m]

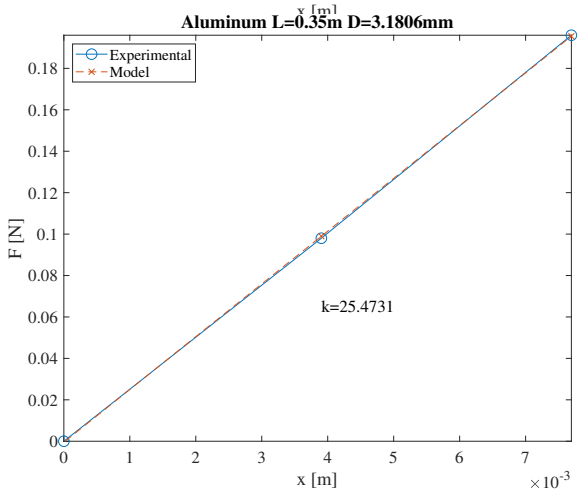
Aluminum L=0.35m D=3.1806mm
Experimental
Model
k=25.4731
F [N]
x [m]

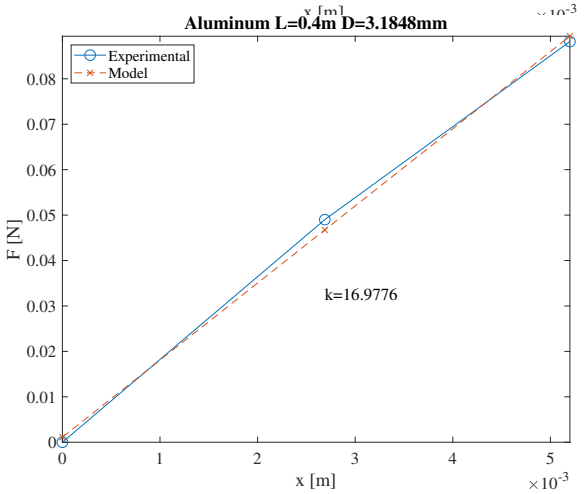
Aluminum L=0.4m D=3.1848mm
Experimental
Model
k=16.9776
F [N]
x [m]

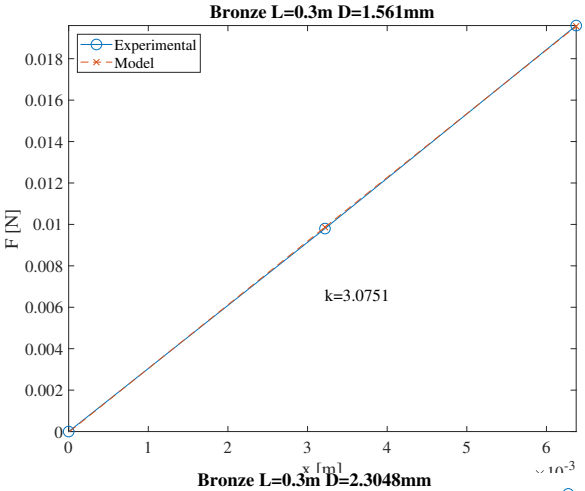
Bronze L=0.3m D=1.561mm
Experimental
Model
k=3.0751
F [N]
x [m]
×10^-3

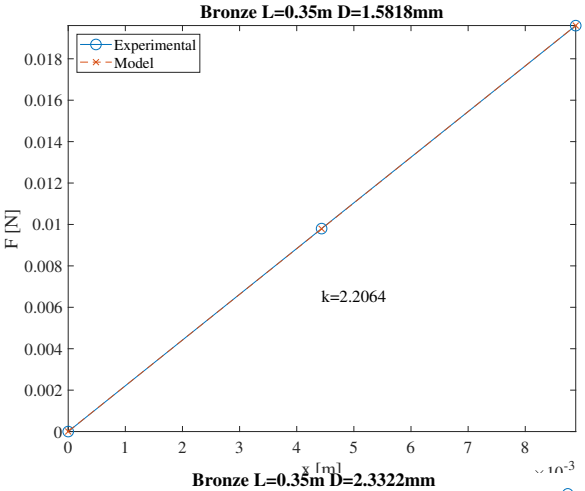
Bronze L=0.35m D=1.5818mm
Experimental
Model
k=2.2064
F [N]
x [m]
×10^-3

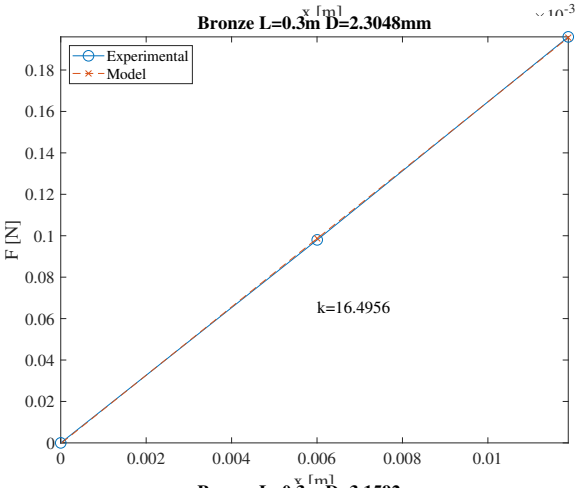
Bronze L=0.3m D=2.3048mm
Experimental
Model
k=16.4956
F [N]
x [m]

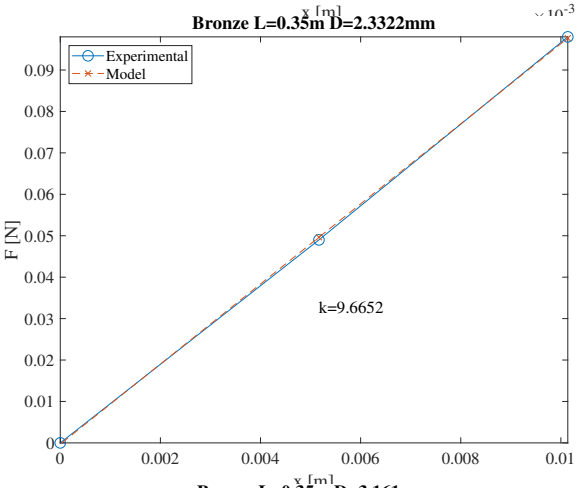
Bronze L=0.35m D=2.3322mm
Experimental
Model
k=9.6652
F [N]
x [m]

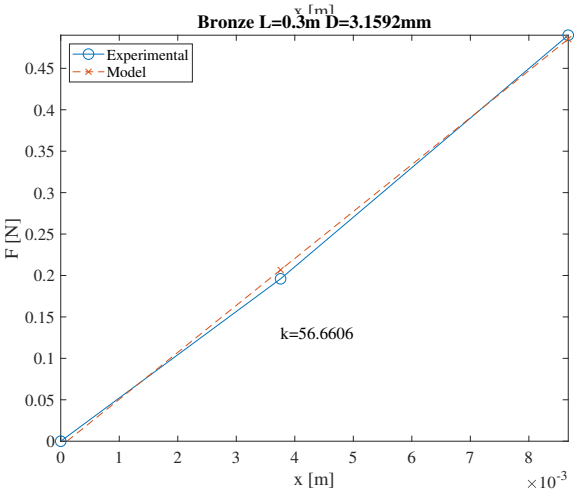
Bronze L=0.3m D=3.1592mm
Experimental
Model
k=56.6606
F [N]
x [m]
×10^-3

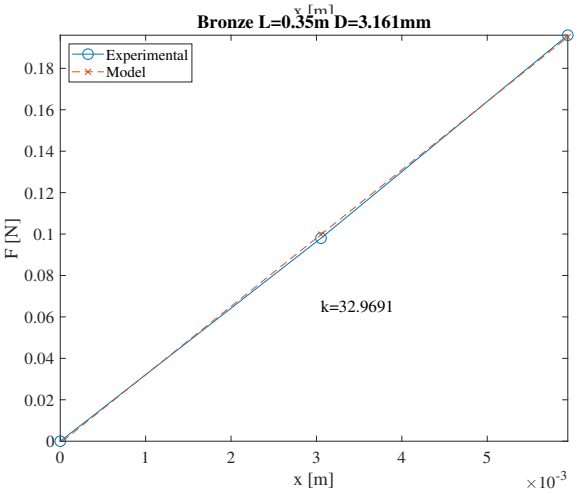
Bronze L=0.35m D=3.161mm
Experimental
Model
k=32.9691
F [N]
x [m]
×10^-3

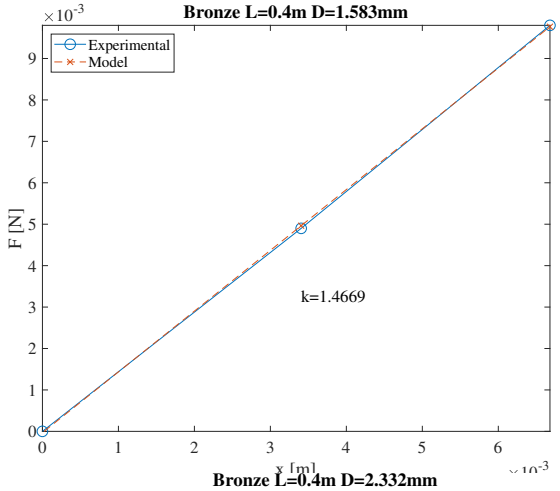
Bronze L=0.4m D=1.583mm
Experimental
Model
k=1.4669
F [N]
x [m]

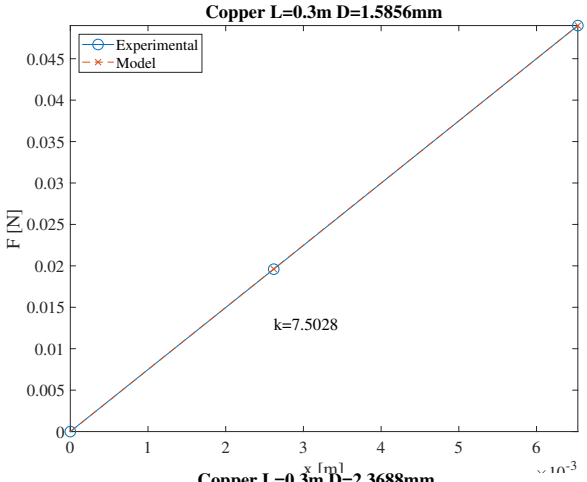
Copper L=0.3m D=1.5856mm
Experimental
Model
k=7.5028
F [N]
x [m]

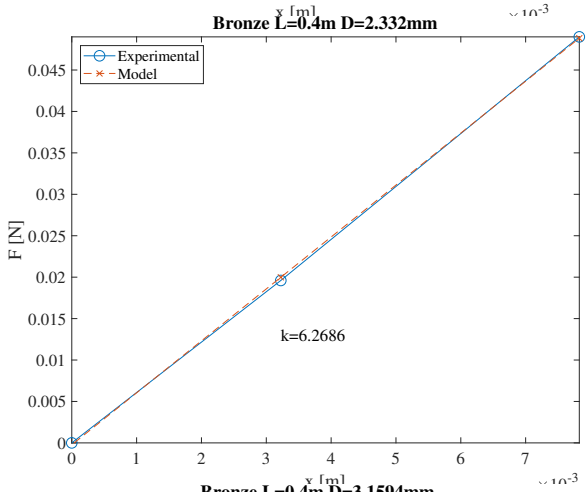
Bronze L=0.4m D=2.332mm
Experimental
Model
k=6.2686
F [N]
x [m]

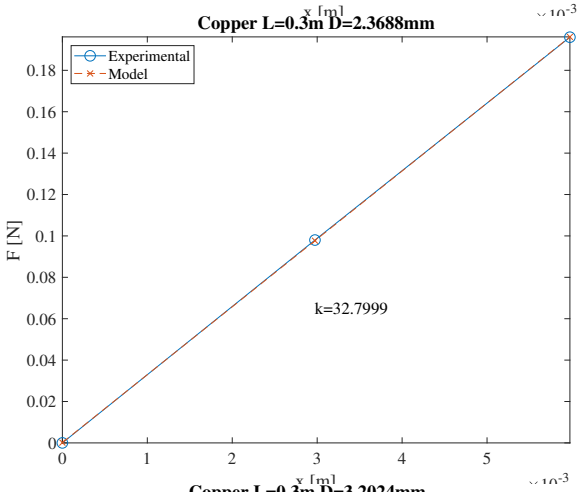
Copper L=0.3m D=2.3688mm
Experimental
Model
k=32.7999
F [N]
x [m]

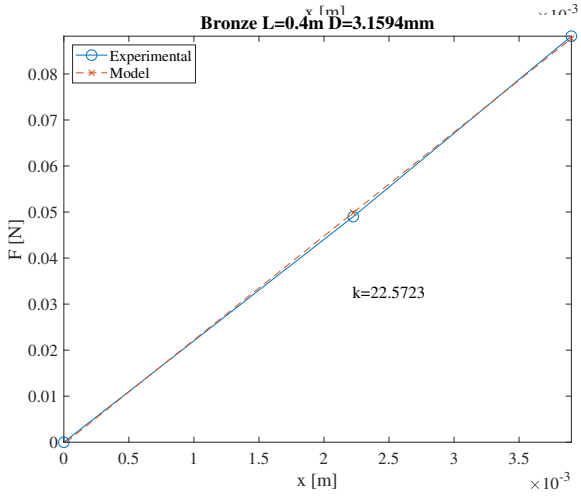
Bronze L=0.4m D=3.1594mm
Experimental
Model
k=22.5723
F [N]
x [m]

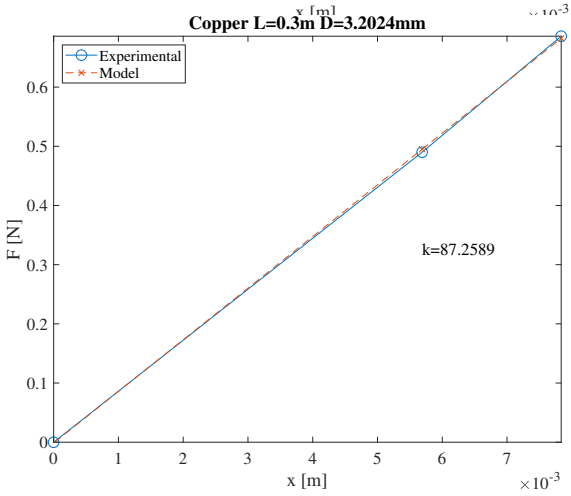
Copper L=0.3m D=3.2024mm
Experimental
Model
k=87.2589
F [N]
x [m]

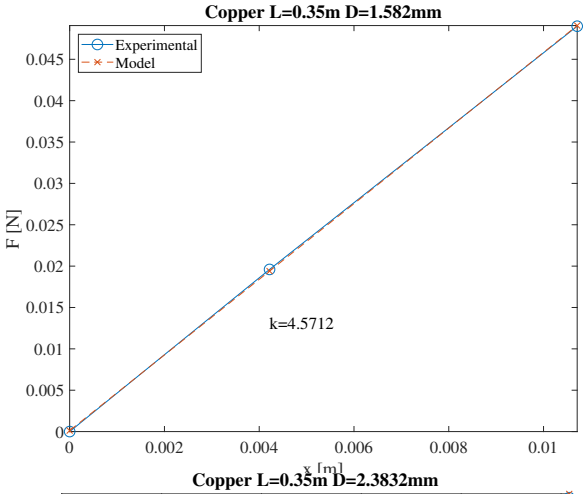
Copper L=0.35m D=1.582mm
Experimental
Model
F [N]
x [m]
k=4.5712

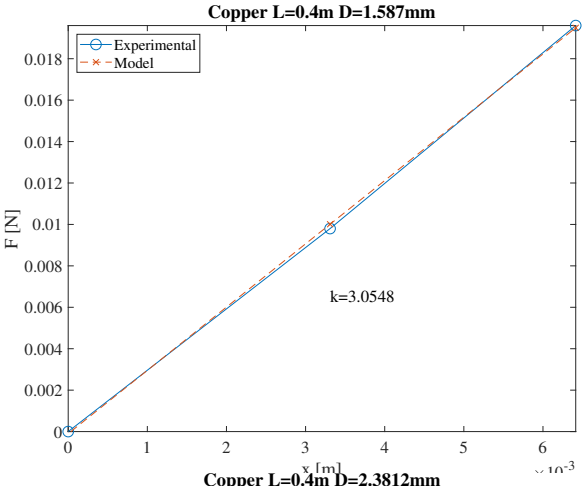
Copper L=0.4m D=1.587mm
Experimental
Model
F [N]
x [m]
k=3.0548

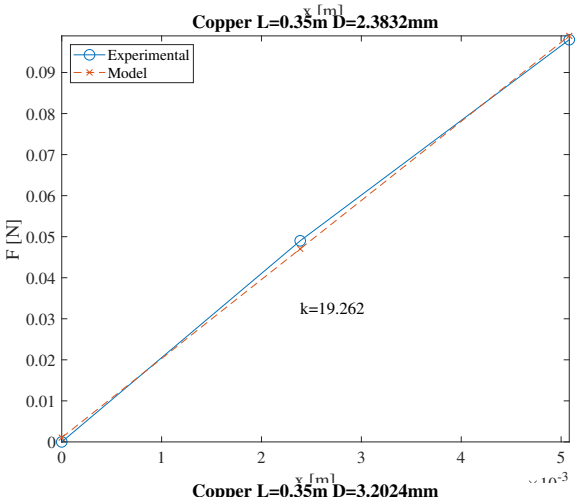
Copper L=0.35m D=2.3832mm
Experimental
Model
F [N]
x [m]
k=19.262

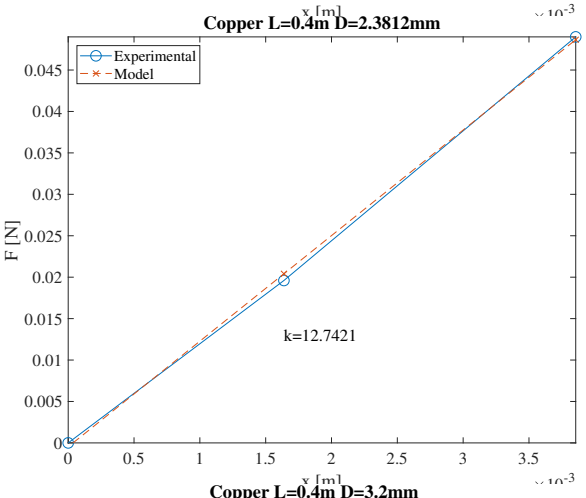
Copper L=0.4m D=2.3812mm
Experimental
Model
F [N]
x [m]
k=12.7421

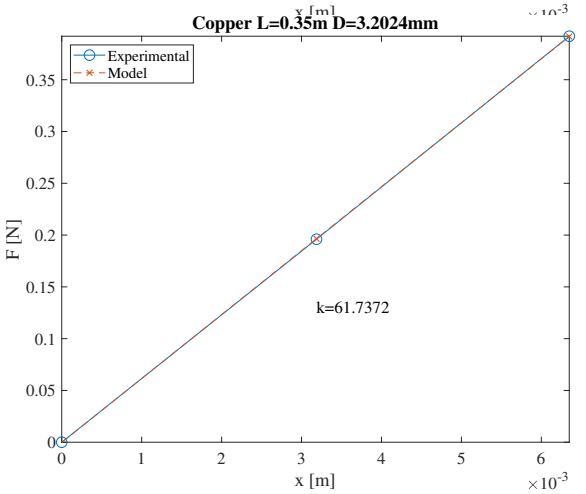
Copper L=0.35m D=3.2024mm
Experimental
Model
F [N]
x [m]
k=61.7372

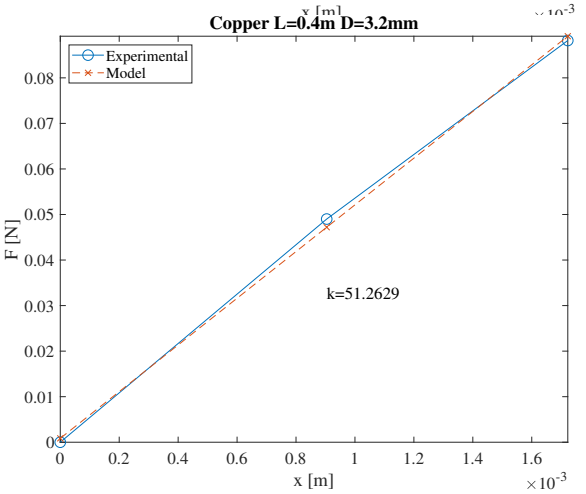
Copper L=0.4m D=3.2mm
Experimental
Model
F [N]
x [m]
k=51.2629

Appendix B

Viscous damping in air (ζ)

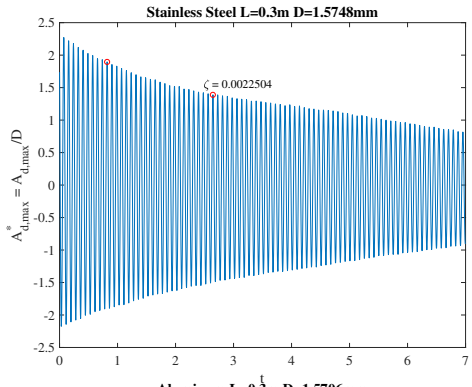

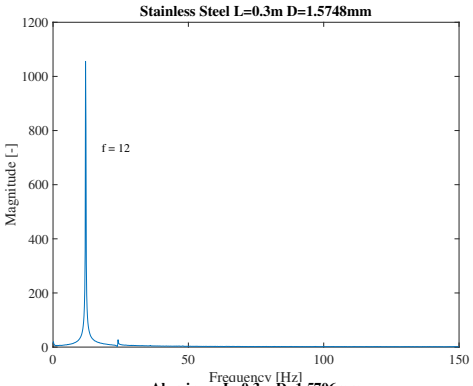

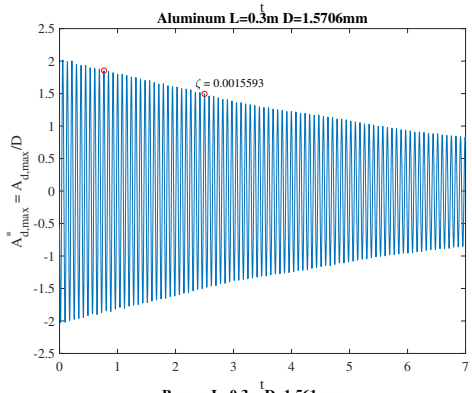

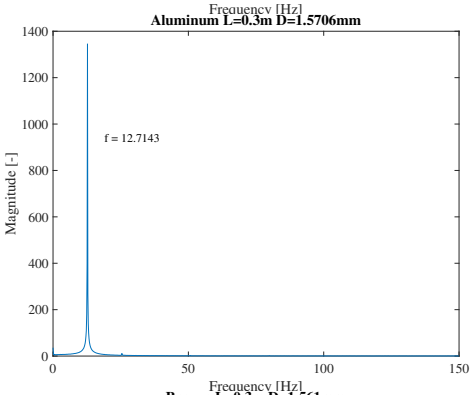

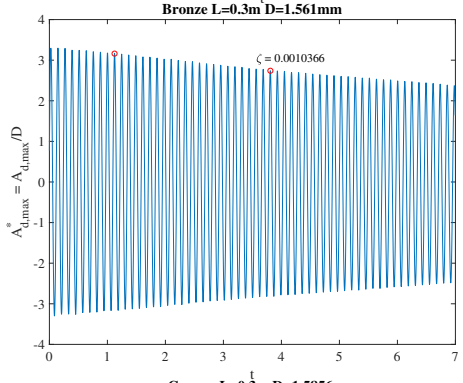

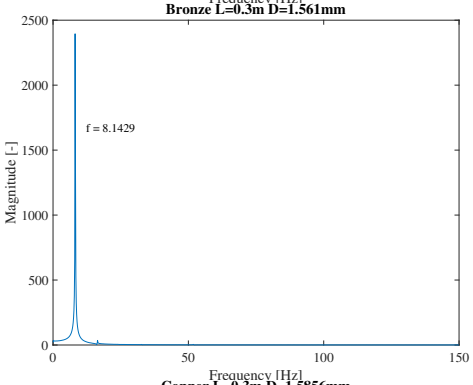

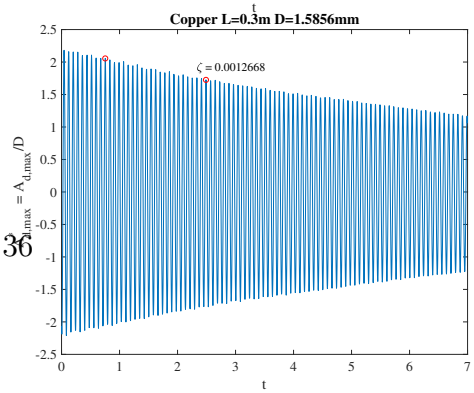

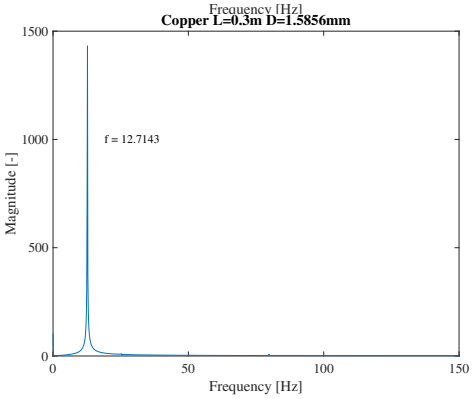

Path | Frequency

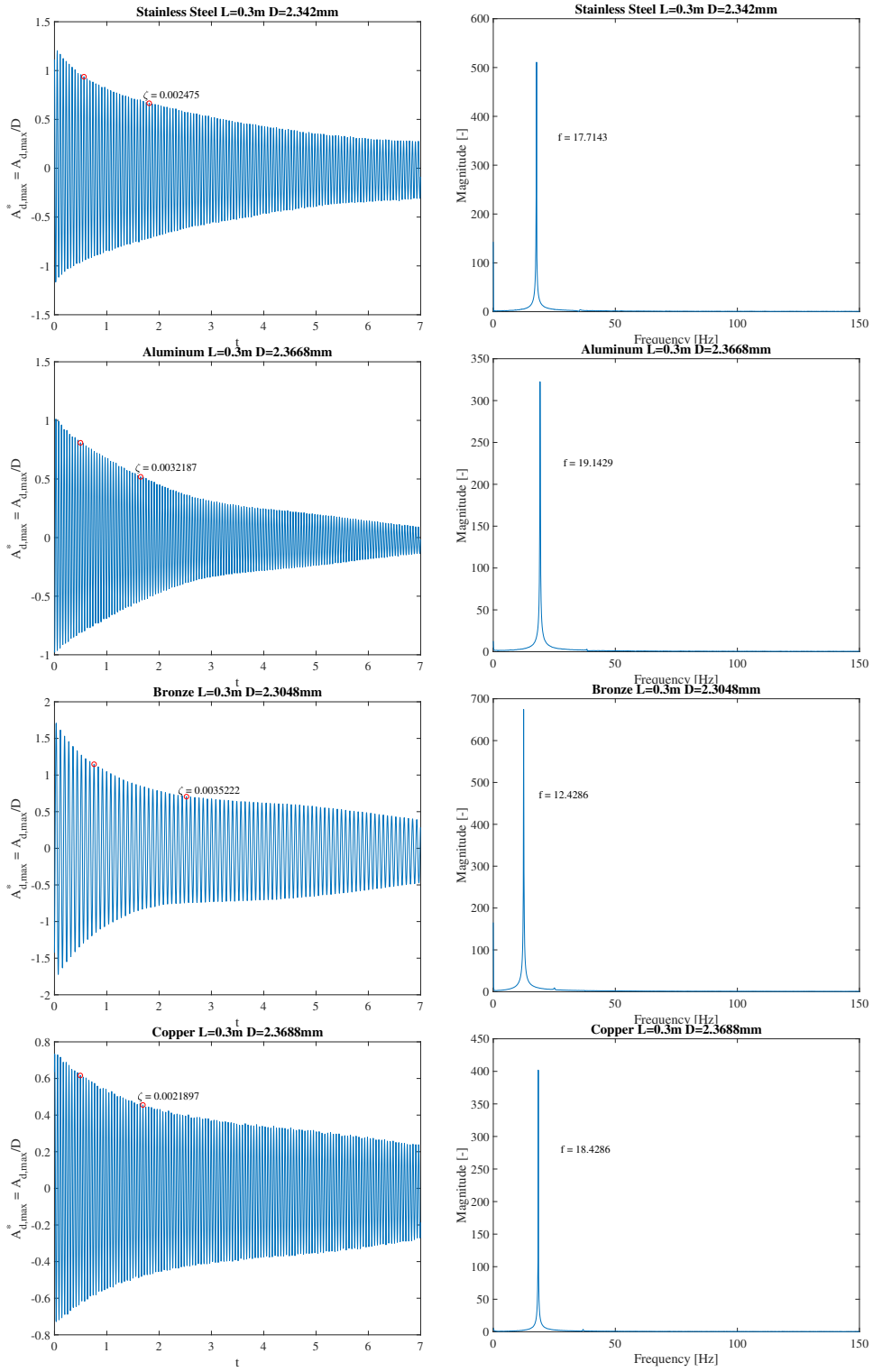

Path

Frequency

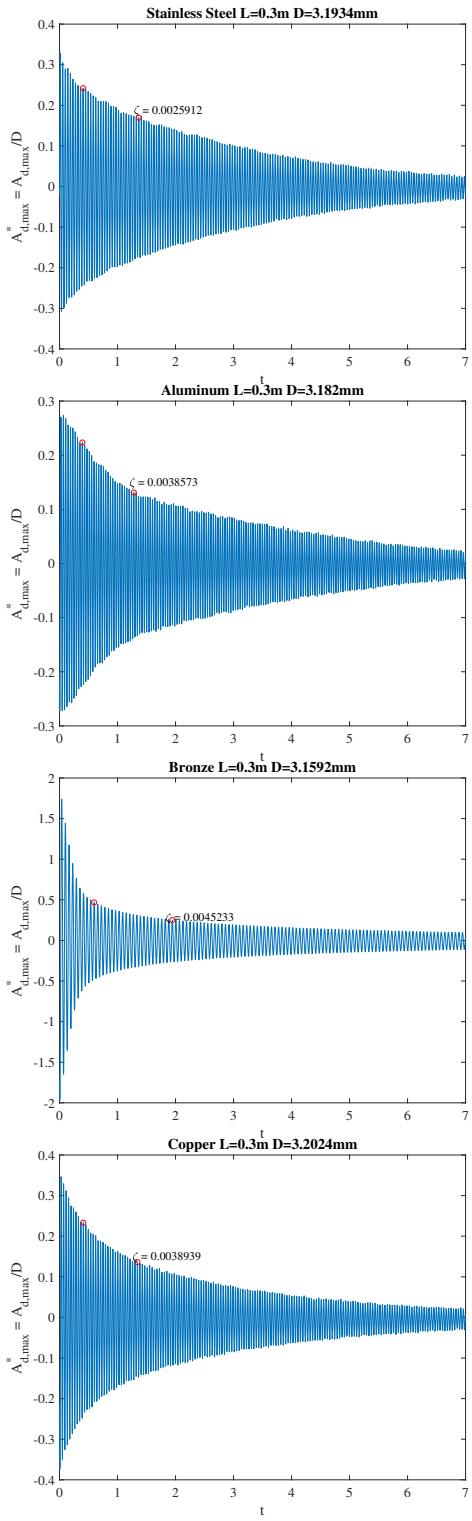

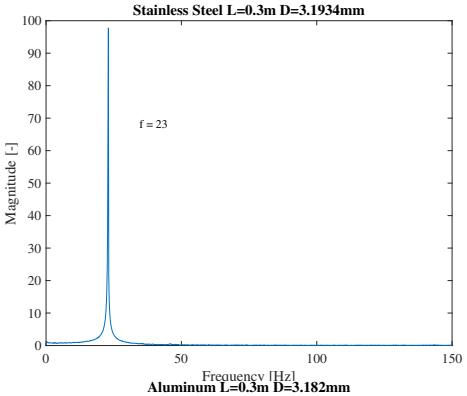

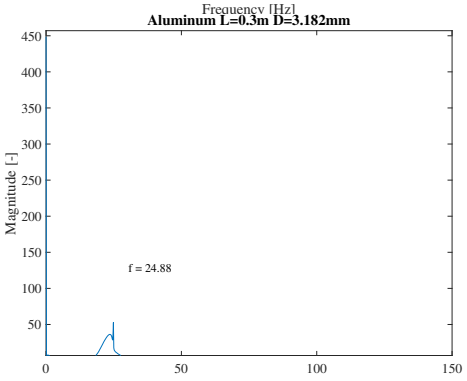

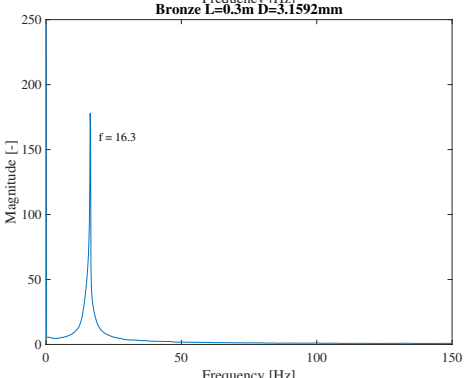

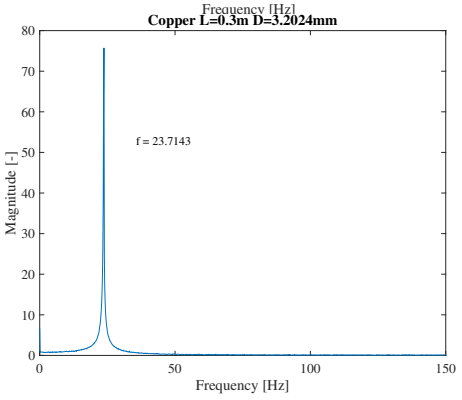

Path

Frequency

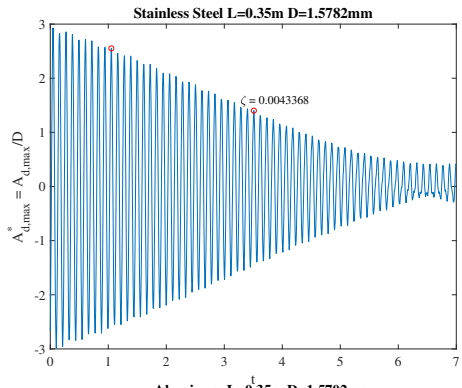

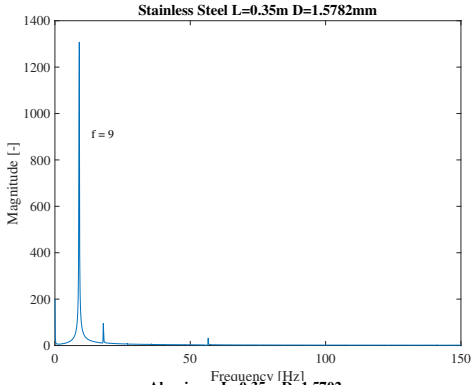

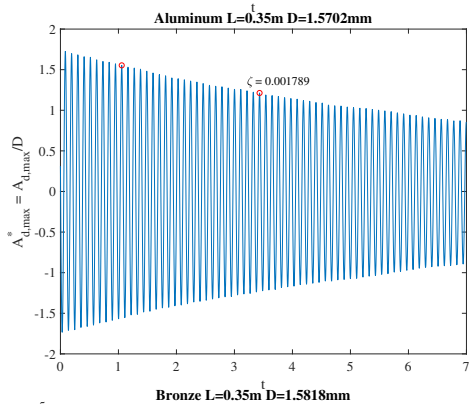

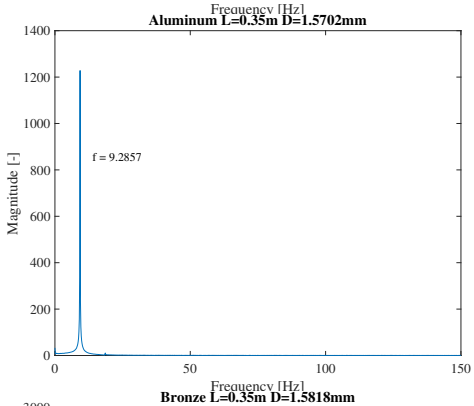

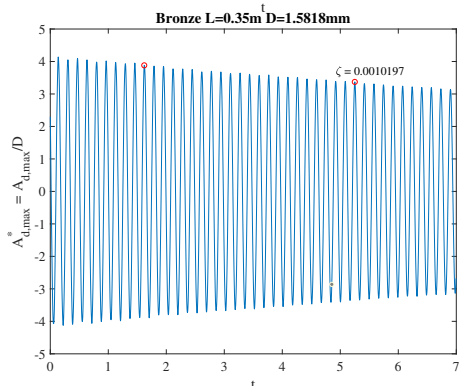

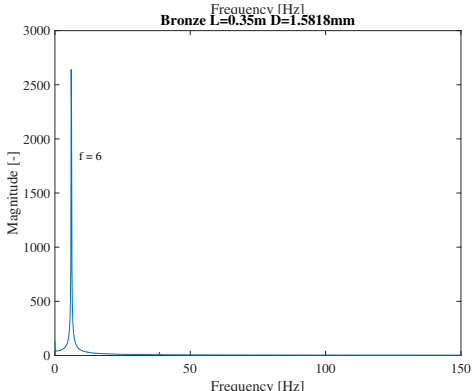

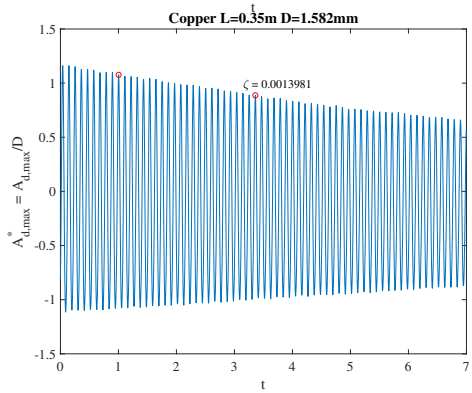

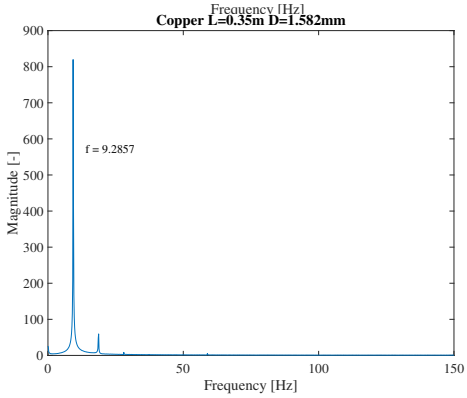

Path

Frequency

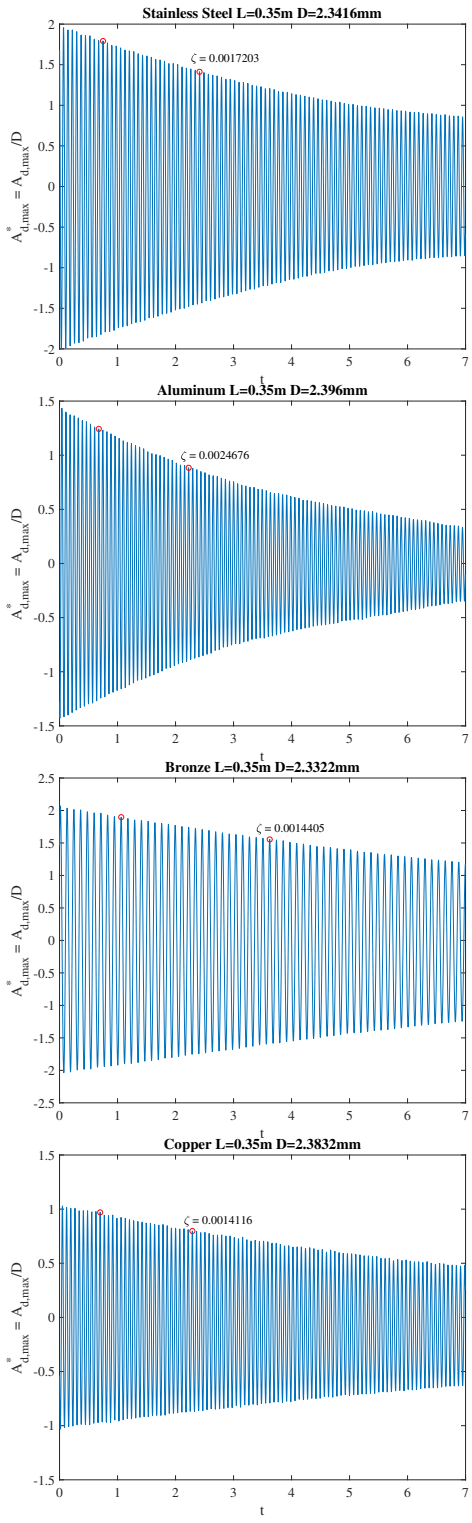

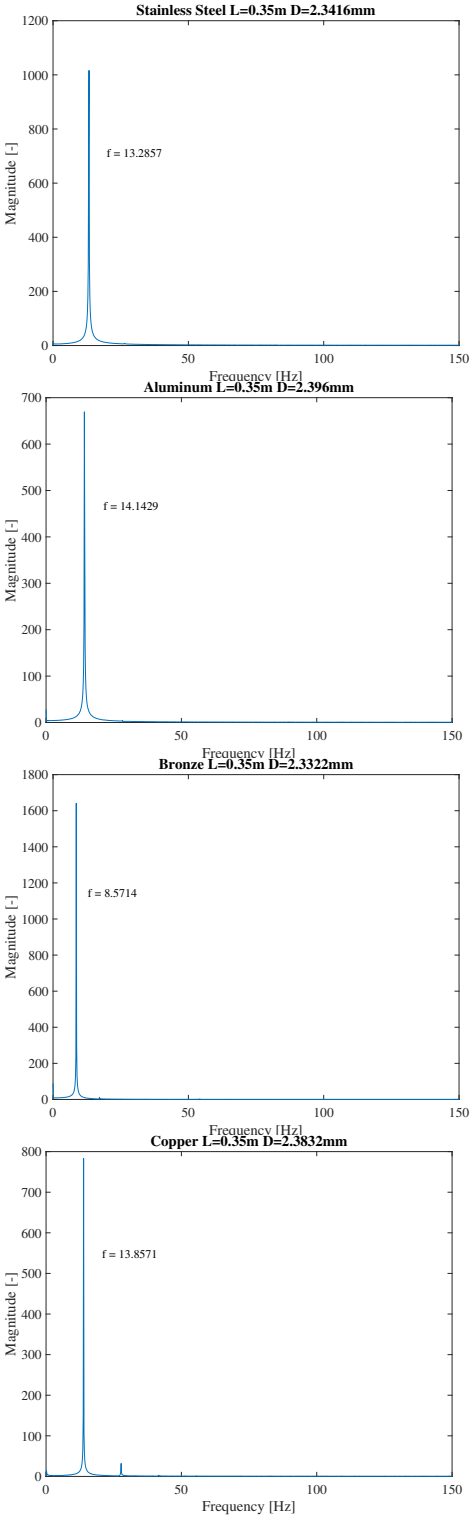

Path

Frequency

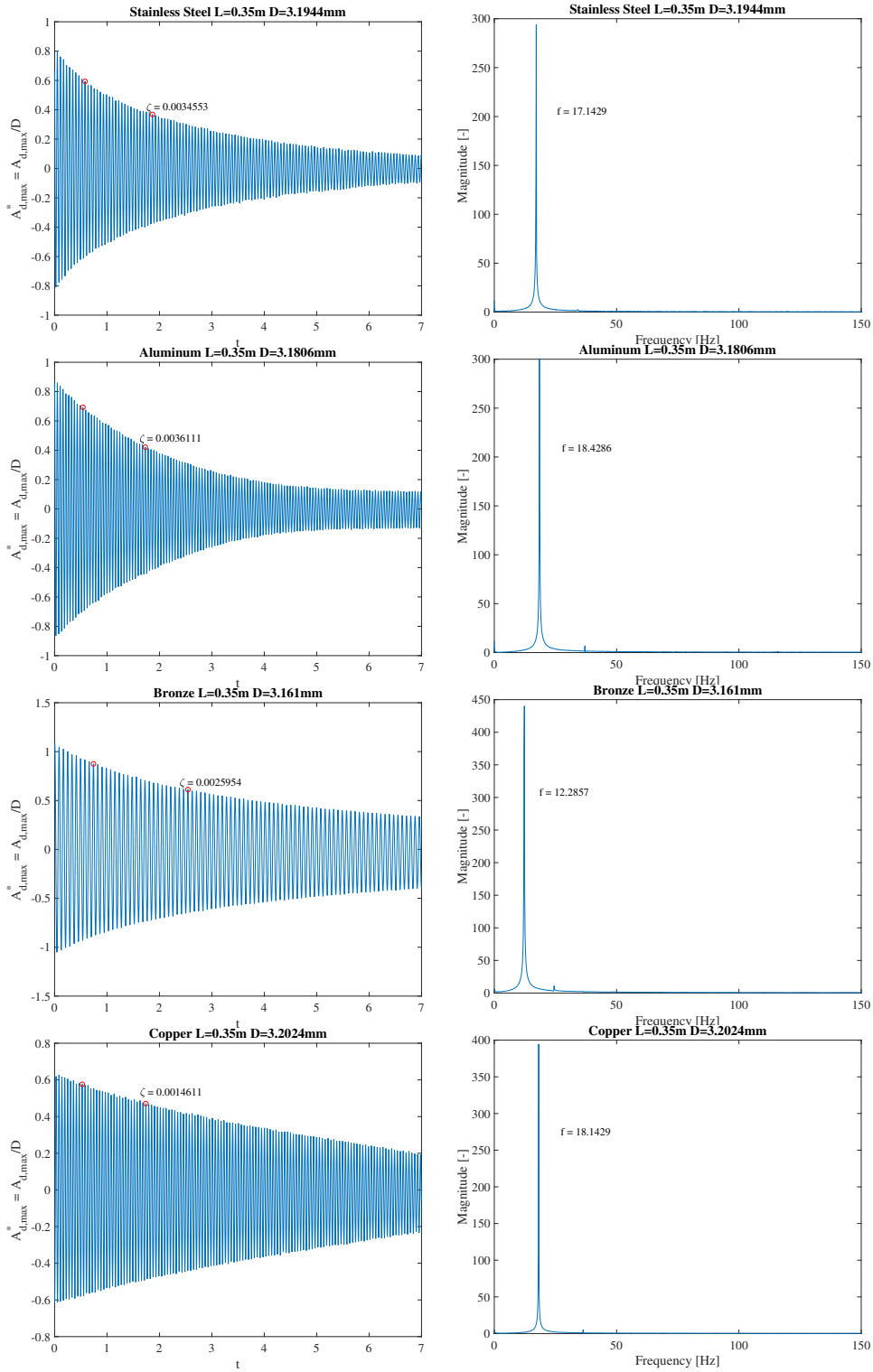

Path

Frequency

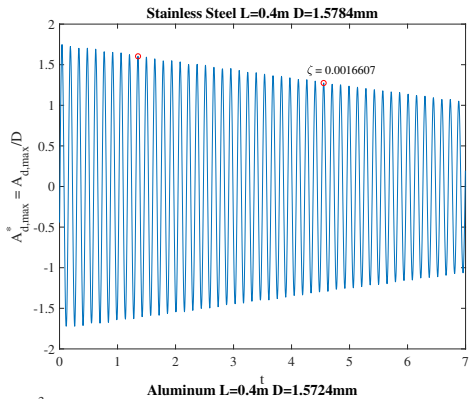

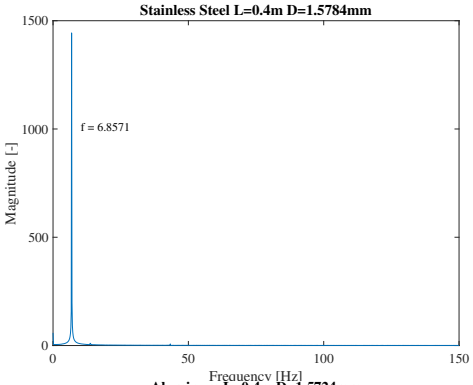

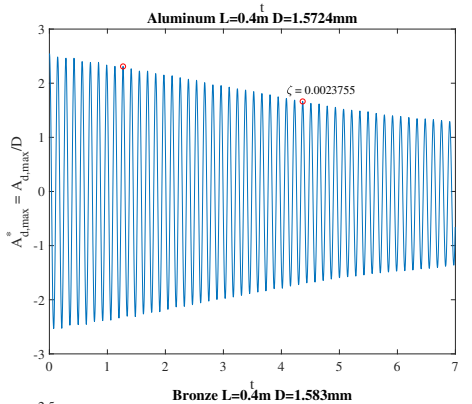

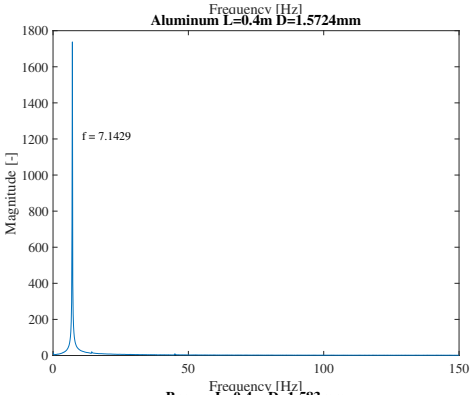

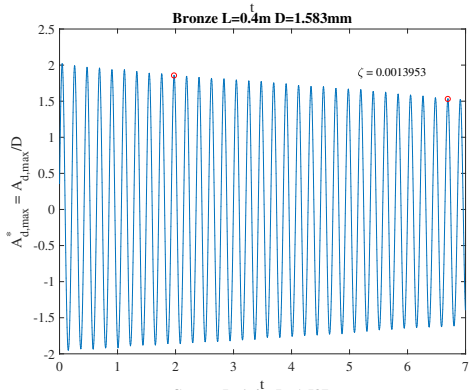

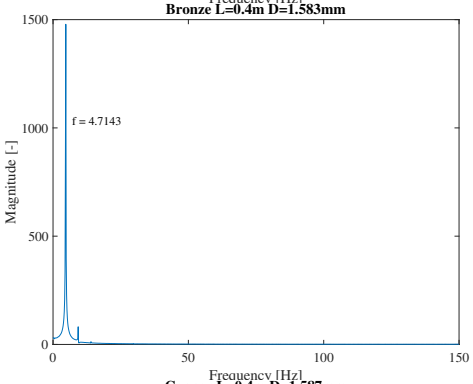

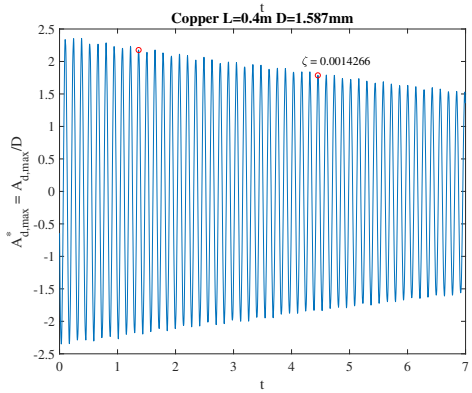

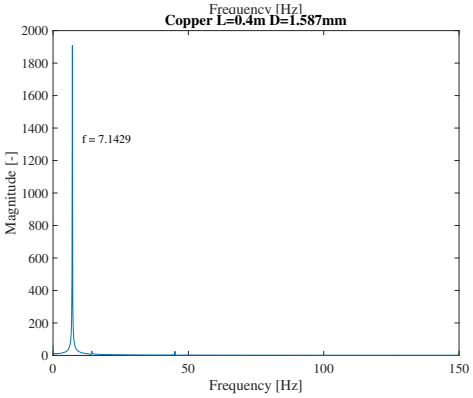

Path | Frequency

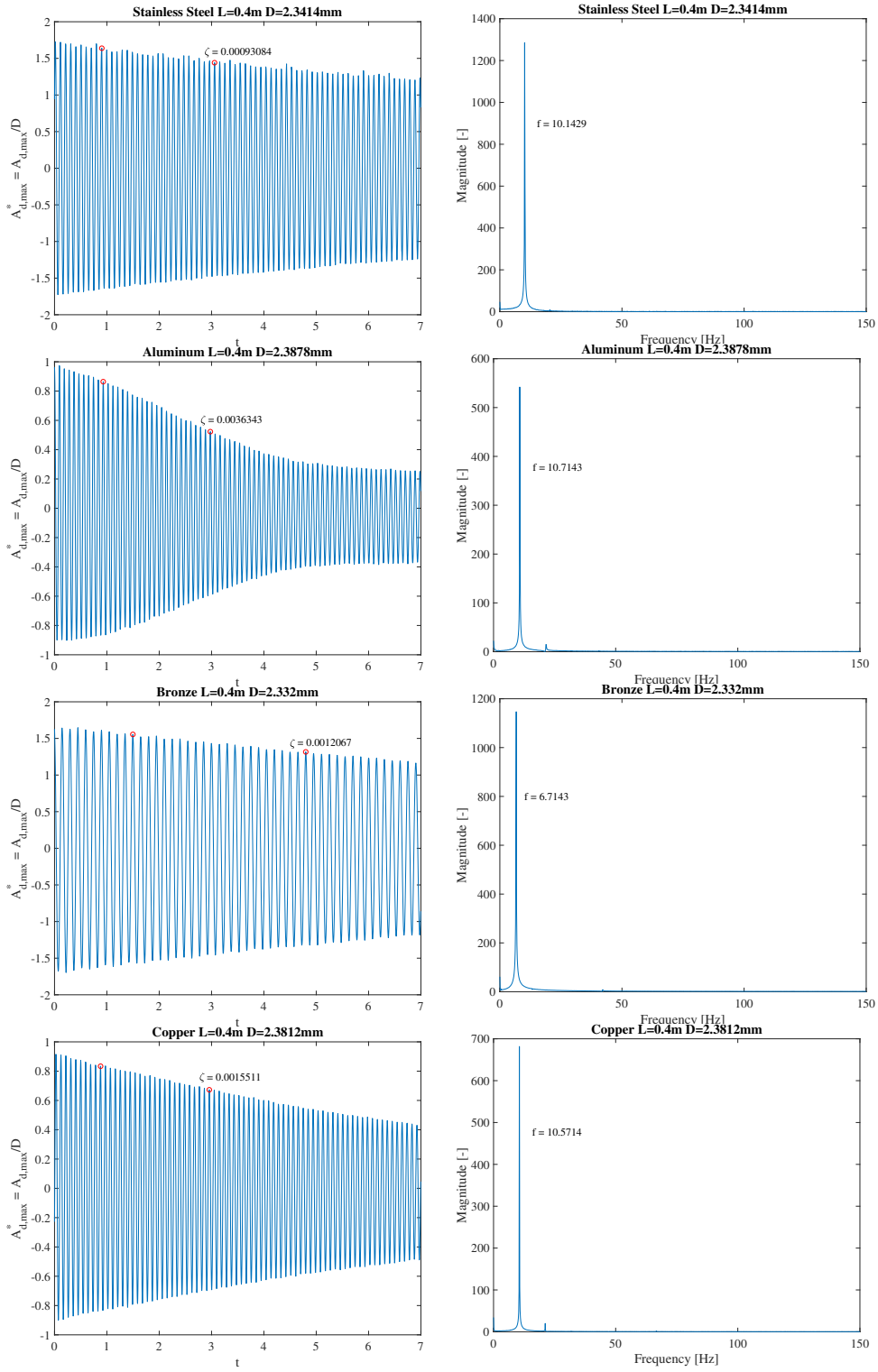

Path

Frequency

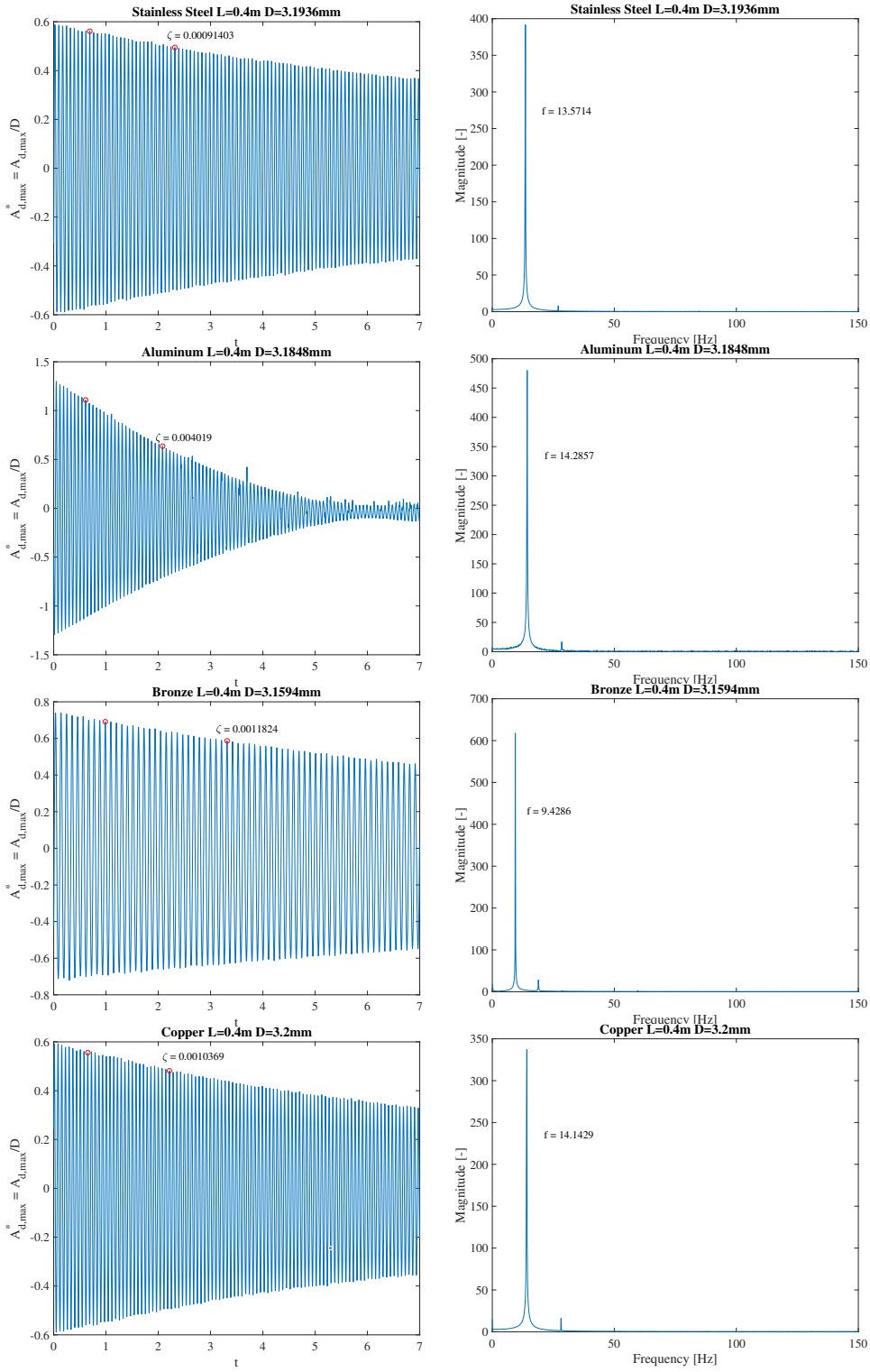

Appendix C

Viscous damping in water (ζ)

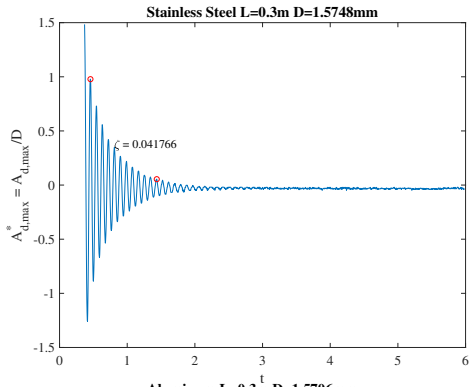

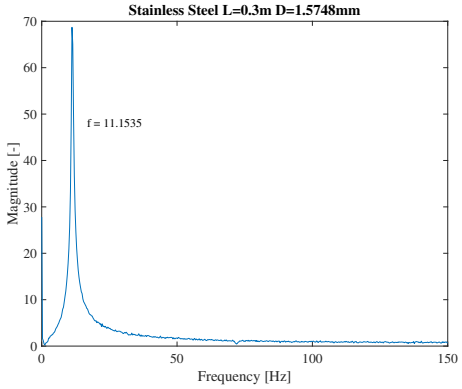

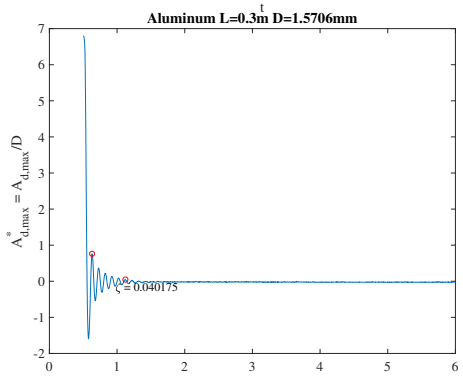

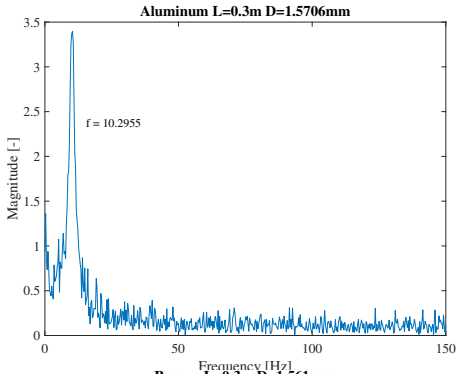

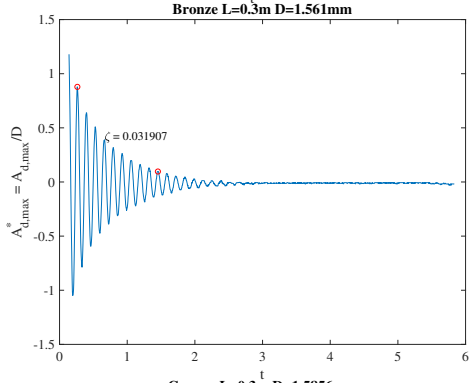

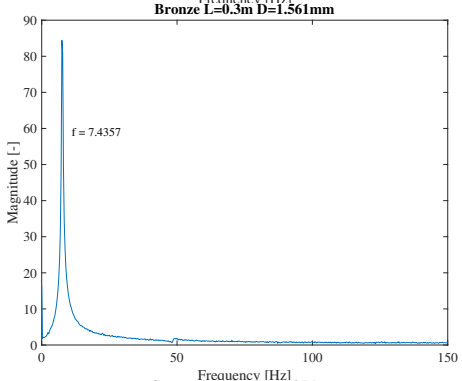

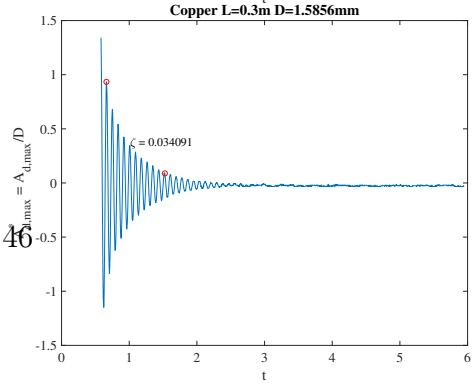

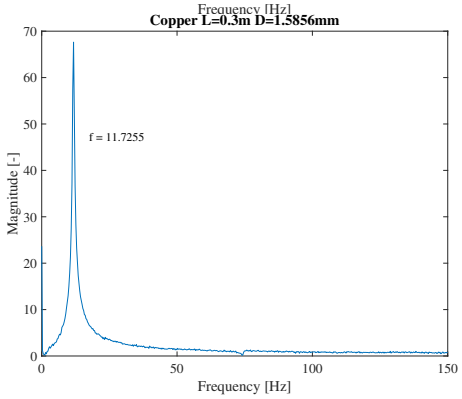

Path | Frequency

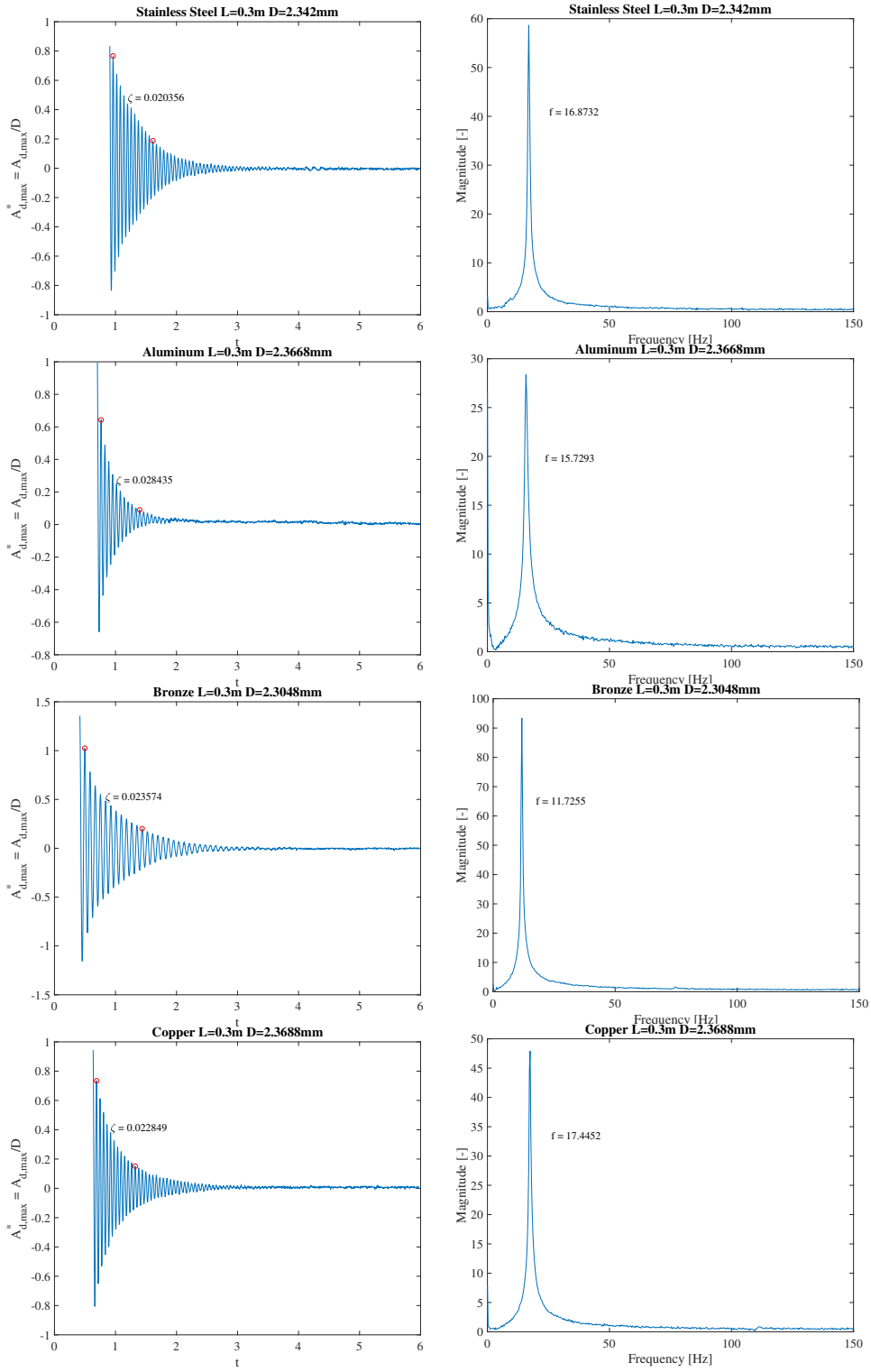

Path

Frequency

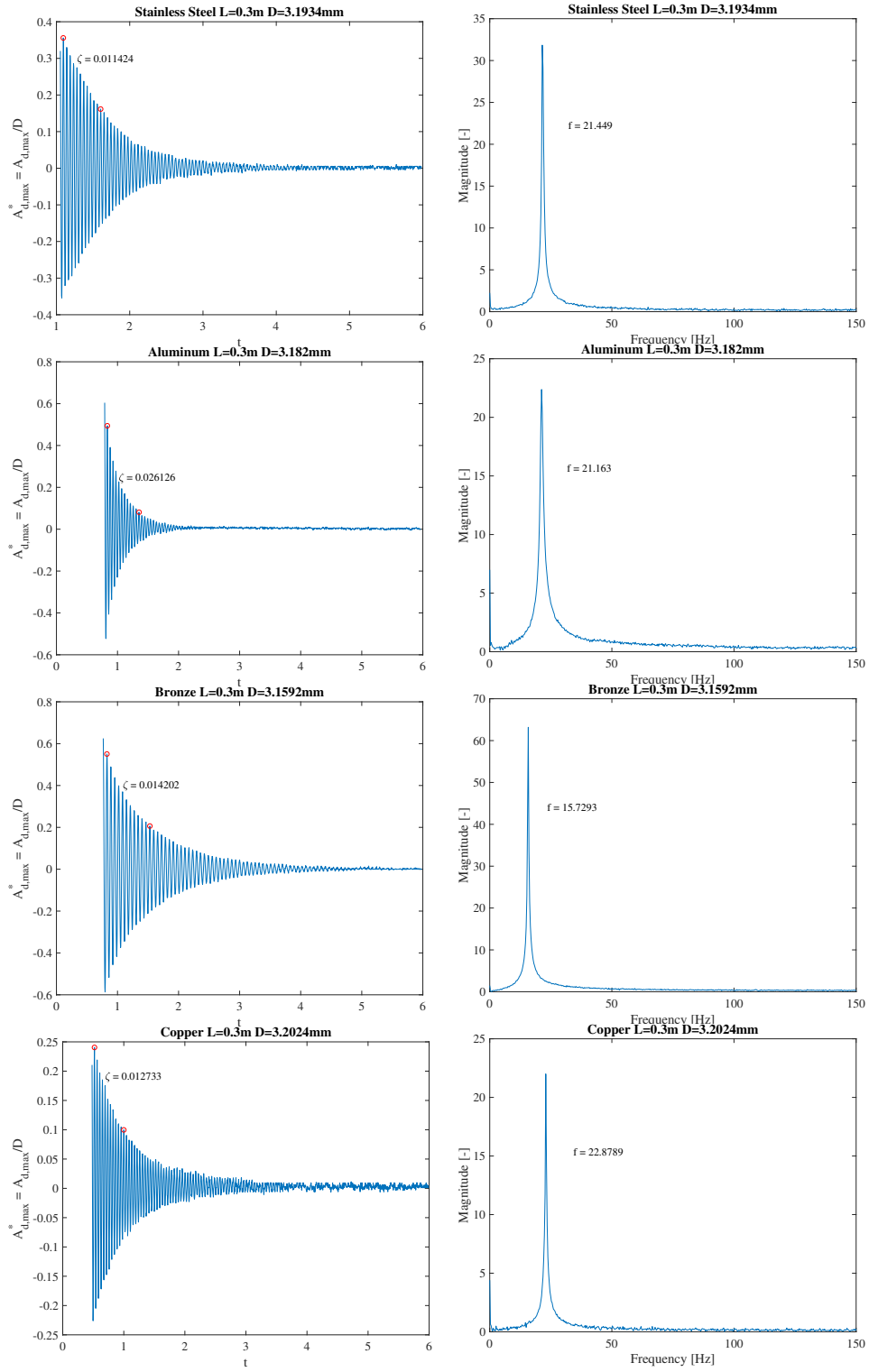

Path

Frequency

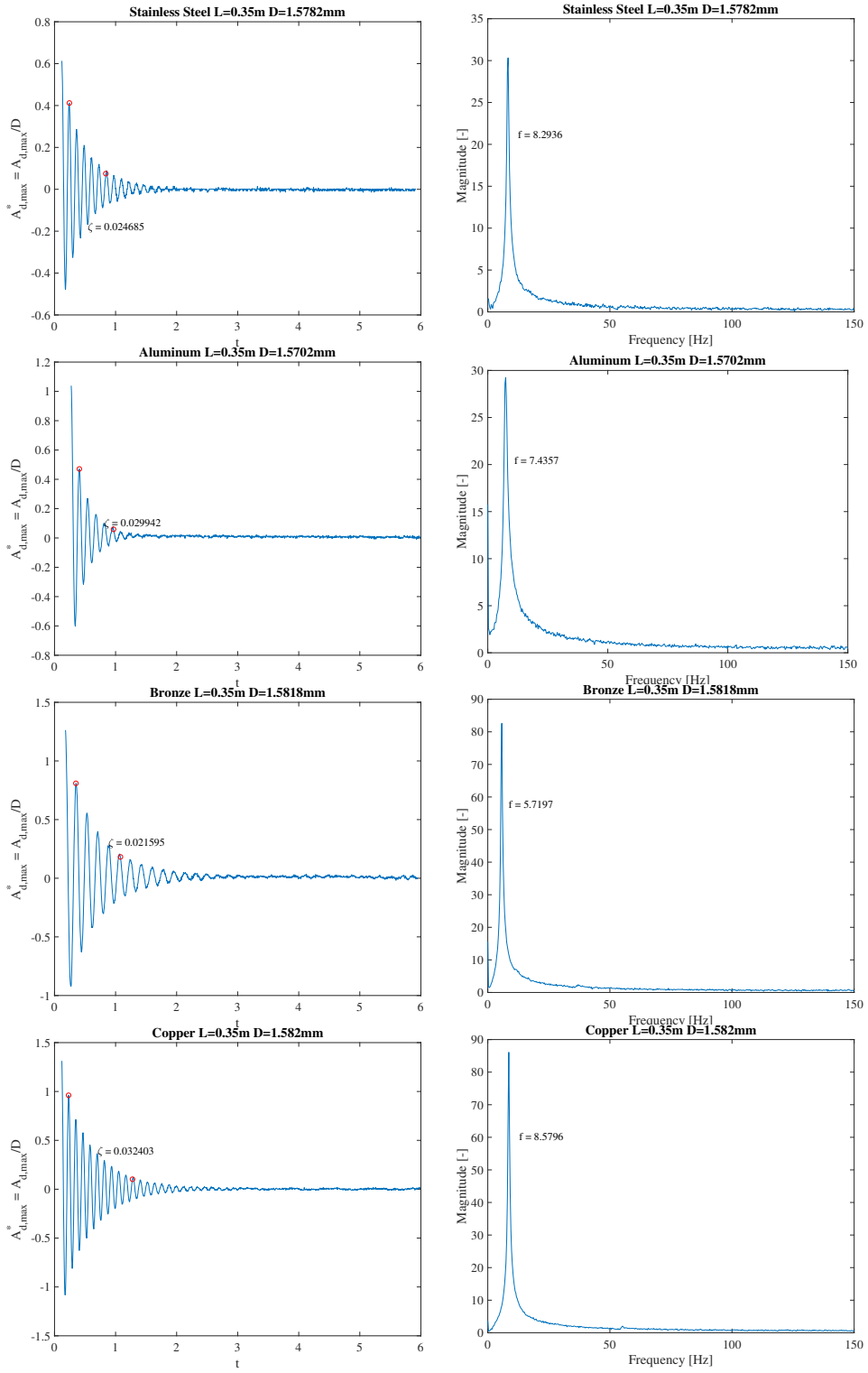

Path Frequency

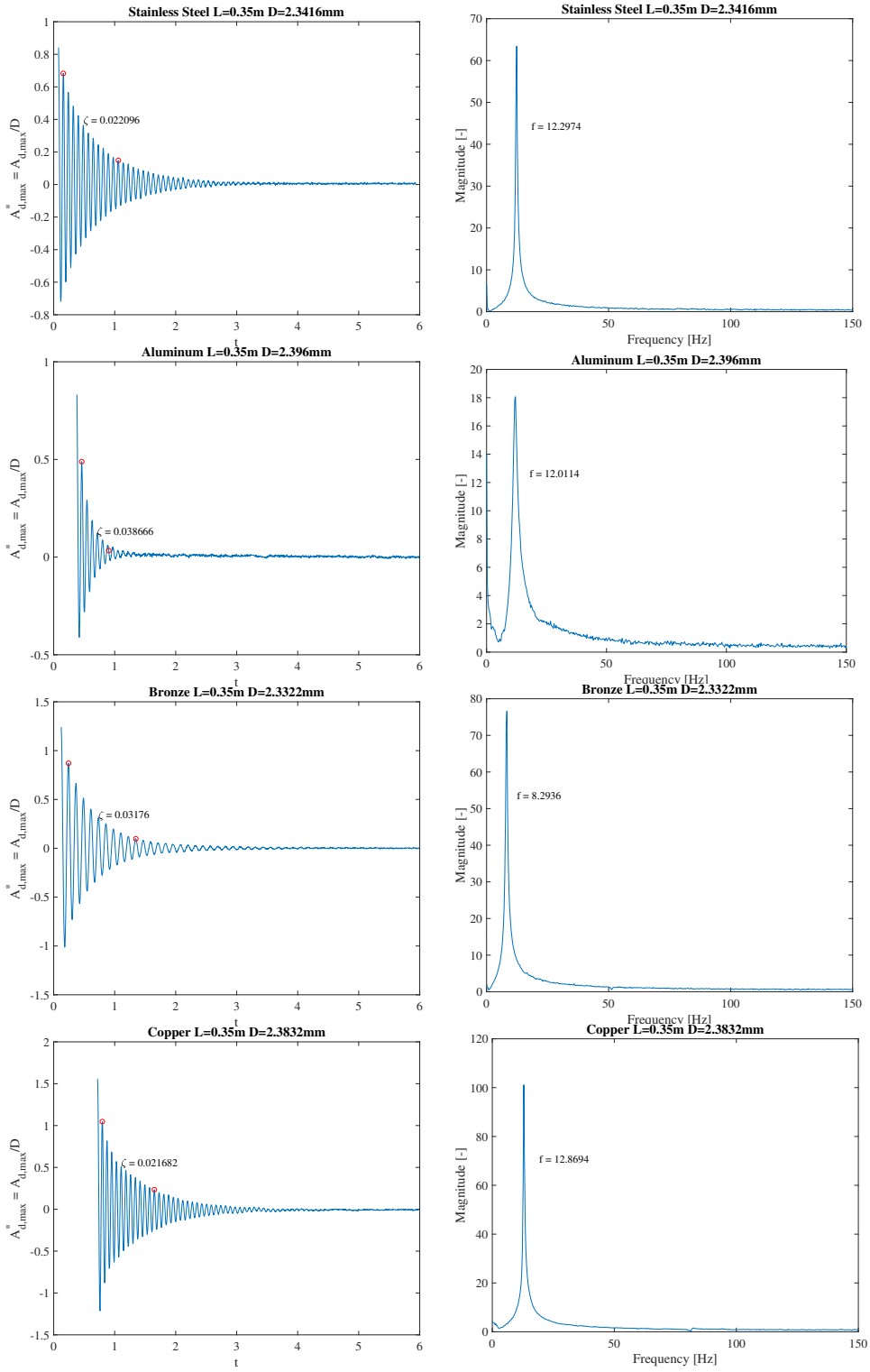

Path

Frequency

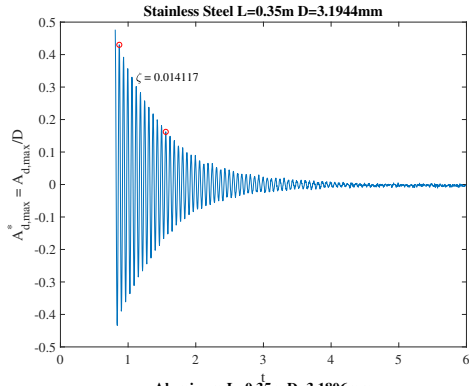

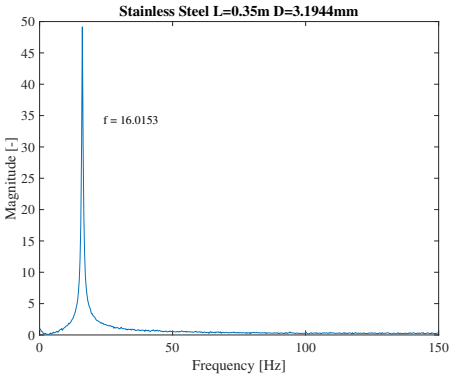

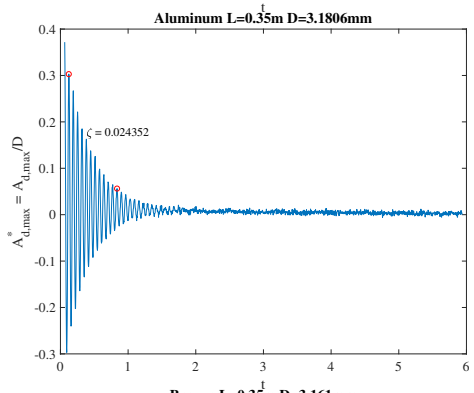

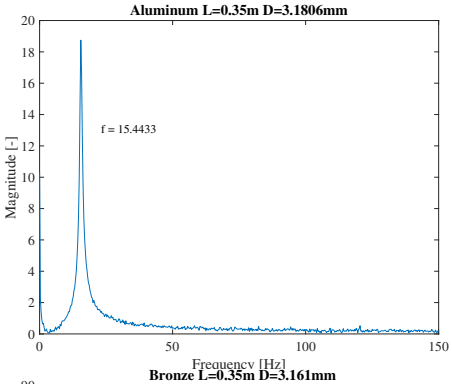

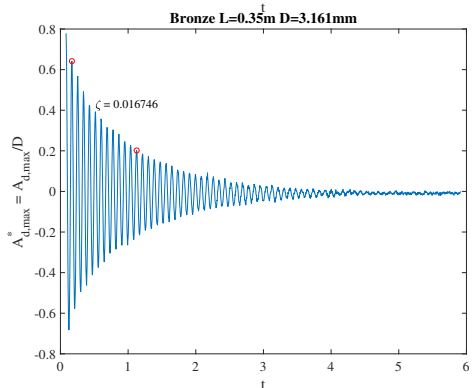

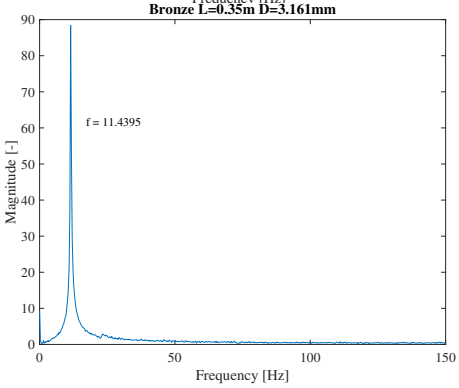

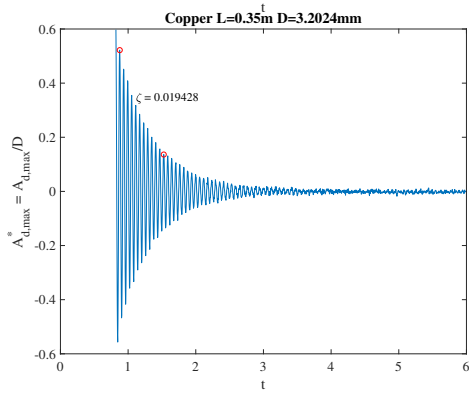

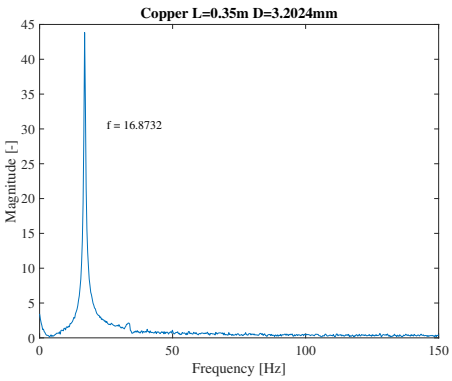

Path

Frequency

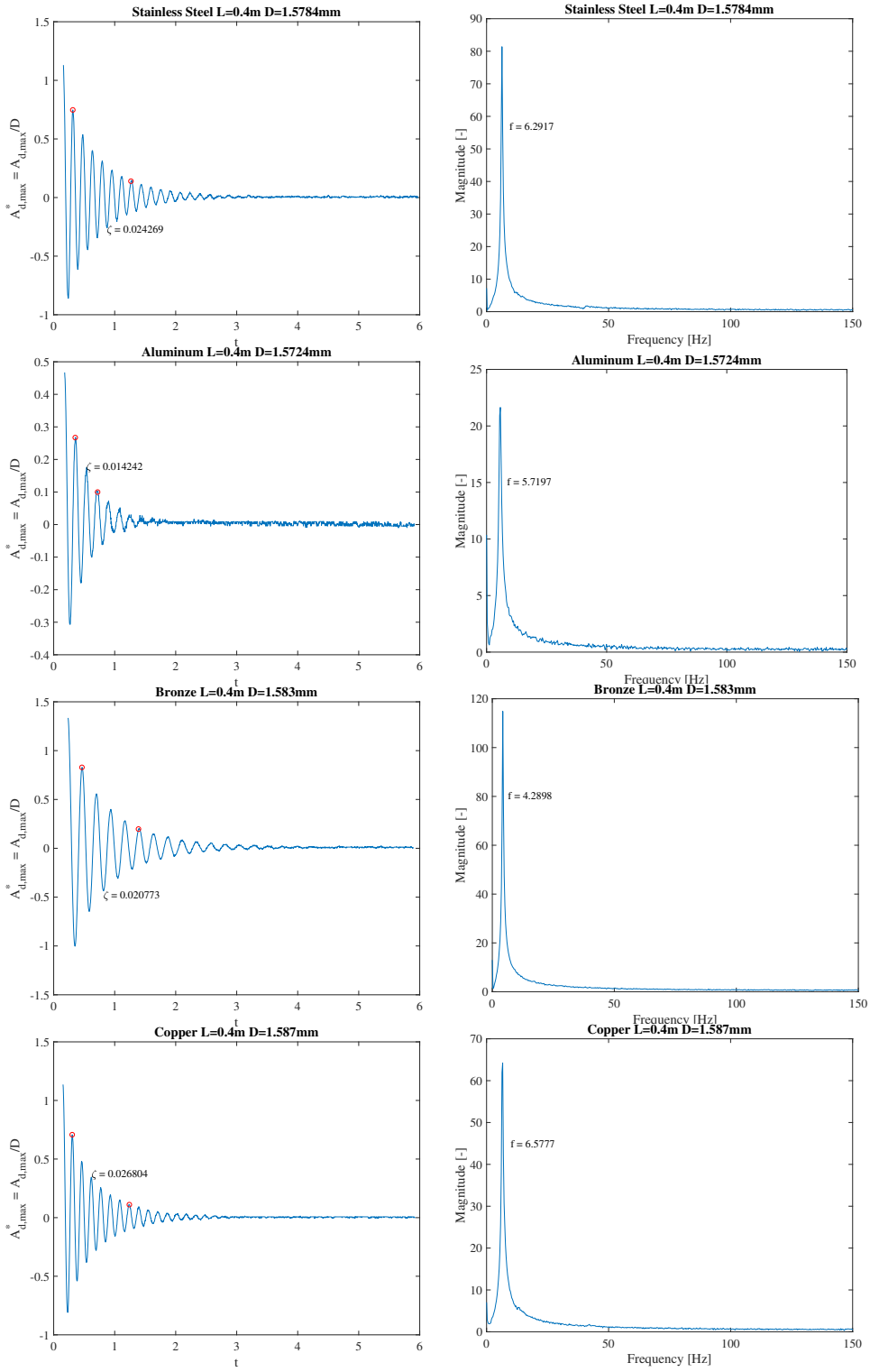

Path | Frequency

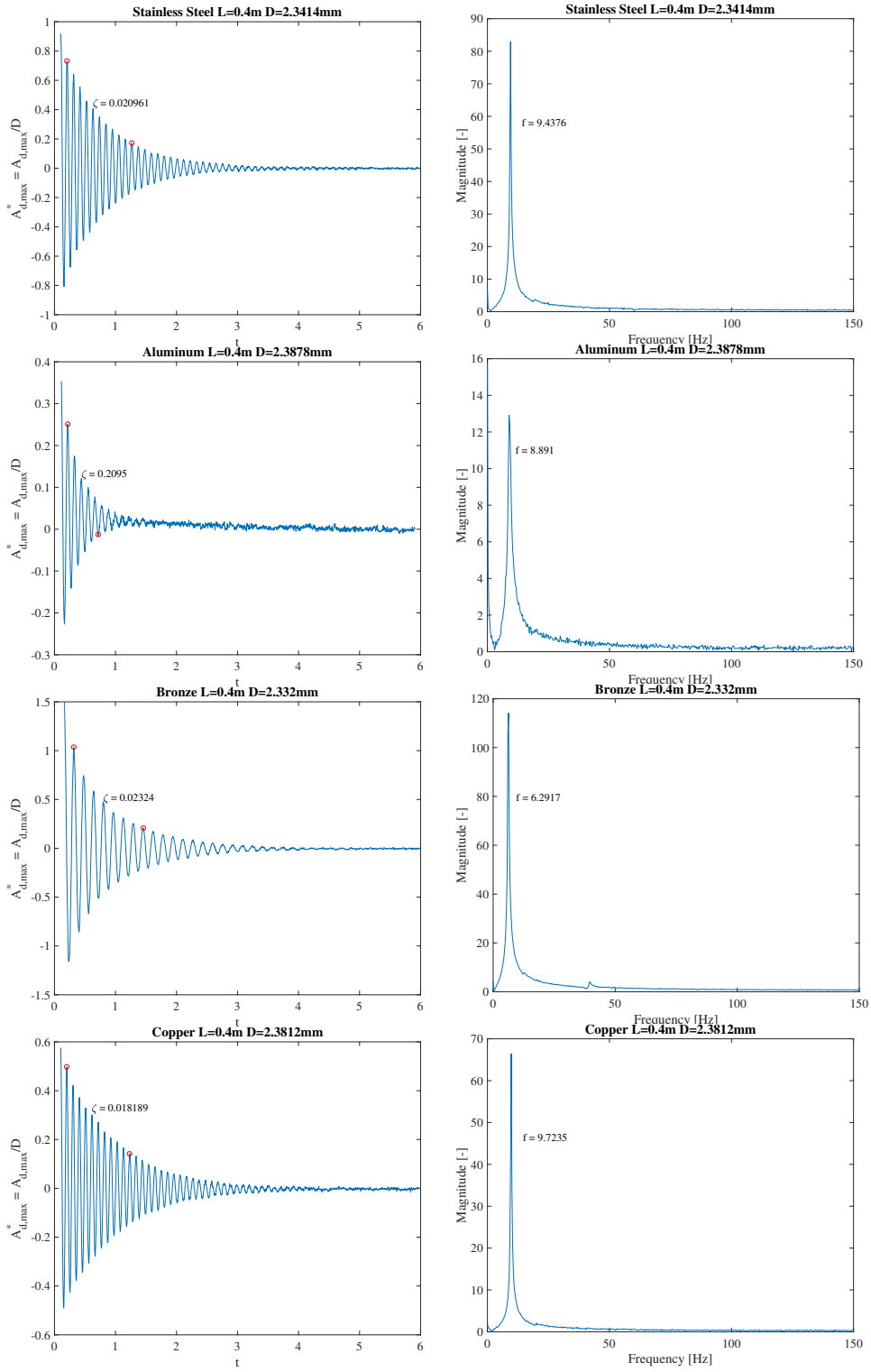

Path

Frequency